Implementing a Stochastic Soot Model in a 3D Domain

By

Tyler Strickland

A dissertation submitted in partial fulfillment of
the requirements for the degree of

Doctor of Philosophy

(Mechanical Engineering)

at the

UNIVERSITY OF WISCONSIN–MADISON

2021

Date of final oral examination: 1/15/2021

The dissertation is approved by the following members of the Final Oral Committee:
Sage Kokjohn, Associate Professor, Mechanical Engineering
David Rothamer, Associate Professor, Mechanical Engineering
Mark Anderson, Assistant Professor, Mechanical Engineering
Qin Li, Associate Professor, Mathematics
Jaal Ghandhi, John Bollinger Chair of Mechanical Engineering and Grainger Professor of Sustainable Energy, Mechanical Engineering

To my dad, my grandpa, and Davey

It's only a test

— Jeff

CONTENTS

LIST OF TABLES

LIST OF FIGURES

NOMENCLATURE

Acronyms

ABF Appel, Bochorn, Frencklach [3]

ARS Aromatic Site soot model

BCCA ballistic cluster-cluster aggregation

CFD Computational Fluid Dynamics

CFD Computational fluid dynamics

CPC Condensation Particle Counter

DNS Direct Numerical Simulation

DNS Direct numerical simulation

DSM Discrete Sectional Model

ELPI Electrical Low-Pressure Impactor

ERC Engine Research Center

FSN Filter Smoke Number

GCI Gasoline Compression Ignition

GPU Graphical Processing Unit

HACA Hydrogen abstraction C_2H_2 addition

HPC High Performance Computing

KH Kelvin-Helmholtz

LDEF Lagrangian Droplet-Eulerian Fluid

LE Lagrangian-Eulerian

LNS Eulerian-Lagrangian Numerical Simulation

LPDA Linear Process Deferment Algorithm

LPEF Lagrangian parcel - Eulerian fluid

LST Lagrangian Soot Tracking

MoM Method of Moments

MPI Message Passing Interface

MPM Multiple particle method

MSP Multistep Phenomenological

OpenMP Open Multi-Processing

PAH Polycyclic Aromatic Hydrocarbon

PAH Polycyclic aromatic hydrocarbon

PDF Probability/Particle Distribution Function

PSD Particle Size Distribution

PSI-CELL Particle-Source-In Cell

RDF Rate Distribution Function

RT Rayleigh-Taylor

SGS Sub-grid Scale

SMPS Scanning Mobility Particle Sizer

SPM Single Particle Method

TDC Top Dead Center

TEM Transmission Electron Microscopy

Greek Symbols

α_{sa} scattering to absorption ratio

α_{surf} ABF active surface fraction term [3]

η efficiency

κ conductivity

λ mean free path

λ wavelength

μ viscosity

ν kinematic viscosity

Ω nice volume

ρ mass density

σ attenuation radius

τ characteristic time / time constant

Non-dimensional parameters

Kn Knudsen Number

St Stokes Number

Operators

[ ] concentration

$\Im(\ )$ imaginary part

$\mathcal{O}(\ )$ order

∇ differential

Ex( ) expectation

$'$ corrected

Pr( ) probability

Roman Symbols

n normal vector

v velocity

Ea activation energy

Eo optical property

Fo optical property

NA Avagadro's number

A Arrhenius preexponential

a Particle radius

C emperical constant

C_A fuzzy particle structure prefactor

D diffusion coefficient

D_f fractal dimension

dV differential volume

F force

f_v soot volume fraction

K kernel

k_b Boltzmann constant

K_e extinction coefficient

L optical path length

l length

m mass

$M0$ soot particle concentration

m_o complex index of refraction

MW Molecular weight

n_p number of primary particles in a soot aggregate

P pressure

Q optical efficiency

R gas constant

R_g radius of gyration

s surface area

T temperature

t time

u speed

x_p dimensionless particle size

Y_a scattering correction coefficient

Sub-/Superscripts

0 initial

a absorption

b boundary

e extinction

fmr free molecular regime

g gas

p particle

s total scattering

ABSTRACT

In this document a highly detailed stochastic soot model limited to 0D simulations is coupled to 3D domains through the use of a Lagrangian parcel-Eulerian fluid method. Although both the stochastic soot model used and the Lagrangian parcel-Eulerian fluid method have long histories of development, their use, as described in this document, is novel and useful. Previous works significant to the model's development include documents from both the stochastic and simpler soot model genre and the fuel, aerosol, and other particle tracking and Lagrangian parcel-Eulerian fluid genres. Developing the theory behind the model is crucial to its implementation because of the unconventional Lagrangian parcel-Eulerian fluid representation. In fact, the Lagrangian parcel-Eulerian fluid coupling is only a means of simplifying the much more difficult theoretical model. Despite the accompanying assumptions, the complete model is validated from the bottom up and then again in a holistic fashion with promising results. Then the model is used in multiple case studies, showcasing capabilities not had by other models. The optical properties of soot generated in a Spray A simulation are calculated to find measured results are likely overpredicting the mass of soot along the central axis via KL extinction measurements. A thermophoresis submodel that calculates force based on the soot particles' shape is installed to find it has a high influence on the path of the heaviest soot particles. Investigations into the HACA mechanism for soot growth and the effect of syngas on soot in 3D domains are performed with much more detail than has been available before.

1 LITERATURE REVIEW

Soot morphology continues to gain attention as size and shape dependent relations are discovered. These include adverse respiratory health effects [56] and links to fuel properties [73].

Meanwhile, experimental soot measurements for such information prove to be limited, difficult, and usually include substantial uncertainty. The most common soot measurement techniques with some morphological data are scanning mobility particle sizer (SMPS) or electrical low-pressure impactor (ELPI) measurements. One challenge with these techniques is that they only provide an equivalent diameter that must be interpreted to determine either soot mass or soot particle shape. Gulijk et al. [49] found that interpretations of these results depended on the fractal degree of the soot being measured. More morphological information is obtained using transmission electron microscopy (TEM) but sample collection and preparation becomes a major concern due to the typical staging process required. Typical TEM measurement like that used in the work of [80] et al. measuring exhaust soot particles use samples collected on TEM grids that have been exposed to pre-measurement evolution while traveling down the measurement passage and are subject to nonuniform particle collection based on morphology. Kook et al. [73] and Kondo et al. [71] avoided soot evolution during sample transit while collecting fractal dimension data in mixing controlled combustion in a constant volume chamber by putting the TEM grid directly in the sampling location [71]. This method still has uncertain measurement bias for certain particles sticking to the TEM grid. It is also not easily adapted to an engine case. Fierz et al. [34] applied an electrostatic charge to ultra-fine aerosol particles before flowing them past the oppositely charged TEM grid to get a standardized sticking behavior that can provide morphology-based concentrations. Using this method on soot would expose the sample to premeasurement evolution during charging.

These measurement difficulties and inefficiencies make accurate soot simulation extremely lucrative. Unfortunately, soot production pathways, that may have many stages, based on

sensitive polycyclic aromatic hydrocarbon (PAH) species, flame structure, and mixture dependent behavior cause easily flawed or incomplete simulations [10, 64].

There are many distinct modeling methods that have been developed and continue to be used and modified. The unifying link between all phenomenological soot models is their attempt to describe a system with a difficult number of constituents by using average values. This problem extends beyond soot into problems of dust [90], rain and snow [66], galaxy collisions [72], and antigen and antibody interaction [86]. To model these problems directly would mean considering each particle, or instance, individually. For typical engine conditions, not only is running a unique calculation for the sheer number of soot particles prohibitive in a computational cost sense. Tracking every particle would push Eulerian characteristic cell sizes into nanoscales and memory requirements to the order of 10 Gb per cm^3 to store only the locations of every particle. The absolute inability of conventional computers to handle such a case can obfuscate the problem to the point of neglecting soot particles' particle nature. Several direct numerical simulations (DNS), identified by resolution for all flow features on continuum length scales, still use an average representations of soot [78, 108], even when many soot particles are larger than small flow scales.

The mathematical statement used to precisely move from considering every individual particle to averages of particles is given by the Smoluchowski equation [112]:

$$\frac{\partial n(x,t)}{\partial t} = \frac{1}{2}\int_0^x K(x-y,y)n(x-y,t)n(y,t)dy - \int_0^\infty K(x,y)n(x,t)n(y,t)dy \qquad (1.1)$$

for $x > 0$ and $t > 0$ where x is the particle size. For particles with multiple characteristics, x can be vectorized and the equation can be brought into multiple dimensions. In essence, the equation is a ledger of particles. The left hand side of this equation, $\frac{\partial n(x,t)}{\partial t}$, is the time derivative of the number of particles of size x at time t. The first term on the right hand side represents a source of particles of size x, while the second term on the right hand side represents a sink of particles of size x. In the source term, particles of size x are produced by

two smaller particles that add up to x, call them $x-y$ and y, coagulating. In the source term, particles of size x are removed by any other particle coagulating with x and increasing its size. The rate at which $x-y$ and y coagulate is concentration dependent, hence the n terms. K is the coagulation kernel, where $K(x,y)$ gives the expected rate that a particle of x and y size will coagulate. The coagulation kernels are the transition terms that give statistical answers to a discrete phenomenon. That is, based on only particle types, y and $x-y$, and not the individual circumstances of particles of that type, the expected coagulation rate is determined.

For soot, coagulation is typically thought of in chemical kinetics terms where kernels are based on collision theory [123] or transition state theory [75]. If the coagulation type is more ballistic in nature, collision theory provides the coagulation kernel. In collision theory molecules must collide with enough energy to overcome the activation energy to "stick" and form the product. If the coagulation type is more molecular structure based, transition state theory provides the coagulation kernel. In transition state theory reactant molecules exist on potential energy surfaces that have stable troughs separated by higher energy peaks. Practically, the reactants must form a transition state molecule that is usually at a higher energy level than the initial and final state. Note that despite the two different motives, transition state and collision theory provide very similar kernels. Because of the chemical basis of these submodels, progress in their formulation follows the progress of larger detailed chemical mechanisms. Appel et al. [3] formulated the widely used hydrogen abstraction C_2H_2 addition (HACA) pathway to grow soot based on a collection of many other previous PAH mechanisms. This gave kernels for soot surface reactions. Patterson et al. [95] validated the combination of the free molecular and continuum soot coagulation kernels via the harmonic mean, §A.1, to be accurate at all combustion pertinent scales.

The differences between soot models are, in essence, differences in simplifications made to Equation 1.1 and the solution method to the equation that results. This means that the

coagulation kernel submodels are often shared between models.

At the most basic and simplified end of the soot model spectrum, there are the widely used multistep phenomenological (MSP) models described by Fusco et al. [42]. In this type of model, all soot is treated equally, and a general soot amount is the only calculated parameter. Variations like the acetylene inception, 9-step model of Liu et al. [79] differ in the modeled phenomenon that effect the balance, such as O_2 and OH oxidation submodels.

Increasing in complexity, models maintain the phenomenological steps of inception, coagulation, and surface reactions but use a more complicated representation of the soot population. The widely used variations of the method of moments, originally developed by Frenklach [36], can be found in Converge, Fluent, Chemkin [27, 35, 103]. This method describes the soot population using moments (section A.11). Although it is a topic of interest in the theoretical math sector, a unique size distribution cannot generally be reconstituted from an incomplete set of moments requiring further empirical assumptions for a particle size distribution [4, 57, 106]. Again, variations on this method are typically just differences in the phenomenon considered, such as that of Kazakov et al. [62] who used different collision kernels based on whether the soot was in transition or continuum regimes of soot concentration.

Even more complex with a more complete soot description is the discrete sectional model (DSM) created by Gelbard [43]. This model manages discrete sections that each represent particles of a certain size, providing a dynamic discrete size distribution. Its various modifications can be found throughout literature and implementations are found in commercial software such as Converge and Chemkin [27, 103]. Like previously discussed models, variations are usually differences in the steps. For instance, the work of Veshkini et al. [124] that proposed a surface reactivity function to improve the models handling of particle aging.

Finally, the highly detailed Monte-Carlo stochastic model was first implemented for soot by Balthasar et al. [5]. Goodson et al. [45] modified the Monte-Carlo method by replacing

the coagulation kernel with a majorant kernel that reduced the numerical expense by an order of magnitude. Patterson et al. [94] further modified the Monte-Carlo method by implementing linear process deferment algorithm (LPDA), which delayed other events until coagulation events were resolved for quicker simulations. The Monte-Carlo method is intrinsically different than the previous models in that it does not solve the population balance in a deterministic way, with a numerical solution, but in a probabilistic way.

This change has many consequences. Other deterministic methods' computational expense scale approximately exponentially with the description of the particles but the stochastic method is minimally affected [15]. So, simplifications made to the population balance can be drastically reduced by describing each particle with multiple variables, effectively making the size of the set of particles, *i.e.* N in the Smoluchowski equation, massive. Morgan et al. [87] tracked positions and radii of all primary particles in a particle giving them space-filling representations of particles. Better particle description allows better submodels such as the aromatic site soot model (ARS) developed by Celnik et al. [15], which improves on the well-established ABF (Appel, Bochorn, Frencklach [3]) model by tracking the surface functional sites (armchair,etc.) of the particles.

The cost of enhanced particle descriptions is 3D implementation difficulties. With only a few soot descriptors (x_i), convection-diffusion equations can easily be added to model equations and solved numerically in a 3D domain with Eulerian methods, but the massive number of particle types of the stochastic model would require an equal number of transport equations which would be absolutely prohibitive for any current computer. Most efforts to use a stochastic model in a 3D domain are all efforts to discretize a 3D domain into pseudo-0D domains and then use the stochastic model conventionally. Mosbach et al. [88] simulated the soot of homogeneous charge compression ignition (HCCI) cases with 3D effects such as mixing with a Stochastic Reactor Model. Wang et al. [128] did the same thing for a gasoline compression ignition (GCI) case with special attention to the wall film soot formation

due to exceptional environments created by fuel droplet wall impingement and subsequent evaporation and mixing.

An alternative method to an Eulerian numerical scheme of the soot transport equations is to model soot particles in Lagrangian parcels of the Eulerian-Lagrangian numerical simulation (LNS) scheme used earlier by Crowe et al. [23] in the particle-source-in cell (PSI-CELL) method identified by Patankar et al. [93]. This method has a long history in aerosols, including modeling fuel droplets in sprays in the Lagrangian droplet-Eulerian fluid (LDEF) variations used by KIVAv3 and Converge [2,103]. LNS has been adapted for Lagrangian soot particles to create Lagrangian soot tracking (LST) used by [59] and others. In these works, soot particles were initialized through simple means, along an isotherm for instance, and then tracked for spatial insight with no expectations of general soot information. Wan et al. [126] and Zuber et al. [140] used LST for direct-injection diesel cases where each particle represented a fixed number of like particles modified by surface growth, determined by a modified Hiroyasu model, and oxidation processes, determined by Nagel-Strickland Constable soot oxidation expressions. The primary purpose of these models is tracking particle motion and not particle growth, but they were capable of producing soot particle size distributions despite their questionable validity.

One of the many difficulties with a comprehensive LST model is how to represent $\mathcal{O}(10^{17})$ particles, each of which is interacting with the surrounding gas on a volumetric basis. Recently Ong et al. [91] advanced the LST soot model concept, basing it on a semi-empirical formulation and confronting model-based inception. Coagulation was ignored because the model was intended to only simulate primary particle size. Lagrangian soot particle inception was initiated by a minimum cell incipient species density threshold. Like the earlier works of Wan and Zuber, each particle represented a group of like particles. Unlike those works, the number represented was based on a submodel. Two methods to represent many particles were proposed and studied. The first, single particle method (SPM), calculated the

number of soot particles that needed to be represented based on the incipient soot mass in the Lagrangian particles original cell. The second, multiple particle method (MPM), initializes a fixed number of Lagrangian particles at each timestep, with a density throughout the domain that is described by $\rho_{\text{particles}} = \frac{m_{\text{incipient},i}}{\sum m_{\text{incipient},i}}$. No error analysis was performed on the methods, but simulation results between the two methods were compared.

Additional literature review, more specific to certain applications of the new soot model, is included as an introduction to those sections.

2 MODEL

The literature review section cited many works of stochastic soot models and Lagrangian parcel - Eulerian fluid (LPEF) models; however, to the author's knowledge, the implementation of a fully coupled stochastic soot model via LPEF has not been explored. The following is a description of such a soot model, including parts that have already been discussed in other works to provide context, albeit much abbreviated.

Purpose

Combustion is simulated using computational fluid dynamics (CFD), which is essentially a numerical algorithm so solve the discretized conservation equations (mass, momentum, energy), §A.5. Combustion complicates the problem by being multiphase, multicomponent within each phase, and adding many source terms that may be volumetric and over many scales. Soot is one of those complications. Soot is produced and consumed during combustion, sinking or sourcing mass and having momentum, and energy and is in the solid phase. Submodels define these source and sink terms within the confines of the conservation equations. The accuracy of the soot submodel may be crucial to the combustion simulation in general, but it is certainly important in determining soot values. The purpose of this work is to produce a soot model that describes soot in more detail than conventional soot models at a reasonable computational cost.

SWEEP

SWEEP is a software package aimed at solving for the evolution of highly detailed soot population information given the soot's environmental condition through time. SWEEP is a phenomenological soot simulation program. It solves the population balance problem (equation 1.1) using stochastic Monte Carlo based methods. The Monte Carlo method is an algorithm used to solve difficult systems that can be represented statistically. Repeated

random sampling to converge to the expected result underpins the method. Convergence to the expected value is guaranteed based on the law of large numbers:

$$\overline{X}_n \rightarrow \mu \qquad \text{for} \qquad n \rightarrow \infty \tag{2.1}$$

where $\overline{X}_n = \frac{1}{n}(X_1 + \cdots + X_n)$ is the sample average and μ is the actual expected value. The law of large numbers states that the average of a set of independent and random values will approach the expected value in the limit of the size of the set [5,32]. This is an intuitive law but an important one too because it ensures that repeated sampling of the same set should converge to an average value and not trend or oscillate, like a broken experiment may.

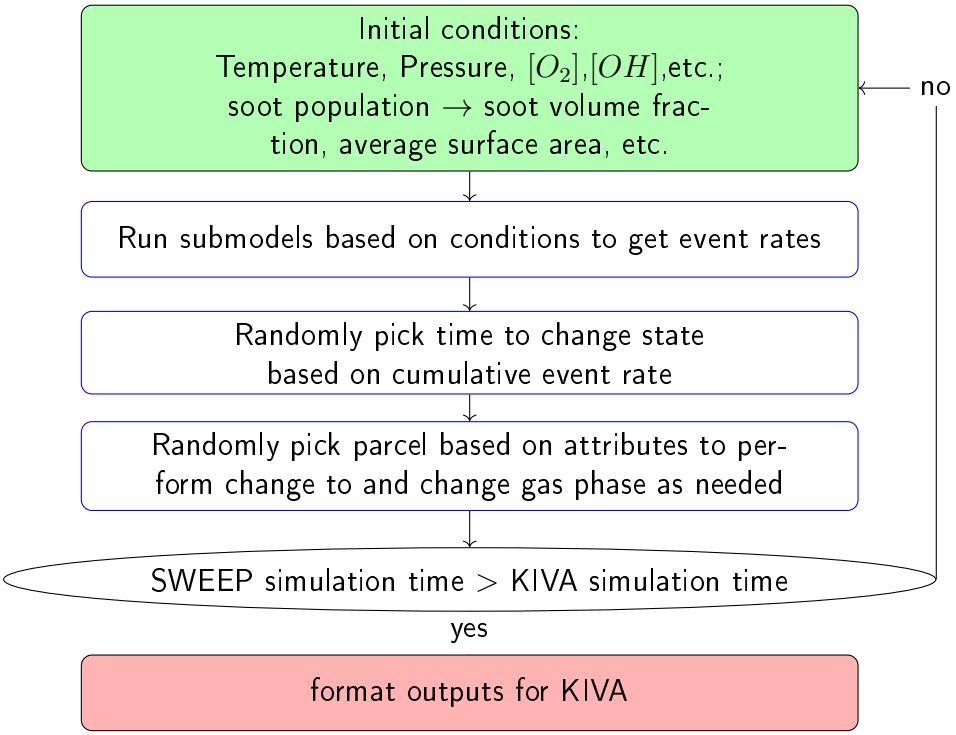

Figure 2.1: Simplified flow chart of the SWEEP simulation algorithm as it is used in the current model

Figure 2.1 shows a flowchart of SWEEP's simulation algorithm as it is formatted for use in KIVA. Like all submodels, simulation begins with the initial conditions. Like many soot models, the gas phase temperature, pressure, and pertinent species concentrations are

initial conditions. Unlike most soot models, the initial soot information is stored in discrete particles. SWEEP tracks a random set of virtual soot particles. The virtual particles are described by a set of variables, i.e. virtual properties. The set includes constitutive number of carbon and hydrogen atoms, surface area, active surface site fraction (using the ABF model), and a history of age, number of condensations, surface reactions, and coagulation. Functions of these, such as volume, mass, and collision diameter, are calculated.

In the next step in the flowchart, submodels are calculated based on initial conditions. Like all phenomenological models, the initial conditions are used in submodels for different phenomenon to find rates of change in the soot population and in the gas phase. The phenomenon considered in this model are:

- inception - two body pyrene collisions

$$\text{rate}_{\text{inception}} = \frac{1}{2} k_{\text{tr}} [\text{PAH}]^2 \tag{2.2}$$

  where [PAH] is the concentration of PAH, and k_{tr} is a transition kernel made from the harmonic mean (A.1) of the free molecular regime and slip flow regime kernel.

  Inception results in the creation of a new incipient soot particle. Two gas phase molecules collide to form what is recognized by the model as a soot particle. In the implementation of the soot model for the work of this document, this occurs when two pyrene molecules are consumed to create a soot particle with 32 carbon atoms and 20 hydrogen atoms. Pyrene is used as an inception species because it is hypothesized that pyrene is a representative polycyclic hydrocarbon that undergoes few form altering gas phase reactions that are not also on the pathway to larger soot pathway molecules. i.e., it is sufficiently far along the soot production path to avoid molecular reformatting. Other species have been proposed as inception species including smaller, acetylene, and larger, benzopyrene, particles, because the cost of a larger mechanism

must be weighed with accuracy. Studies from Zhang et al. [134] have investigated different inception species and found pyrene acceptable. The inception event is modeled using collision theory (equation 2.2).

- condensation - free-molecular collision between gas and soot

$$\text{rate}_{\text{cond}} = \eta 2.2[\text{PAH}]\sqrt{\frac{\pi k_b T}{2m_{PAH}}}(d_{PAH}^2 + 2d_{PAH}a_P + a_P^2) \tag{2.3}$$

η is the collision efficiency, k_b is the Boltzmann constant, a_p is the soot particle collision diameter, d is the gas phase collision diameter, and m is the mass.

Condensation is closely related to inception, with one of the inception species molecules replaced by an already formed soot molecule. Condensation for every particle is modeled by the free molecular collision rate (equation 2.3). Condensation is not commonly considered a major factor and does not often become a major factor in simulations. High condensation rates require low concentrations of pyrene relative to soot particles.

- surface reactions

Surface reactions are conceptualized as chemical reactions rather than the more ballistic interpretations of the other soot coagulation processes [37].

$$\text{rate}_{\text{surface}} = AT^n \exp\left(-\frac{Ea}{RT}\right)\prod_{j=1}^{J}\psi_j^{p_j}\prod_{i=1}^{I}C_i^{v_i} \tag{2.4}$$

ψ_j is a characteristic of the particle pertinent to the particular reaction. Equation 2.4 is the Arrhenius rate equation but with an optional term, ψ_j, that replaces the collision diameter.

  - addition - acetylene soot collision

    Addition is modeled using equation 2.4 with an active surface area coefficient (equation 8.1) and radical site coefficient determined by the HACA model. With

the terms populated, equation 2.4 becomes

$$\text{rate}_{\text{add}} = A\alpha_{surf}[C_2H_2][s_{\text{soot}}]T^n e^{-\frac{Ea}{RT}}, \tag{2.5}$$

where A is the Arrhenius preexponential, $[C_2H_2]$ is the acetylene concentration, s_{soot} is the soot surface area, n is the temperature exponent, Ea is the activation energy, R is the gas constant, T is the temperature, and α_{surf} is ratio of radicalized active sites to soot surface area [3]. More details are in section 5.

– oxidation - OH and O_2 with soot collisions

Oxidation is modeled using equation 2.4 with an active surface area coefficient (equation 8.1) and radical site coefficient determined by the HACA model. More details are in section 5.

- coagulation - Smoluchowski coagulation equation, equation 1.1

Coagulation between two already formed soot particles is modeled using the Smoluchowski coagulation equation. The coagulation kernels within the Smoluchowski equation are based on collision theory so the calculated frontal collision diameter of the particles are used.

Moving on to the random jump node of the flowchart, a random time is selected based on the submodel rates. Because the soot information is stored in discrete particles and not a continuous concentration value, rates from the phenomenon submodels cannot be directly transferred to the soot population. Instead, probability theory is used to move between the continuous space of the submodels and the discrete space of the particles. Precisely, the virtual soot particles are the subjects of Markovian processes (Appendix A.2), modified by random events occurring according to the Poisson distribution (Appendix A.3). This means

once the cumulative event rate is found based on the submodels, a random time is picked based on that rate for a discrete change to occur to a particle.

Once the time is picked, the next node of the flowchart is reached. Here the event type and the particle to which the event occurred is selected randomly and based on probability. The probability of the event enacted is based on its rate relative to the other events and the particle to which it happens is based on the particles' pertinent characteristics. The particle undergoes a change that is representative of the event occurring. For instance, the state of a particle after a virtual oxidation event with OH will have one less carbon atom. At this point, the conditions are now different than the initial conditions and the simulation has moved forward.

The next step in the flow chart is a check to see whether the SWEEP simulation time has surpassed the KIVA simulation time. If it hasn't, the process is repeated. If it has, the simulation is complete and the changes are formatted to be read by the parent simulation.

2.1 Partitioning a 3D domain

It is worth noting, despite mentions of LPEF throughout this document, the generalization of the model discussed herein is more accurately described as a sectional model in which the sections are highly dynamic. Only through assumptions made during implementation (section 2.1) does the model earn its LPEF coupling description.

SWEEP is a stochastic model that assumes all elements (i.e. X_i in equation 2.1) are indistinguishable beyond their multi-variable representation. So, a particle's location in an inhomogeneous domain would break the model. In essence, SWEEP is a 0D model. Unfortunately, interesting cases occur over inhomogeneous domains. The following is a method to use many 0D simulations to solve an inhomogeneous problem.

Small regions can be assumed homogeneous. In a continuous domain, for any variable, for any ϵ, you can pick a subdomain small enough such that the variation in that variable

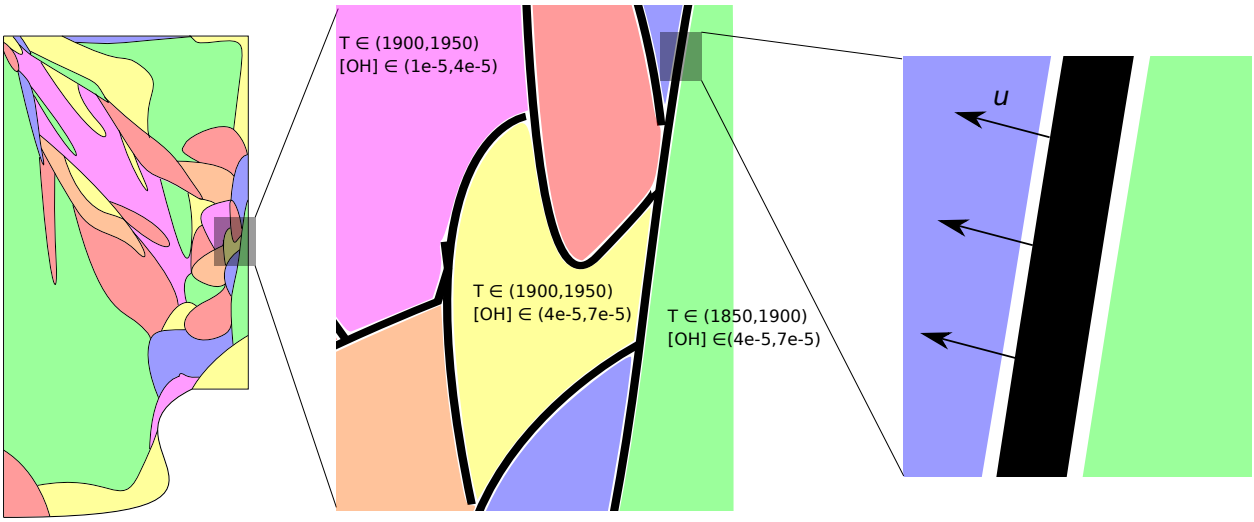

Figure 2.2: Cartoon of domain partitioning. Different colors represent different subdomains.

over the subdomain is less than ϵ. So a partition can cover the entire inhomogeneous domain with pseudo-homogeneous subdomains. Figure 2.2 shows a cartoon of a 2D cylinder domain covered by a partition. Note that the subdomains have temperatures and species concentrations that vary by less than ϵ. Because of the homogeneity, each subdomain can support its own independent SWEEP-like simulation. Subdomains are a moving reference frame for the soot within. Soot motion and subdomain evolution is described by Reynold's transport theorem

$$\frac{d}{dt}\int_{\Omega(t)} \mathbf{f}\, dV = \int_{\Omega(t)} \frac{\partial \mathbf{f}}{\partial t}\, dV + \int_{\partial\Omega(t)} (\mathbf{v}_b \cdot \mathbf{n})\, \mathbf{f}\, dA \tag{2.6}$$

where Ω is the bounded volume, $\mathbf{n}$ is the outward unit normal vector, $\mathbf{v}_b$ is the velocity of the boundary relative to the velocity of the bounded fluid, and $\mathbf{f}$ is a function (soot concentration, for instance). Subdomain boundaries are moved at the gas phase velocity by setting $\mathbf{v}_b = 0$. If $\mathbf{v}_b \neq 0$ then the flux of soot through the boundary must be handled. This must be done stochastically. Random virtual particles must be traded from the domain losing volume to the domain gaining volume in a quantity proportional to the flux.

In reflection, fundamental assumptions made in the general model:

- ϵ_i is a sufficiently small deviation to consider homogeneous.

- Subdomain movement (macroscopic acceleration) is unimportant to soot.
- Soot has no volume.

Eulerian fluid - Lagrangian parcel coupling

Models, such as the G-equation combustion model [77], have difficulty tracking a single boundary in the Eulerian field. To avoid tracking boundaries over multiple cells, set ϵ such that the subdomain spans only a single cell. All boundaries will be defined on sub-grid scale (SGS).

Every subdomain will have a central point. This point will be represented by a Lagrangian parcel. The parcels' motion through cells represents the resolved motion of the subdomain boundaries.

Subdomains will be initialized (a Lagrangian soot parcel will be added) in vacant cells (cells without a Lagrangian soot parcel) when a threshold inception species is exceeded. Lagrangian parcels are created as a function of the represented volume partition and local parcel divergence (i.e.,$\nabla \cdot \rho_{\text{parcel}}$).

The assumptions and simplifications required for this variation on the model are:

- Subdomains divide the volume of their parent cell up equally.
- Regions without soot or soot inception species of a certain threshold are unimportant.

2.2 Installation

The soot model is coupled to the combustion simulation via source and sink terms in the species (Appendix A.5) and mass (Appendix A.5) and momentum (Appendix A.5) conservation equations. The species and mass equation source/sink term resolves molecules leaving or entering the gas phase as a result of reactions with soot. The momentum source/sink term comes from the body force needed to accelerate soot particles in a changing flow field.

The transfer of momentum from the gas phase to soot is modeled using the coefficient of drag based on the electrodynamic diameter of the soot particles. Currently soot is assumed massless, so this term is 0 but it does exist.

These terms are produced in SWEEP based simulations, run in an additional step of the combustion simulation's operator splitting scheme.

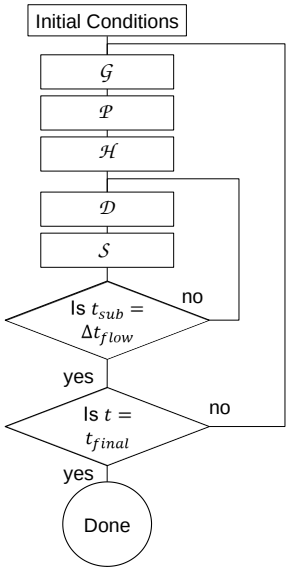

Figure 2.3: Simplified flow chart of the combustion simulation time step splitting algorithm

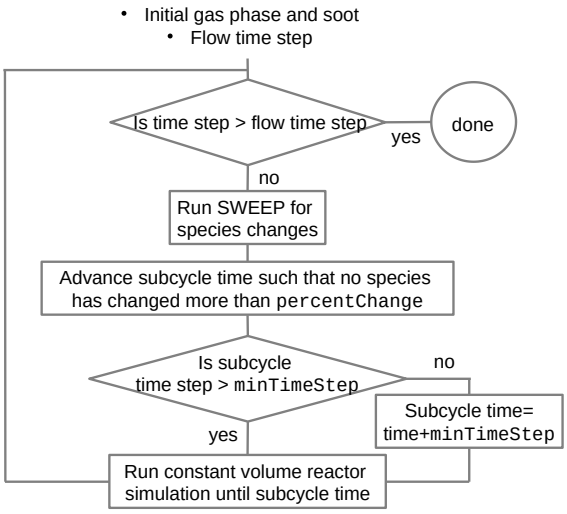

Figure 2.4: Simplified flow chart of chemistry/soot time step splitting algorithm

Figure 2.3 shows the operator splitting flowchart for KIVA with the soot model implemented. In KIVA, the largest (flow) timestep is split between gas phase advection and diffusion (G), parcel motion (P), heat transfer (H), detailed chemistry (D), and soot evolution (S). So, any variable x must be solved for using the approximation

$$\frac{dx}{dt} \approx G(x^g) + P(x^p) + H(x^h) + D(x^d) + S(x^s) \tag{2.7}$$

where $x^p(t_{\text{initial}}) = x^g(t_{\text{final}})$, assume $G(x^m) = 0$ for $m \neq g$. Within equation 2.7 detailed chemistry and soot are stiff.

Gas phase species important to soot production are often scarce. Pyrene, or other large

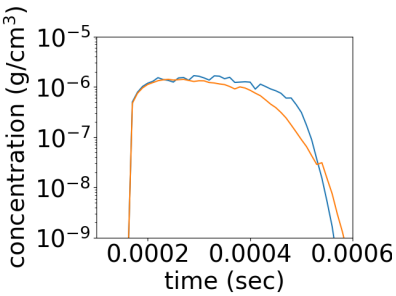

Figure 2.5: Pyrene concentration over time as simulated by SWEEP with the indicated time step. blue line: subcycle time step of 1e-7 sec. orange line: subcycle time step of 1e-10 sec

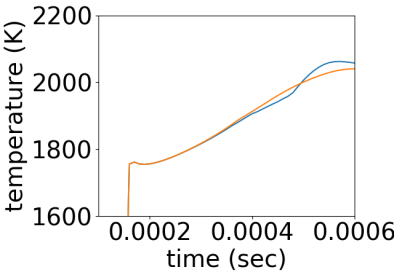

Figure 2.6: Temperature over time as simulated by SWEEP with the indicated time step. blue line: subcycle time step of 1e-7 sec. orange line: subcycle time step of 1e-10 sec

soot precursory PAHs, monatomic hydrogen, and hydroxide are prime examples. Soot processes can be severely limited by these species' concentrations. The numerical realization of this is species concentration covering orders of magnitude by the chemistry and soot solvers. In other words, the species concentration problem is much stiffer than the fluid flow that controls the time step. An important assumption of the operator splitting method is that the variables being solved for are relatively constant over a time step, i.e. in pseudo steady state. To restore the pseudo steady state assumption, the chemistry and soot steps are subcycled within a flow time step. This is outlined in the flow chart of Figure 2.4. The soot model advances the simulation time until a species concentration is varied up to a threshold amount, at which point control is given to the chemistry solver. The chemistry solver matches the soot models simulated time, and then control is passed back to SWEEP. This loop continues until the flow time step is reached. In this way, species concentration is never allowed to vary by more than the specified amount.

Figure 2.5 shows the domain averaged pyrene concentration of a diffusion flame simulation over time using a subcycle time step of 1e-7 and 1e-10 seconds. A subcycle time step of 1e-7 corresponds to roughly the flow time step and causes the species concentration thrashing previously discussed. A subcycle time step of 1e-10 is small enough to create pseudo steady state conditions over sweep and chemistry solution steps. Figure 2.6 shows the domain av-

eraged temperature for the same simulations. It is obvious that there is a C^1 discontinuity in the solution at approximately 0.5ms. Differences between the concentrations and related values indicates the operator splitting pseudo steady state assumption is not valid for flow time steps and confirms the importance of subcycling.

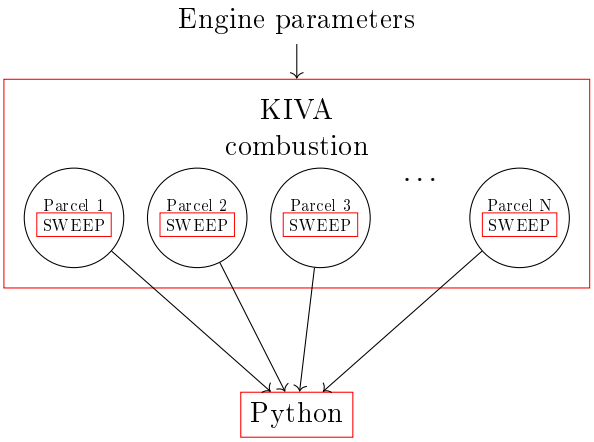

Figure 2.7: Simplified flow chart of simulation process for the direct model

Figure 2.7 shows the compute flowchart for a simulation. A single combustion simulation spawns many soot parcels during runtime. Each parcel has its own OD modified SWEEP simulation that has been described earlier. All of these subsimulations are completely coupled to the parent combustion simulation. In postprocessing, all the parcel data that has been logged can be viewed individually or the results can be mapped onto the domain for a volumetric interpretation.

As mentioned in the literature review (section 1), fuel spray models use LPEF-based models extensively. This includes its use in KIVA. Comparing the two expedites soot parcel model development and helps implement the data structures for new Lagrangian parcels. Fuel droplets and soot particles share, source / sink terms in momentum and species equations, domain boundaries, and descriptions ($\vec{x}, \vec{u}$, mass, temperature, shape). They do not share coefficient of drag submodel, parcel genesis and destruction modes, viscous effects, and surface models.

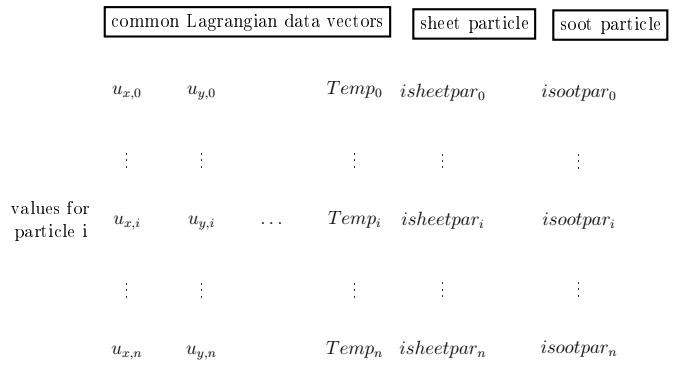

Figure 2.8: Extended vector topography for Lagrangian parcels

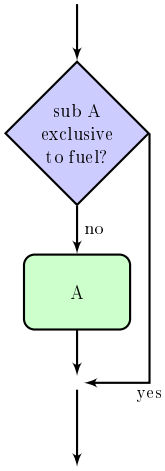

Figure 2.9: Flowchart for subroutine execution using the extended vector set

Based on the soot and fuel parcel similarities, KIVA's parcel data structures and transport subroutines can be shared. KIVA keeps track of parcel properties using vectors with the index corresponding to the parcel identity. To implement soot parcels, the current set of Lagrangian data vectors was extended to include a soot flag. Figure 2.8 shows the vector array. Values not needed by a parcel, such as the sheet parcel flag, were ignored. The soot flag was used in subroutine conditionals to avoid fuel or soot parcel specific routines depending on the parcel type (Figure 2.9). It also controlled which parcels were associated with an additional set of SWEEP simulation data structures. This was functionally important because the memory requirements of the soot model are quite high.

2.3 Rank responsibility

Section 2.5 introduced the extended hybrid model to deal with coupling and memory problems, however, if the surrogate soot model does not recreate the source and sink terms in the conservation equations A.6, then the extended hybrid model is flawed and the direct model is required. Accordingly, the direct model is still worth improving.

In the direct model, computational cost memory-wise is substantial and dependent on

the mesh size. A single parcel may reasonably have 2^{15} (32,768) particles, each described by 8 floating point numbers 64 bits long, costing more than a Mb. Many meshes have far more than 1,000,000 cells. If 1:10 cells produces non-negligible soot and each parcel requires a Mb of memory, the soot simulation will require more than 100 Gb of memory.

Currently, KIVA uses a master rank to distribute and collect all parcels. This scheme requires a single processor to have enough memory to house every parcel. For loads like the one described above, depending on the system architecture, this may be slow or impossible. Other programs such as OpenFOAM [48] and Converge [103] use a distributed scheme where the domain is distributed amongst the ranks. This allows much larger meshes and it can also allow many more parcels. KIVA's solvers are not designed for such a distributed scheme and converting it would be a major undertaking. Fortunately, the engine simulations currently considered are sectors, relatively coarse, and do not require a lot of memory without the soot model. A distributed scheme for just the parcels would reduce a lot of the memory cost. Since parcels are already passed between rank 0 and the slave ranks, most of the infrastructure to implement such a scheme already exists. The additional components needed include a directory of where parcels are logged and a layer for slave ranks to pass to other slave ranks.

2.4 High performance computing

The previously described soot model is substantially faster than DNS, however, it would be dishonest to call it a light or cheap model. Evidence of its expense can be found in its requirement of, a detailed gas phase chemistry model. (The G-equation combustion model is certainly cheaper.) KIVA utilizes multicore processing in solving chemistry to alleviate some of this expense. Multicore processing is added to the soot model with the same intent.

MPI was chosen over GPUs, OpenMP, or vectorization because of the significantly independent character of the stochastic models along divisions of time steps and parcels. Additionally, MPI is used to distribute the chemistry solver and the coupling of chemistry and

soot benefits from similar handling.

Depending on the soot parcel parameters, the runtime of the soot simulation can vary by orders of magnitude. Accordingly, dynamic load balancing of the ranks (MPI processing units) is crucial for performance. For each timestep, parcels are distributed by rank 0 to slave ranks in small subsets in a round-robin fashion to avoid one rank getting an especially troublesome section of the domain. The ranks solve the soot simulation for each parcel according to the flowchart of Figure 2.4. When the rank has completed the soot simulation for all of its parcels, the results are returned to rank 0. If there are more unassigned parcels, the process repeats.

Program profiling has been used to confirm that message passing (a major downside of MPI) is not the bottleneck of the program. Even so, to minimize the message passing time, parcel data structures have been vectorized for more efficient communication via `MPI_Gather`, `MPI_Send`, and `MPI_Recv`.

Simulations are always a compromise between speed and accuracy. So that the cost of decisions made in the validation stage are understood, memory and time cost profiling is done for different model aspects.

Table 2.1: Execution time and slowdown for SWEEP simulations of flame HWA1 with different ensemble sizes

ensemble size	time (sec)	time per element	slowdown (%)
128	0.088	6.88e-4	0
512	0.228	4.45e-4	-35.2
8192	6.18	7.54e-4	14.9
32768	24.56	7.50e-4	8.2

The slowdown for a SWEEP simulation with more virtual particles is documented in Table 2.1. Slowdown with the datum case using 126 particles is calculated using

$$\text{Slowdown} = \frac{\frac{t_{128}}{128} - \frac{t_n}{n}}{\frac{t_{128}}{128}} = 1 - \frac{t_n}{t_{128}}\frac{128}{n} \tag{2.8}$$

where t_n is the simulation runtime for n particles. Table 2.1 shows no evidence of anything

more than linear dependence on ensemble size despite the potential for exponential slowdown. This is possibly due to low rates of coagulation (the most expensive event).

Table 2.2: Performance data of the direct model in very sooty conditions. Note that the large case is running on univ and the small case is running on univ2 of the HPC cluster.

# ranks	simulated time (sec)	run time (sec)
40	2.437e-5	54676
192	2.435e-5	27534

Direct model simulation performance data is logged in Table 2.2. Applying speedup metrics

$$\text{Perfect speedup} = \frac{\text{N}_{many}}{\text{N}_{fewer}} \tag{2.9}$$

$$\text{Actual speedup} = \frac{1/t_{fewer}}{1/t_{many}} \tag{2.10}$$

where t_n is the runtime with n ranks.

$$\text{Disappointment ratio} = \frac{\text{Actual speedup}}{\text{perfect speedup}} = \frac{1.98}{4.8} = .414 \tag{2.11}$$

shows that the simulation does not achieve perfect speedup but does show significant improvement through adding more ranks. The disappointment ratio will be reduced as the time spent solving the advection-diffusion equations goes to 0 since that time does not utilize MPI.

2.5 Model hybridization

The stochastic model described in section 2.1 will be referred to as the direct model so that a variation on the model can be introduced. The preference towards the direct model in soot interested studies is obvious, however it's possible that without its full adoption by commercial simulation software, the model may experience limited use due to implementation difficulties. Most significantly, the direct model requires complete access to the source code to include changes to data structures and program flow. If optimization via MPI is included the changes become even more intrusive. Besides the source code changes, although the model is

Table 2.3: Comparison of the direct soot model to its alterations

	Gas phase species consumption and production	Stochastic soot simulation run during combustion simulation	Soot parcels generated and tracked by combustion simulation	Soot simulation surrogate models used
Direct	yes	yes	yes	no
One-way	no	no	yes	no
Extended Hybrid	yes	no	no	yes

usable on conventional computer systems, it's not necessarily cheap and the typical 12 hour turn around requirements for industrial use are often difficult to achieve.

The direct model is more expensive instruction-wise than industry standards in two ways. The standard coagulation kernel size grows by the number of stochastic particles squared [94]. That is, if one wants information for particles that only occur 1:10,000 of the time versus 1:1,000 of the time, as is the case for the PSD of Figure 3.19, then the number of calculations required will be $\mathcal{O}(100)$. Secondly, in the 3D solution method, every time step is dependent on / cannot progress without the slowest parcel. i.e. the model suffers from the "weakest link" problem.

Problems of source code requirements and cost are addressed by modifying the model while retaining the additional data provided via stochastic methods. Table 2.3 lists the alterations made to the fully coupled direct model. The first variation, the one-way model, is fundamentally different from the direct model by decoupling the SWEEP soot simulations from the combustion simulation. That is, the effects of soot on gas phase consumption or production, temperature, etc. are ignored. A result of the soot model decoupling is that the soot models can be run asynchronously to the combustion model.

The program flow chart of the one-way model is shown in Figure 2.10. When comparing the one-way model to the direct model, soot parcels are still generated and tracked by the combustion simulation but instead of the soot simulations being run in tandem with the combustion simulation, the parcel conditions are logged and passed to individual SWEEP

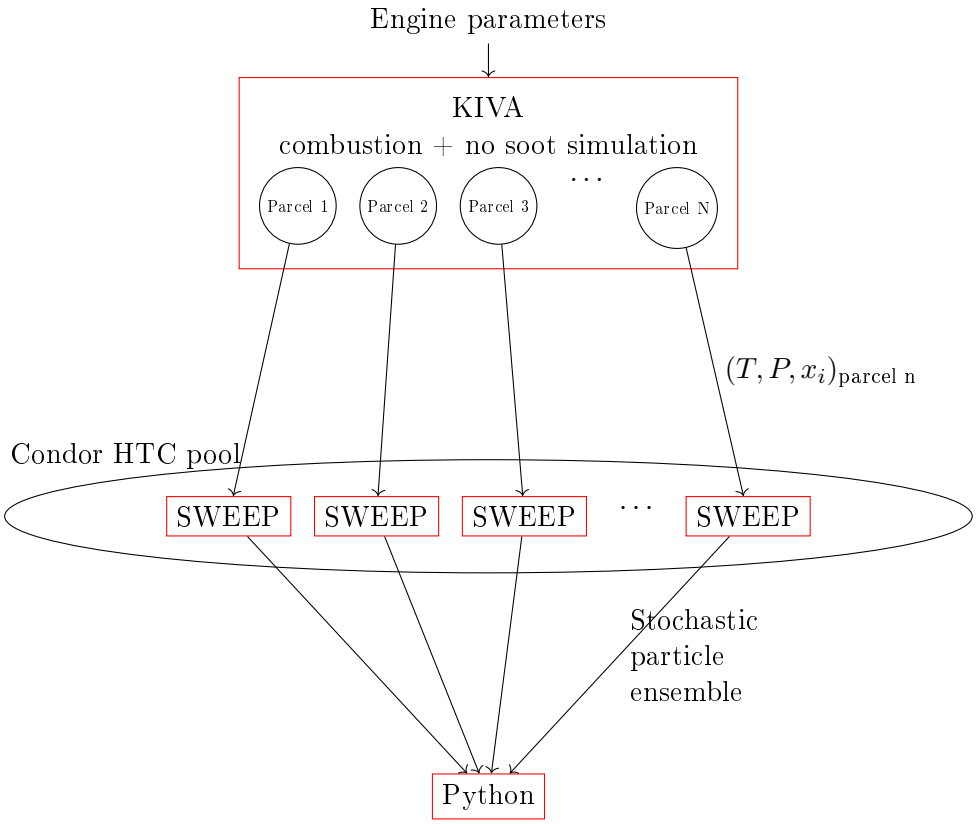

Figure 2.10: Simplified flow chart of simulation process for the one-way model

simulations in a postprocessing step. The individual SWEEP soot simulations are run using a completely different computational resource, namely the Condor High Throughput Computational pool [118]. The benefit of the one-way model is the reduced cost of the model by removing the weakest link problem. Additionally, the Condor HTC pool is a much cheaper and readily available resource than a high-performance computing cluster with fast interconnects.

The extended hybrid model is identical to the one-way model except it uses a secondary conventional soot model coupled to the combustion simulation and the Lagrangian soot parcels are generated in a postprocessing step. The program flow chart of the extended hybrid model is shown in Figure 2.11. The conventional model acts as a surrogate for the stochastic model that was moved into a postprocessing step. This creates a coupling between combustion and soot production that is missing in the one-way model. The best surrogate

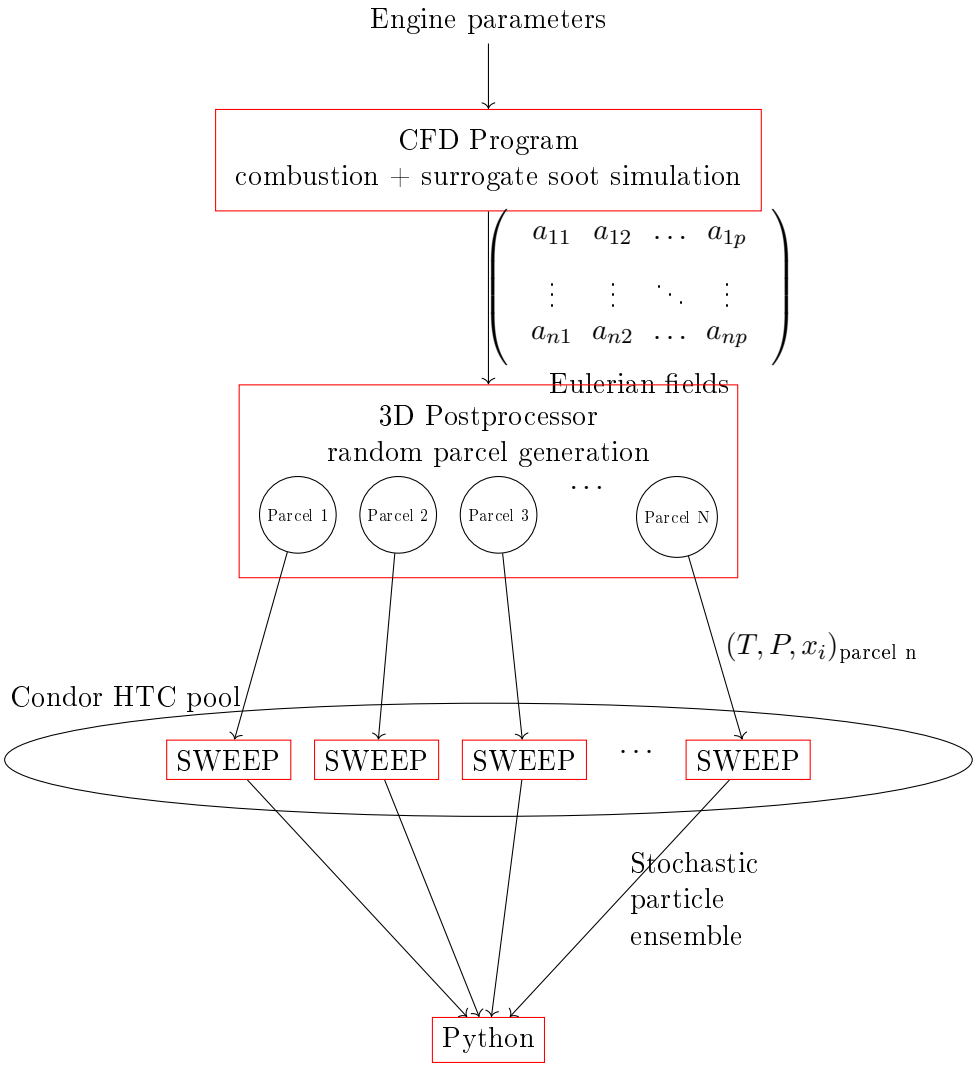

Figure 2.11: Simplified flow chart of simulation process for the extended hybrid model

model would predict the behavior of the stochastic model perfectly and the results from the direct model and extended hybrid model would be identical. Differences and simplifications in conventional soot models prohibit a perfect match; accordingly, the surrogate selection process is important.

Lagrangian parcels are initialized in post-processing at random locations in the same threshold inception species isovolume used in the direct model. They also follow path-lines governed by the same equations and gather the same species concentration data. Removing the stochastic soot simulations and Lagrangian parcels from the combustion simulation re-

moves the need for source code access; accordingly, the extended hybrid model can be used with any simulation software.

2.6 Extracting particle morphology

The soot model parameters are not necessarily the variables of interest for comparing to measured data or developing new models. For instance, the soot model keeps track of a particle's collision diameter, but measured results are based on electrostatic mobility diameter. Additional models are used in postprocessing to retrieve these additional variables from the soot simulation variables.

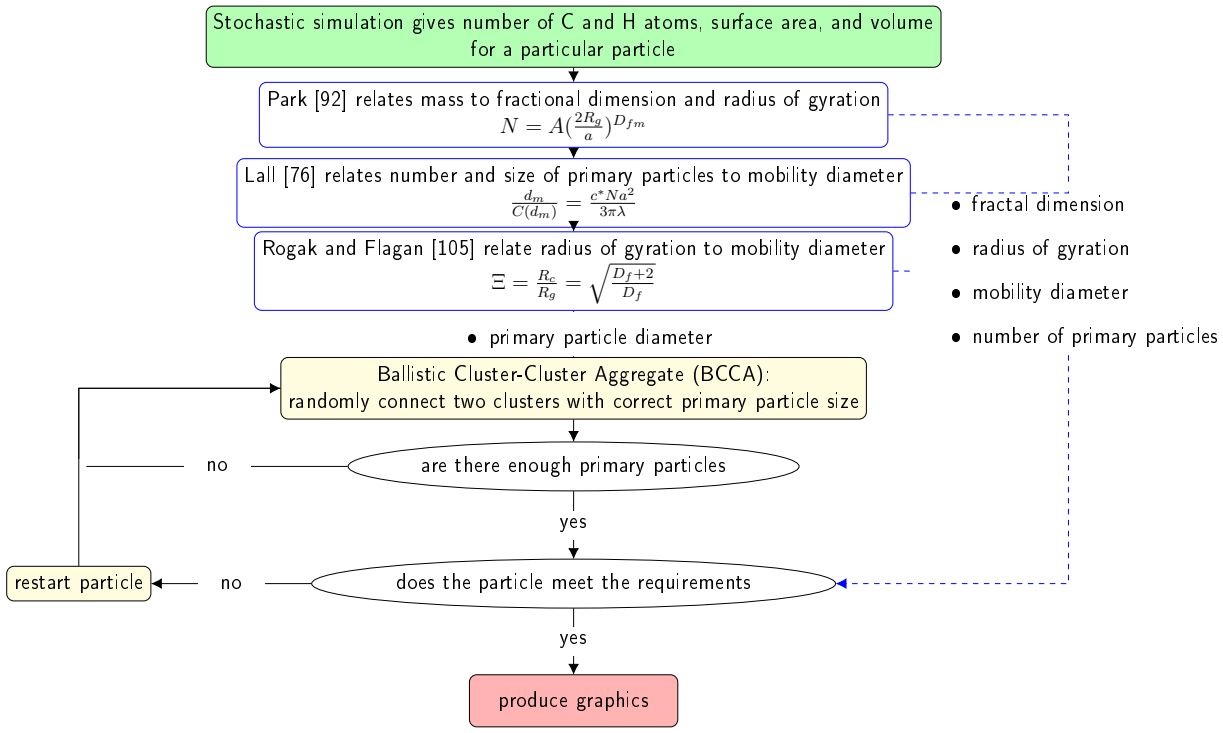

Figure 2.12: Flow chart of soot particle production algorithm

Figure 2.12 is a flowchart outlining the steps to produce a space-filling soot particle representation. Other interesting values, such as the electrodynamic mobility diameter, are calculated along the way.

Inferred morphology

The first step in extracting more particle information than the model provides is to make an assumption on the shape of the particle. For instance, to get a PSD, the method of moments soot model assumes an empirically observed PSD shape [36]. Fortunately, the stochastic model is much more detailed than the method of moments model and the assumption made is debatably intrinsic to the nature of soot.

Soot particles are often described using notions of fractals, meaning the particle's shape is roughly the same at any scale. Obviously and unlike conceptual fractals, there is a lower bound on the particle's fractal behavior. Less obviously, there may also be an upper bound caused by size dependent reshaping [109]. However, it is reasonable to assume the model predicted soot is within these bounds. Through fractal theory, the expression

$$N = C_g(R_g/a)^{D_f} \tag{2.12}$$

where N is the number of primary particles and is proportional to mass, C_A is the structure prefactor, R_g is the radius of gyration, a is the primary particle radius, and D_f is the mass fractal dimension (i.e., how 3 dimensional the fractal is)
relates the size to the number of primary particles or mass [12].

With this relation in place, an experimental value of the structure prefactor allows equation A.17 to be solved for the fractal dimension. The mass of the particle can be calculated from the number of carbon and hydrogen atoms. Subsequently, the mobility diameter can be calculated from equation A.14. and the radius of gyration from equation A.18 for particles in the Stokes regime.

Measured morphology comparison

SMPS measured electrostatic mobility diameter and simulated collision diameter may not be the most direct comparison. SMPS method determines diameter by comparing to a cali-

bration based on a perfectly spherical particle under influence of electrostatic and tangential acceleration forces. Collision diameter represents a perfectly spherical volume of influence in the collision rate term of event rate submodels (e.g., equation 2.2). Despite the electrostatic interpretation of the collision diameter, it is not obvious that these diameters should be one-to-one related. Using the algorithm described above, measured electrodynamic diameter is compared to simulated electrodynamic diameter in PSD plots.

Synthesized agglomerate space-filling representations

Ballistic cluster-cluster aggregation (BCCA) simulation software [8] mimics soot particle aggregation. The randomly produced particles can be characterized by Number of primary particles, primary particle size, fractal dimension, radius of gyration, and radius of gyration to collision radius ratio [74]. Particles from SWEEP simulations can be represented by randomly generated particles sharing similar characteristics. Figure 2.12 shows the algorithm to repeatedly produce random particles until a particle with the correct structure is produced.

Figure 2.13: Space-fill representation silhouette of a soot particle with 1024 primary particles, a primary particle diameter of 11 nm, a radius of gyration of 22.5nm, and a fractal dimension of 1.76

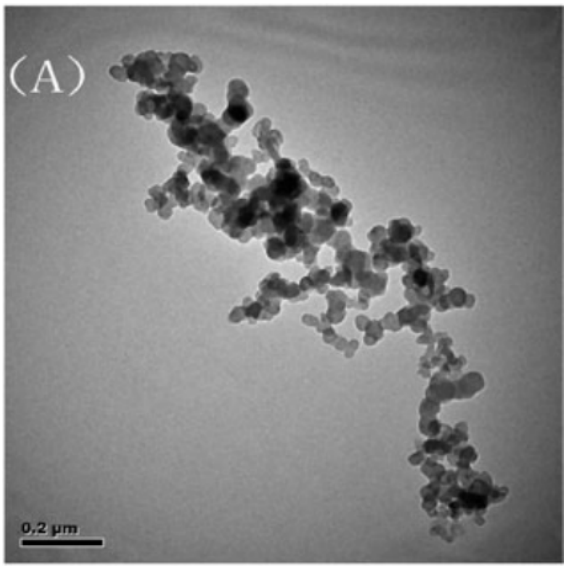

Figure 2.14: TEM image of a soot particle

Figure 2.13 is a soot particle generated using this technique and 2.14 is a TEM image of a soot particle from [80] with similar properties.

3 VALIDATION

Validation of the soot simulation follows a progression that is broken into multiple steps. Each step validates a layer that the remaining layers are built upon, such that the cumulative stack is valid. A valid stack ensures that the simulation will produce the correct soot results.

Figure 3.1 shows a pictorial representation of the validation stack. Soot is a product of incomplete combustion; accordingly, accurate soot predictions rely on the entire simulation scope including mixing, gas chemistry, and finally soot production [10]. As such, the combustion simulations need to be validated despite its indirect ties to soot. The SWEEP submodel that is the base of the soot model must also be validated in the same independent sense. SWEEP and the combustion simulation are coupled via the LPEF framework. In the previous section, §2, the actual LPEF framework was proven to be conceptually valid however, errors brought by the discreteness of the Eulerian mesh and other assumptions on the nature of soot parcels need to be considered. This happens in two stages. Firstly, convergence studies using different levels of discreteness show that the coupling works with

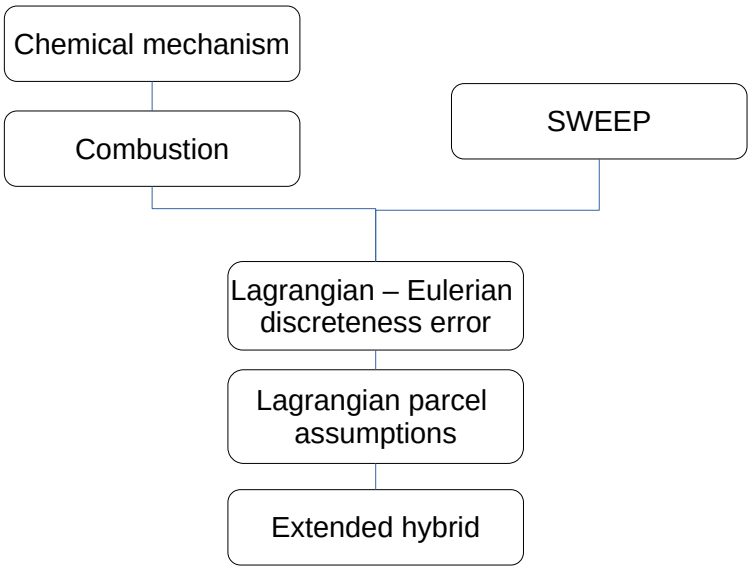

Figure 3.1: Validation stack for soot simulation via LPEF coupling. Note that the direct model is validated before the extended hybrid model.

sufficient mesh resolution. Secondly, numerical studies show that assumptions made on the nature of soot parcels are relatively accurate. At this stage, the direct model is validated. The extended hybrid model is validated by comparing results from a direct model to results from the extended hybrid model.

In this "bottom up" validation strategy, validation starts outside the scope of this report. Submodels, for instance, are not discussed here but in the cited parent documents. Chemical validation is one aspect that is not validated in this document but is mentioned due to its importance. Finally, the entire soot simulation stack is validated as a redundant sanity check.

3.1 Chemical mechanism validation

The Multicomponent wide distillate mechanism developed by Ren et al. [101] was the chosen chemical mechanism due to its reasonable size, age, and PAH pathway. The mechanism contains 178 species and 758 reactions, including a PAH pathway that extends to benzopyrene, the subsequent PAH after pyrene. This is useful in alleviating a false buildup of pyrene that would progress to larger PAHs. The correct concentration of pyrene is crucial to the SWEEP model as it uses pyrene as an inception species.

Substantial mechanism validation was conducted by Ren et al. [101]. This included comparisons to measured data for laminar flame speed, ignition delay, and species concentrations for species crucial to soot. Diesel fuel surrogate validation was also done for 0.1/0.9 molar fraction toluene/hexadecane, the surrogate used in diesel simulations of this document.

3.2 SWEEP validation

The relatively unconventional stochastic nature of the SWEEP program warrants a more detailed description of the validation. Firstly, the Monte Carlo methods are subject to large numerical errors if an insufficient number of samples are used. That is, an adequate cross section of the soot population is needed. Secondly, the typical physical approximation errors

must also be validated. According to the law of large numbers, the numerical error for a Monte Carlo type simulation goes to 0 as the number of particles goes to ∞. Simple convergence studies can be used to determine the practically necessary parameters to limit numerical error. Physical approximation errors are observed by comparing to measured data.

Table 3.1: Premixed burner stabilized laminar flame experimental conditions

handle	molar ratio				equivalence	pressure	inflow velocity	cite
	C2H4	O_2	N2	Ar	ratio	bar	cm/sec	
HWA1	0.242	0.379	0.000	0.379	1.92	1	7.0	[137]
JW1.69	0.127	0.183	0.690	0.000	2.07	1	5.9	[63]

Steady state burner stabilized laminar flame experiments were used because of their ability to be modeled in 0D, a requirement for stochastic soot models. Steady state burner stabilized laminar flames are modeled using CHEMKIN's purpose-built simulation. A description of the solver can be found in [27]. In short, measured centerline temperature profiles are used to close the energy equation in simulations. Results of the simulations are centerline profiles of species concentrations and axial velocity. The centerline distance of a control volume from the burner surface can be converted to time since leaving the surface via velocity. Then a moving reference frame matching the control volume can be modeled as a 0D with conditions changing in time. These 0D conditions can be given to SWEEP. The results of SWEEP can be compared to measured soot from the centerline.

The experimental data used are from two different ethylene flames described in Table 3.1. The HWA1 flame was collected by Zhao et al. [137] and JW1.69 was collected by Kazakov et al. [63]. Both are similar with an equivalence ratio of two, atmospheric pressure, and an inflow velocity of approximately $6.5 cm/sec$. The largest parameter difference is in their inert gas species. In terms of results, the soot volume fraction was captured for HWA1 while a normalized size distribution was captured for JW1.69.

Figure 3.2 shows PSDs at different heights simulated using different numbers of virtual particles. There is relatively quick convergence. Even for 128 elements, the shape of the PSD

(a) 0.5 cm

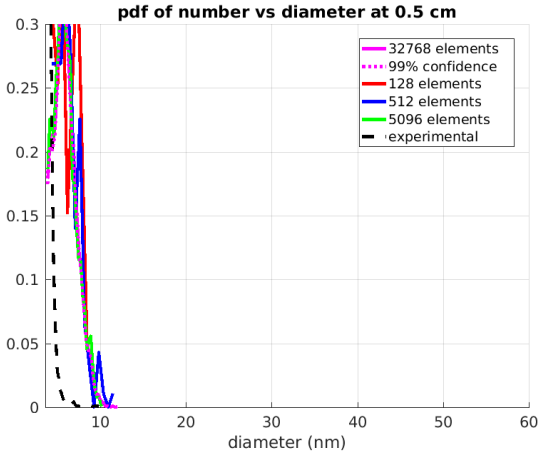

(b) 0.7 cm

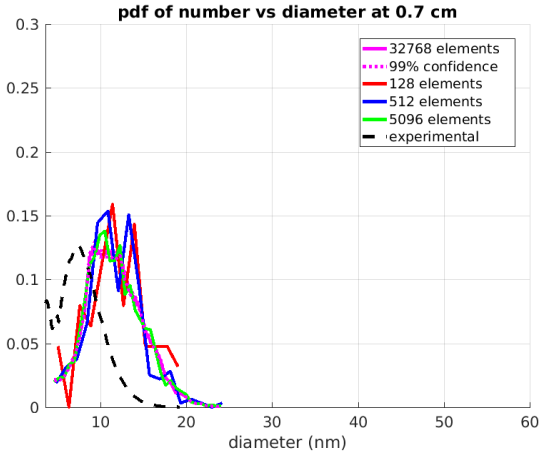

(c) 1.0 cm

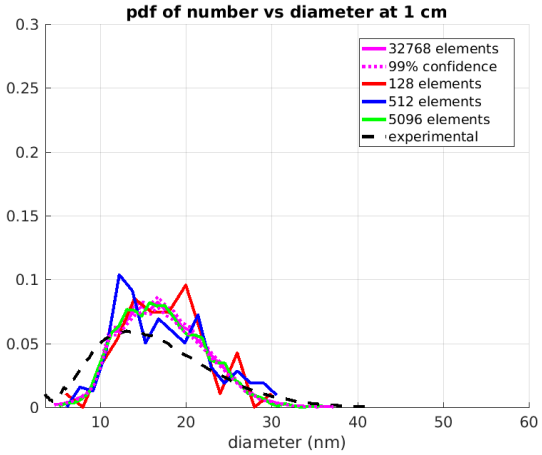

(d) 1.2 cm

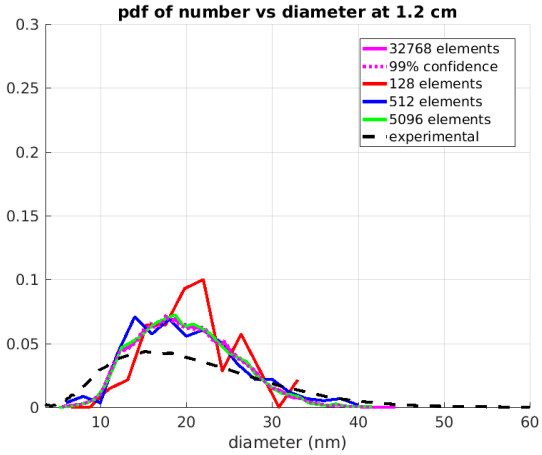

Figure 3.2: PSDs for flame HWA1 calculated using different ensemble sizes and measured. The plots are for the indicated height. The largest ensemble size (32768) is bounded by a 99 percent confidence interval.

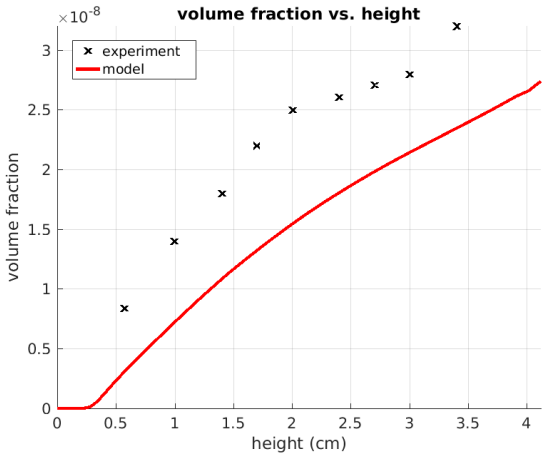

Figure 3.3: Measured and simulated volume fraction of soot for flame JW1.69

is still interpretable. For simulations using more than 256 particles, the numerical error is smaller than the features of interest.

To validate the soot model for physical approximation error, comparisons to measured results are used. Soot measurements are typically confined to metrics of the amount of soot and the size distribution of soot. Other soot metrics such as primary particle size, compactness, and uniformity are interesting but currently rely on unconventional and very intrusive measurement techniques [34]. The amount of soot can be expressed using the soot volume fraction.

Figure 3.3 shows a plot of the volume fraction of soot versus height. Agreement is within 10 percent difference over the entire measured range. Since soot is usually discussed in terms of orders of magnitude and similar agreement is used as validation elsewhere [14], this validates the model for values of soot quantity.

Measured normalized PSDs are compared to the simulated converged PSDs in Figure 3.2. Due to experimental measurement capability, the PSDs have a cutoff at 3.5 nm. Model results are also shifted by 3 mm (so the model PSD at 7 mm are from the model's results at 10 mm) to counteract mainly the effects of cooling in the measurement process [137, 138].

The PSD comparisons of Figures 3.2 show the model is able to capture the characteristics

of the measured data including the local maximum in location and magnitude, the largest particles present, and the general distribution of particle sizes to within approximately 20 percent deviation. Most disagreement is merely differences in timing. Early distributions of Figures 3.2a and 3.2b seem to be shifted to the right for instance. The insufficient shift may be due to increased sensitivity to cooling or abnormal cooling during measurement in the early stages of soot development.

Based on the validation steps in this section, the SWEEP model is sufficiently accurate in simulating soot amounts and distributions for the case parameters while using more than 256 stochastic particles.

3.3 Combustion validation

The current CFD and chemical kinetics approach has been applied to a range of spray and engine combustion cases using a variety of fuels; accordingly, only validation relevant to the present work is presented here. Further validation can be found in references [19].

Multiple cases are used in combustion validation for different aspects. The cases are chosen based on their prominence in literature, measurement capability, and propensity for soot. The first set is based on the industry standard Spray A conditions. Spray A is a diesel like injection into a domain that provides visual access with static boundaries, useful in validating flame lift off length. The second set is based on a light duty GM 1.9L diesel engine. Engine simulations are the prime motivation for the soot model and help to validate the numerical mesh and cylinder pressure.

Spray A combustion model validation

For the particular iteration of Spray A considered, dodecane is injected at 1500 bar for 5.8 ms into 15 percent oxygen, 1000K ambient conditions resulting in a pseudo-steady state duration from 1.8 to 5.8 ms after the start of injection. The Spray A test chamber used has a

viewing window from 15.2 to 67.2 mm used for soot measurements. Measured results used in this study are from Skeen et al. [111] except for OH images, due to availability. OH images are from Abraham et al. [97]. Despite not having the images of Skeen et al., the lift off length was published as 11.5mm which is very close to 12.2mm, reported by Abraham et al. [97]. Both of the experiments use the same Spray A conditions summarized in Table 7.1.

Table 3.2: Spray A experimental conditions

$T_{ambient}$	1000 K
$\rho_{ambient}$	22.8 kg/m^3
$O_2, ambient$	15.00 %
$N_2, ambient$	75.15 %
$CO_2, ambient$	6.23 %
$H_2O, ambient$	3.62 %
Fuel	c12h26
Inj. Duration	5.8 ms
Nozzle	90 μm
Injection Pressure	1500 bar
Pseudo-steady	1.8-5.8 ms
Light	blue (406 nm)

Table 3.3: Spray A simulation parameters

Simulation package	KIVA3v Rev 2 + ERC submodels
Soot model	Direct, One-way, Extended hybrid
Surrogate soot model	NA, NA, MoM & direct
Turbulent model	RANS (RNG k-ϵ)
Reaction Mech.	Multi component w/ PAH [101]
Mesh	Pseudo 2D
Base mesh (mm)	1.0

The case is simulated using an in-house computational fluid dynamics (CFD) code based on the KIVA family of codes [99]. The code includes improved physical models developed at the University of Wisconsin-Madison's Engine Research Center (ERC). The spray model uses the Lagrangian-Drop and Eulerian-Fluid (LDEF) approach. To reduce the grid size dependency of the LDEF spray model and allow accurate spray simulation on a relatively

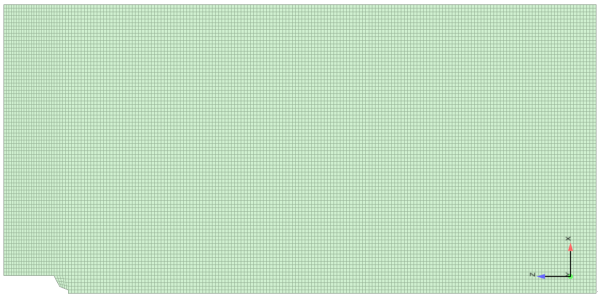

Figure 3.4: Spray A mesh with the injector tip in the lower left hand corner, injecting along the bottom edge

coarse grid, the Gasjet model of Abani et al. [1] is used to model the relative velocity between the droplets and gas phase in the near nozzle region. The Kelvin Helmholtz - Rayleigh Taylor (KH-RT) model was used to model the spray breakup [7]. The Re-Normalization Group (RNG) k-ϵ model was used for turbulent flow calculation [52]. The chemistry calculations were performed by SpeedChem, a sparse analytical jacobian solver coupled to the CFD [96]. A mesh size with a characteristic dimension of 1 mm was selected by performing a grid sensitivity study. It was found that this grid size gave an acceptable trade-off between accuracy and computational expense. The mesh used is shown in Figure 3.4. The simulation parameters are listed in Table 3.3. The current CFD approach has been applied to a range of spray and engine combustion cases using a variety of fuels; accordingly, only validation relevant to the present work is presented in this work. Further validation can be found in references [19, 115].

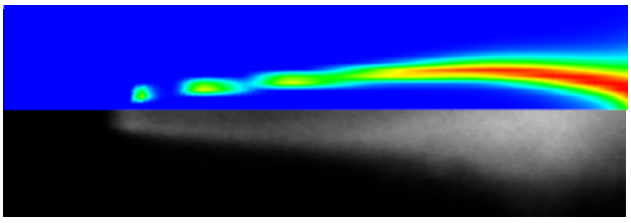

Figure 3.5: Spray A steady state lift off length (upper) simulated OH concentration (lower) measured OH chemiluminescence of Abraham et al. [97]. The image domain is 7.0cm long and 2.3cm wide.

Lift-off length is a common measure of simulation accuracy since it involves mixing and combustion. Figure 3.5 shows a comparison between the measured OH chemiluminescence and simulated OH mole fraction under pseudo steady conditions. In the figure, the injector is out of view on the left. The upper half is the simulated OH concentration across the center-plane at 4ms and the lower half is the ensemble averaged measured OH chemiluminescence. Both images are to scale and span the same domain. The overall jet structure is captured by the simulation well; however, the lift-off length is over predicted by approximately 3 mm. This agreement is similar to other studies (e.g., [113]) and is deemed acceptable.

GM 1.9L combustion model validation

Experimental data from a GM 1.9L four-stroke light-duty diesel engine was also used for validation of soot model due to the practical interest of engine soot as well as the SMPS measurement data available. These cases also provide a platform to validate the extended hybrid portion of the model. Before any portion of the soot model is validated, the combustion simulation must be further validated for the engine case, keeping the injection validation of Section 3.3 in mind. The experimental setup is explained in detail by Ross et al. [107] but the operating conditions will be mentioned here.

Table 3.4: GM 1.9L engine conditions

bore (cm)	8.2		
stroke (cm)	9.04		
speed (rpm)	1500		
CR	16.7		
BMEP (bar)	2.0		
EGR (percent)	30		
swirl ratio	2.2		
injector	7 x 140μm		
# of injections	3		2
3rd injection timing (CA deg. ATDC)	9	23	NA

The three operating conditions keep the same low, 2.0 bar BMEP, load while varying

the injection strategy. Fuel injections were made with a Bosch CRIN2 140um 7 hole injector Experimental conditions can be found in Table 3.4. In all three cases the pre injection charge is constant in timing and mass and small. The timing of the main injection is also constant across all three cases. In the 9 and 23 cases, the main charge is also small and constant, however, in the conventional case, the charge is increased to meet the load requirement. The timing of the start of injection of the third injection for the 9 and 23 cases is given by their title, and the mass of the injection is determined by the BMEP.

KIVA simulation

Table 3.5: KIVA GM 1.9L Simulation parameters

Simulation package	KIVA3v Rev 2 + ERC submodels
Soot model	Direct stochastic
Number of parcels	$\mathcal{O}(1000)$
Turbulent model	RANS (RNG k-ϵ)
Reaction Mech.	Multi component mechanism [101]
Mesh	Sector mesh
Characteristic length	0.6 cm

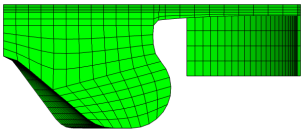

Figure 3.6: GM 1.9L KIVA simulation sector mesh at 7 deg. ATDC

These cases are simulated using two approaches, a KIVA based model and a Converge based model. An identical KIVA simulation setup used for the Spray A simulation of Section 3.3, but with a diesel surrogate and the corresponding sector mesh. Table 3.5 lists these parameters and Figure 3.6 shows the mesh at 7 deg ATDC.

The combustion simulation of the three investigated engine cases is validated by comparing pressure profiles to experimental measurements just like the earlier Converge simulations in Figure 3.9. Figure 3.9 shows simulated and experimental pressure profiles that match to

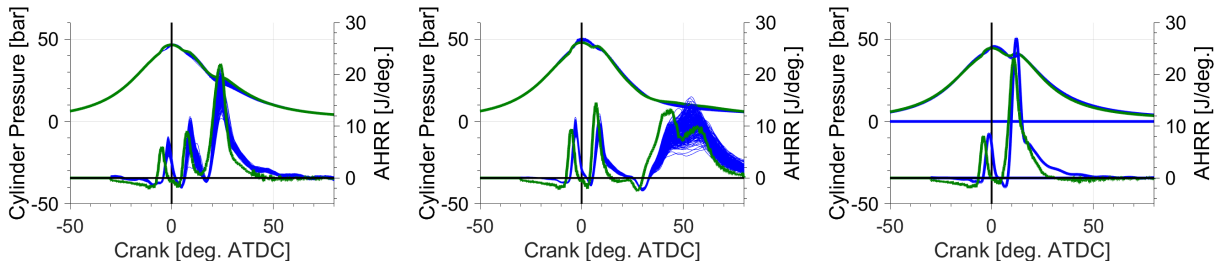

(a) 9 deg (b) 23 deg (c) conventional

Figure 3.7: Pressure profile and heat release rates for the indicated cases

within 5 percent. Again, the conventional diesel case, Figure 3.9c only has one experimental data-set. The agreement found here is similar to other studies (e.g., [61]) and is deemed acceptable for the present work.

Converge simulation

Table 3.6: Converge GM 1.9L Simulation parameters

Simulation package	Converge
Soot model	Extended hybrid model
Number of parcels	$\mathcal{O}(30000)$
Turbulent model	RANS (RNG k-ϵ)
Reaction Mech.	Multi component w/ PAH [101]
Fuel surrogate	$nC_{16}H_{34}$, C_7H_8 (90/10, %molar)
Mesh	Sector mesh
Base mesh (mm)	2
Nozzle outlet embed scale	3
AMR scale	3
Surrogate soot model	PM*

* Method of moments surrogate model was used because a similar method of moments surrogate model was used during validation.

For the converge simulations, similar simulation parameters to those used for KIVA were used however some of the ERC models are missing. The spray model uses the Lagrangian-Drop and Eulerian-Fluid (LDEF) approach with the Kelvin Helmholtz- Rayleigh Taylor (KH-RT) model to model the spray breakup [7]. The Re-Normalization Group (RNG) k-ϵ model was used for turbulent flow calculation [52]. The chemistry calculations were performed

using SAGE, a detailed chemistry solver [103]. Automatic mesh refinement (AMR) was used with a base mesh size of 2 mm and an AMR scale of 3. The simulation parameters are listed in Table 3.6 and Figure 3.8 shows the mesh at 7 deg ATDC.

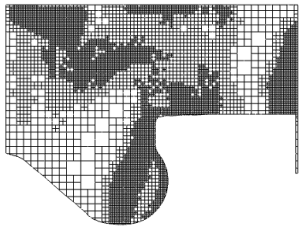

Figure 3.8: Representative GM 1.9L Converge simulation sector mesh at 50 deg. ATDC

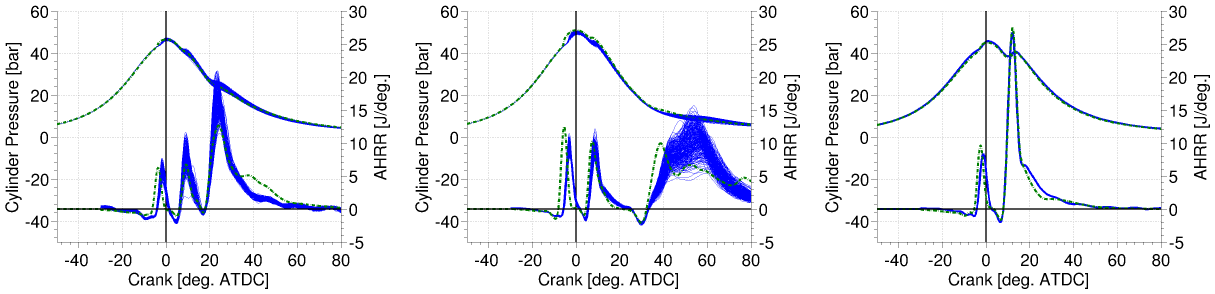

(a) 3rd SOI 9 (b) 3rd SOI 23 (c) conventional

Figure 3.9: Pressure and apparent heat release rate profiles.

The combustion simulation of the three investigated engine cases is validated by comparing pressure profiles to experimental measurements. Figure 3.9 shows simulated and experimental pressure profiles that match to within 5 percent. The conventional diesel case, Figure 3.9c only has one experimental data-set. The conventional diesel injections both occur relatively early and are much more stable than the later third injection of the other two cases leading to a much smaller standard deviation in measured results. The agreement found here is similar to other studies (e.g., [61]) and is deemed acceptable for the present work.

3.4 Soot LPEF representation validation

In this section the use of a LPEF coupling between soot and the momentum, energy, and species fields are validated.

Dimensionless numbers / validating model assumptions

The LPEF coupling assumptions created in Section 2.1 are validated using dimensional analysis, numerical studies of the interested phenomenon, or by comparing to similar assumptions in literature.

- Soot closely follows Eulerian flow

  Because of soot particles low inertia and relatively high surface area per volume due to their agglomerate based structure, soot is commonly assumed to follow the surrounding gas flow perfectly [65]. To validate these assumptions, the principle phenomenon will be analyzed via the dimensionless Stokes number,

$$St = \frac{t_{\text{relax}} \cdot u_{\text{inf}}}{l_{\text{char}}} \tag{3.1}$$

  where t_{relax} is the relaxation time of the particle, u_{inf} is the far field velocity, and l_{char} is the characteristic length of the particle. The Stokes number is a ratio of the reaction time of the particle to the characteristic time of the flow. For our interest, the characteristic length and time of the flow are given by the average piston speed and stroke. The reaction time of the particle is given by time it takes for the particle to reach the characteristic velocity of the flow, i.e.the characteristic velocity over the acceleration of the particle. The acceleration of the particle is calculated using the Cunningham Stokes equation,

$$F_{viscous} = \frac{6\pi m u_{air} U a}{(1 + \frac{\lambda}{a}(C_a + C_b exp(\frac{-C_c a}{\lambda})))}, \tag{3.2}$$

with Basset slip correction factors to extend its accuracy into the transition regime [6]. The transition regime extending into Knudsen numbers on the order of $1e-10$ is where the incipient soot particles exist. If the Stokes number is large, this equation is not valid and the analysis needs to be redone. Particles are assumed to be spheres for simplicity even though that assumption is certainly wrong, with soot having a fractal dimension closer to two than three. This error should not be large enough to change the conclusion. Soot characteristics were based on coal values.

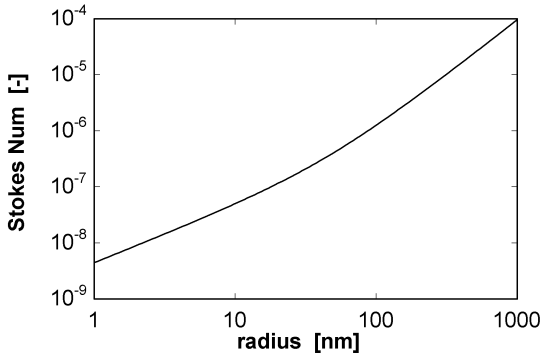

Figure 3.10: Stokes number versus particle size

Figure 3.10 shows the Stokes number as a function of particle size for engine relevant conditions.

The Stokes number grows quicker than particle size, however, for all particles smaller than 1000 nm the Stokes number remains smaller than unity; accordingly, the motion of the parcels is assumed to perfectly follow the Eulerian gas phase.

- Soot particles do not diffuse

  Soot is very sparse and heavy relative to gas phase molecules, causing diffusion to be very weak. Looking at the diffusion coefficient of species i into j based on the kinetic theory of gas,

$$D_{\mathrm{ij}} = \frac{2}{3}\sqrt{\frac{k_{\mathrm{j}}^3}{\pi^3}}\sqrt{\frac{1}{2m_{\mathrm{i}}}+\frac{1}{2m_{\mathrm{j}}}}\frac{4T^{3/2}}{P(d_{\mathrm{i}}+d_{\mathrm{j}})^2}\,, \tag{3.3}$$

and the diffusion velocity [41]

$$u_i = -\sum_{j=1}^{N} D_{ij}\mathbf{d}_j \tag{3.4}$$

$$\mathbf{d}_j = \nabla P_j + (P_j - Y_j)\,\nabla(\ln P), \tag{3.5}$$

where N is the number of species, P_j is the partial pressure of species j, and Y_j is the mass fraction of species j. it is clear that if $m_{\text{soot}} \gg m_{\text{gas molecules}}$ and $d_{\text{soot}} \gg d_{\text{gas molecules}}$ and the total pressure gradient is small, diffusion of soot will not be driven by the gas phase. This means soot diffusion relies on the gradient of partial pressure of soot, ∇P_{soot}. For typical soot concentrations measured in parts per million, the partial pressure of soot, even in the sootiest regions, is very low and the resolution of the RANS based mesh will certainly obscure any gradients strong enough to drive diffusion. The dimensionless Brownian diffusion velocity is much smaller than the dimensionless thermophoresis velocity in boundary layers, showing thermophoresis is a much stronger driver, as Blake et al. [116] and Kittelson et al. [67] have calculated. For these reasons diffusion is often neglected in literature [39, 91, 93, 116].

- Soot particles are at surrounding temperatures

  Soot particles, although larger than gas phase molecules, are still very small, have little thermal mass, and undergo frequent energy transfer collisions with the gas phase at engine like pressures. The thermal time constant of a soot particle will indicate the accuracy of this assumption. The thermal time constant is defined here as the time it takes a particle to loose 10 percent of its thermal energy. The heat rate and thermal capacity of a particle need to be calculated.

  Because soot primary particles are often in the transition regime, continuum based heat transfer models may overpredict the heat of soot. The Fuch's boundary sphere model [40], used here, adds a shell to the soot particle beyond which continuum mechanics are valid. Within the shell, ballistic heat transfer calculations are used. To solve the

problem, the heat leaving the shell must be equal to the heat leaving the particle. The concept is similar to the law of the wall. The Fuchs boundary sphere method has been shown accurate by Liu et al. [79]. In the continuum regime the classic Fourier's law models heat.

In the free molecular regime, ballistic heat is modeled by solving for the flux of gas molecules impacting the soot particle and the energy transfer of each impact. For a monodisperse stationary gas,

$$q_{fmr} = C_T \pi a^2 P \sqrt{\frac{2k_b T_g}{\pi m_g}} \left(\frac{\gamma+1}{\gamma-1}\right) \left(\frac{T_\delta}{T_p - 1}\right), \tag{3.6}$$

where a is the particle diameter, T_g is the temperature of the gas, m_g is the mass of the gas, and C_T is the thermal accommodation coefficient, gives this heat [24].

The thermal capacity of a particle was calculated as that of a coal sphere with an initial temperature of 1000 K. Again, particles are assumed to be spheres for simplicity and soot characteristics were based on coal values. The spherical shape is worst case scenario.

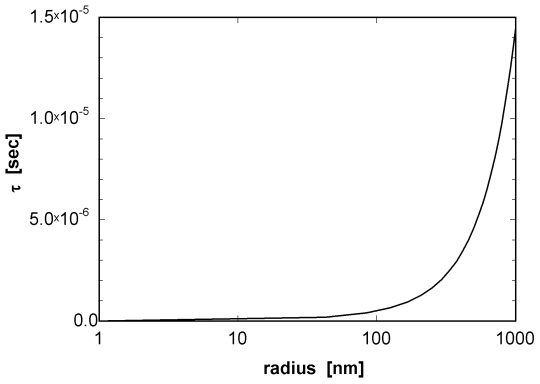

Figure 3.11: Thermodynamic time constant versus particle size

Figure 3.11 shows the thermal time constant of the soot particle as a function of particle size. For all particles, the thermal time constant is an order smaller than the simulation

flow time scale. Accordingly, the parcel temperature is assumed to be at equilibrium with the surrounding gas. This is a common assumption [79].

- Volume fraction is negligible

  For even the most sooty conditions, the volume fraction of soot is still measured in parts per million. Considering the resolution of the simulations in this work and other known errors, this assumption is founded. Similar assumptions in literature for fuel droplets and soot are prevalent [47].

- Radiation is negligible

  Neglecting radiation is a very common assumption is simulation studies [24, 113] because of its computational expense. Its validation comes from studies like that of Zheng et al. [139] which finds the volume fraction of soot in an ethylene diffusion flame changes by less than 15 percent when simulationg radiation. A radiation model is proposed in the future work, §8.

0D coupling convergence

The Spray A simulation will be used to validate the coupling between 0D SWEEP simulations and the total 3D simulation. The soot model is phenomenological, so it does not have tuning parameters. It does have parameters affecting its implementation, however. They are the number of parcels, or subdomains, covering the simulation domain and the number of stochastic particles in every subdomain's soot simulation. As the number of parcels is increased, the homogeneous assumption made of the subdomains they represent becomes more valid, however, the computational cost also increases.

A convergence study is used to determine an adequate number of parcels. In these convergence studies, all simulation parameters are identical except for the parameters studied or noted. Figure 3.12 shows domain cumulative PSDs at 5ms for simulations using different

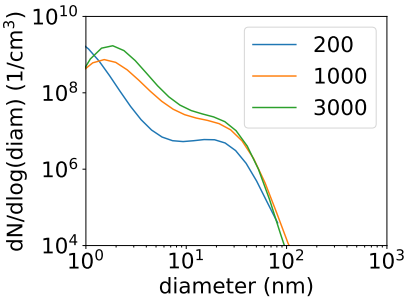

Figure 3.12: PSDs of domain at 5ms as calculated by simulations with the indicated order of parcels

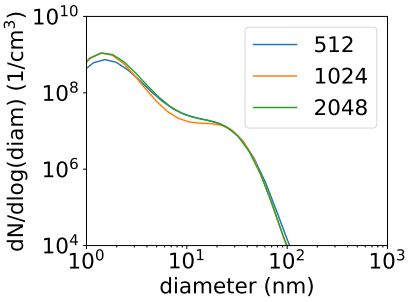

Figure 3.13: PSDs of domain at 5ms as calculated by simulations with the indicated number of particles

numbers of parcels. Approximately 1000 parcels is sufficient for a PSD that matches the converged solution. The law of large numbers states that values determined via the Monte Carlo method will approach the actual values as the subset approaches the actual set [88]. So, a convergence study can be used to determine an adequate number of particles. Figure 3.13 has similar information to Figure 3.12 but varying the number of particles. 512 particles is sufficient for a PSD that matches the converged solution.

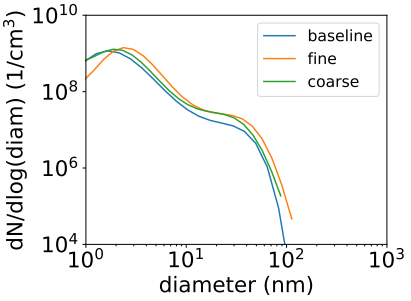

Figure 3.14: PSDs of domain at 5ms as calculated by simulations with the indicated mesh

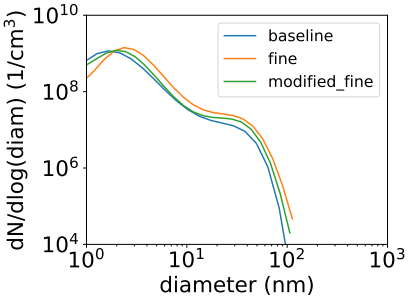

Figure 3.15: PSDs of domain at 5ms as calculated by simulations with the indicated mesh and modifications

The soot model can also be affected by general simulation parameters that influence the subgrid scale resolution and fields, like any model, such as the mesh resolution, interpolation

schemes, etc.. The danger in substantially reduced mesh resolution for the model is losing areas of exceptional equivalence or other important variables to soot production [30]. Figure 3.14 shows the PSDs for simulations with three different resolutions. The base resolution, as listed in table 7.2, is 1 mm, the fine resolution has a characteristic dimension of 0.25 mm and the coarse resolution has a characteristic dimension of 2 mm. The different meshes generate different numbers of parcels as well, indirectly relating a study in mesh size to the study of Figure 3.12. All of the meshes produce very similar PSDs indicating the mesh based RANS filter length is sufficiently small to capture features important to soot. The largest variation comes from the fine mesh case, in which the incipient mode has fewer small particles. Figure 3.15 shows the PSDs for the baseline and fine simulations as well as the fine simulation with the B1 spray breakup constant changed from 60 to 90. The B1 parameter is a model fitting parameter that corresponds to the disturbance in the liquid droplets and how quickly they breakup. The purpose of changing B1 is to recover the PSD of the coarse mesh by changing a spray modeling parameter, indicating apparent mesh dependence of the soot model may actually be mesh dependence of the spray breakup model. By varying the spray breakup model parameter the baseline PSD is retrieved.

Figure 3.16 shows surfaces of the same format as 4.1 colored by temperature for the baseline mesh, the fine mesh, and the fine mesh with the altered spray breakup constant. Although there are plenty of differences between the baseline and fine mesh surfaces, the figure with the altered constant matches the baseline surface better in terms of temperature shortly after the injector tip, up till about 4 cm. This region is especially important to the production of incipient mode particles, as will be seen in Figure 4.3. This indicates differences upstream of the soot model, in the spray breakup model, might be responsible for the deviation in the soot results when refining the mesh.

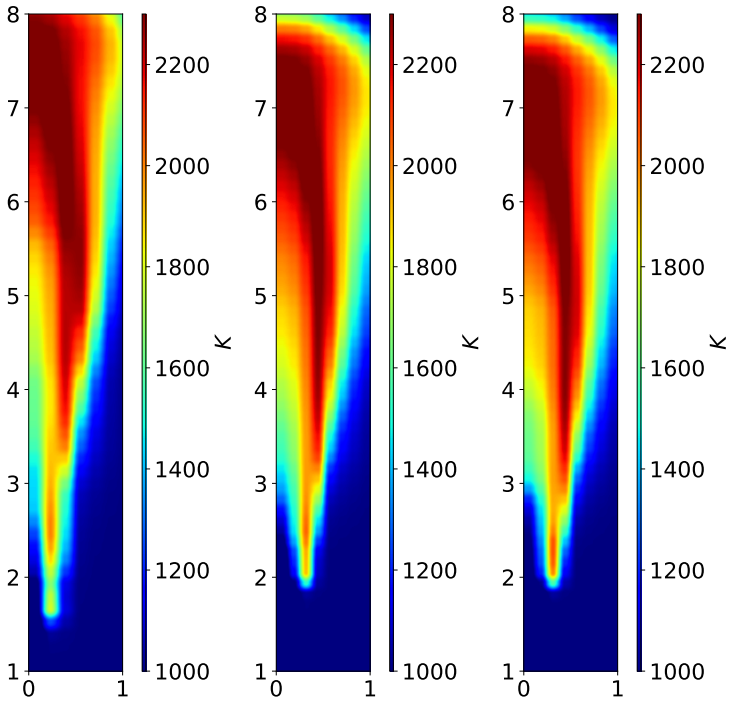

(a) baseline mesh (b) fine mesh (c) fine mesh with a breakup value of 90

Figure 3.16: Surface plots of the time averaged temperature using the indicated mesh. Surfaces are bisections of the central axial plane.

3.5 Extended hybrid model

Spray A forms the basis for extended hybrid model verification because of its lack of additional confounding dynamic domain effects present in engine simulations. Multiple simulations using the direct, one way, and extended hybrid models were run for comparison and validation. The simulation parameters are shown in Table 3.3.

Figure 3.17 shows the pyrene concentration over time as predicted by the direct, one-way, and hybrid model with a MoM surrogate model. The one-way model fails to capture the consumption of the inception species by soot generation. The direct and extended hybrid model concentrations are within approximately an order of magnitude indicating the surrogate soot model is approximating the consumption of the direct model. This validates the use of a surrogate soot model in capturing the effects of the direct model.

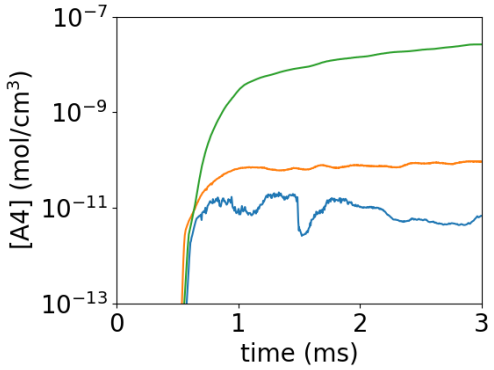

Figure 3.17: Pyrene concentration over time. direct (blue), one-way (green), extended hybrid w/ MoM surrogate (orange)

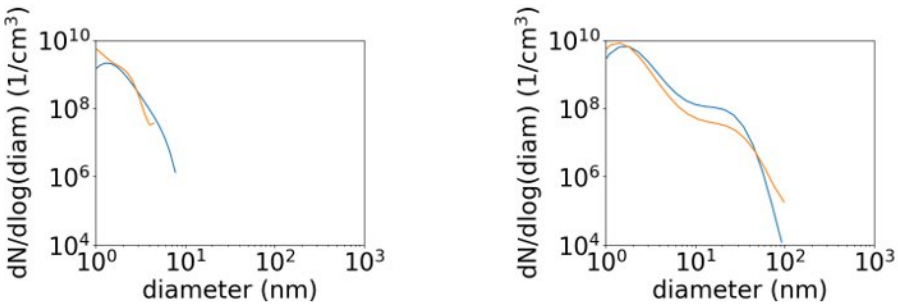

(a) 0.5 ms

(b) 2.0 ms

Figure 3.18: PSDs produced using the direct model (blue) and the extended hybrid w/ direct surrogate model (orange). PSDs are sampled at the indicated time.

Figure 3.18 shows PSD comparisons at two different times for the direct and extended hybrid model. The extended hybrid model is using the direct model as a soot model surrogate. i.e. any differences between the two lines are due to the implementation of the extended hybrid model. The lines are almost identical, indicating the extended hybrid model reclaims the direct model results if the surrogate model is close enough. This validates the decoupled method of making parcels in postprocessing.

The combined validation of a surrogate model to capture the direct model's effect and the method of generating Lagrangian parcels in postprocessing validates the complete extended hybrid model.

3.6 Cumulative validation

As stated before, this step is redundant, but it is comforting.

The same cases used in the combustion validation are used again here. The visual access of axially symmetric Spray A provides access to measurements that can be processed into spatially resolved soot volume fraction data. Again, engine simulations are the prime motivation for the soot model. Soot mass and size distribution data are simultaneously collected from the exhaust.

GM 1.9L

Engine soot PSD data was collected by Ross et al. [107] for all of the cases of Table 3.4. Exhaust gases were probed, diluted to arrest coagulation and surface reactions, and then denudered to remove volatiles. Experimental data is compared to simulation results at the time of exhaust valve opening despite the added processes during measurement. The exact effects of these processes are subject to criticism, however, it is reasonably certain that particle diametrical properties do not drastically change, where larger particles are more stable [10]. Finally, particle mobility diameter is measured with a scanning mobility particle sizer (SMPS) capable of measuring diameters from 7 to 300 nm.

Figure 3.19 shows comparisons of simulated and measured PSDs for the three cases. Five measurements were taken of the SOI 9 case, 8 of the SOI 23 case, and only one conventional case. Both sets with multiple measurements had a standard deviation of about 1e5 particles, meaning the error band of the experimental data is very narrow with respect to the measurements taken. This does not account for sources of systemic error discussed earlier. There are two sets of simulated results, the extended hybrid and particle size mimic results. Measured PSDs for the SOI 9 and conventional cases are similar, with an obvious mode of accumulation particles with a maximum of approximately 1e7 particles per cm^3 at about 80 nm. They also show tails trending toward larger populations of incipient particles

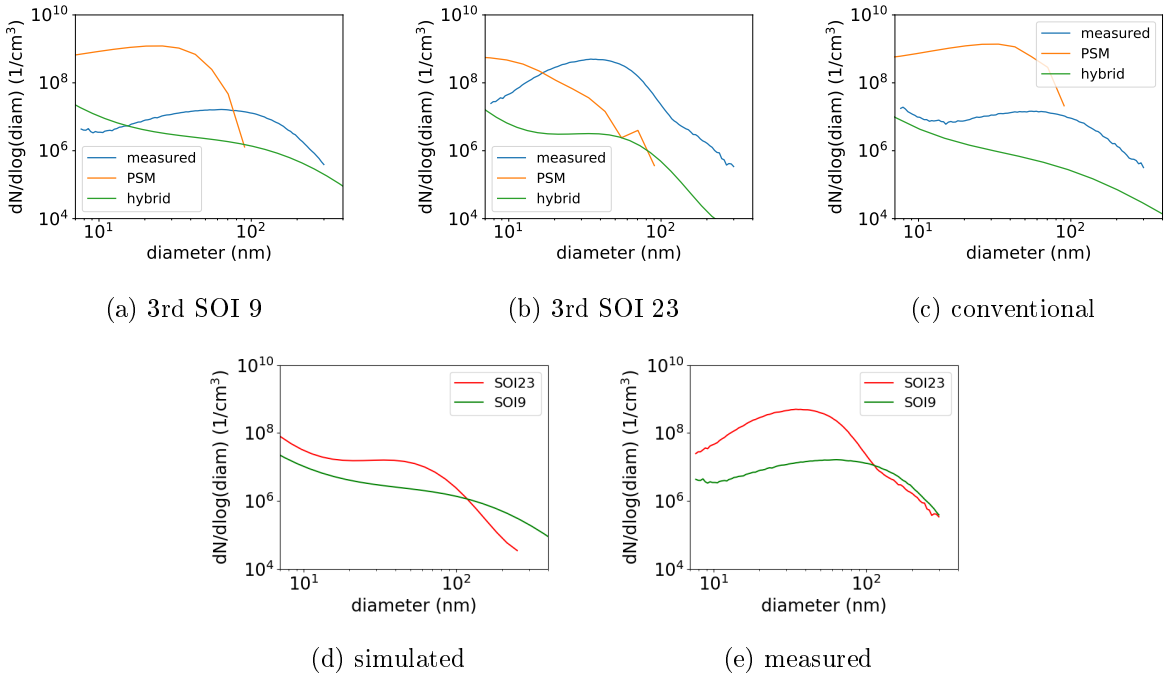

(a) 3rd SOI 9 (b) 3rd SOI 23 (c) conventional

(d) simulated (e) measured

Figure 3.19: Measured and simulated PSDs at EVO from the GM 1.9L cases. Simulations use the extended hybrid soot model.

before the measurement limit of 7 nm. The SOI 23 case is obviously different, showing a much larger concentration, about 1e9 particles per cm^3, of smaller particles, peak of about 30 nm. There is also no tail trending toward a large incipient population in the SOI 23 case however, because the population is so much larger, the concentration of the smallest measurable particles is still larger than the other two cases with tails. The extended hybrid results match the pattern of the SOI 9 and conventional cases being similar while the SOI 23 is is obviously different. Comparing the SOI 9 or conventional cases to the SOI 23 case shows the empirical behavior of a larger midsized population is captured. The more gradual trend from incipient mode to accumulation mode in the SOI 9 and conventional case compared to the more defined accumulation mode of the SOI 23 case is identifiable. In Figure 3.19 the agreement between simulations and measured data is generally within an order of magnitude and always well within two orders over the complete measured range. The largest deviation between simulations and measurements occurs at the local maximums where the simulations

under-predict the modal behavior. All simulations are under-predicted by approximately the same magnitude, with the larger modes, Figure 3.19b, having slightly more under-prediction. Although the matches are imperfect, the empirical behaviors are captured, and the deviation is consistent between all extended hybrid simulations and measured results. The PSM results worse off. They still capture that the conventional and SOI 9 cases are similar however, they are both very dissimilar to the measured results, having a much smaller but much denser population of particles. The SOI 23 case also predicts a much smaller maximum particle size with no empirical trend matching. This validates the extended hybrid soot model for qualitative results.

4 MODEL APPLICATION: SOOT OPTICAL PROPERTIES

4.1 Motivation

The scientific method for developing an understanding consists of creating a theory based on observations and then confirming the theory with further observations/measurements [29]. Often theory outpaces measurement capability. Simulation is a stopgap between theory and experimentation. Simulations can be considered virtual experiments based on theory and can be used as a temporary replacement for actual experimentation. Historically simulations have been used with great effect to advance understanding. Examples of fundamental theories that were first hypothesized using simulations and later confirmed experimentally include:

- Turbulent boundary layers - As Reynolds number increases, log-law of wall is more accurate than power-law. Na Moin et al. [89] identified the behavior in 1998 using DNS simulation. Multiple experiments including those from 2006 by Lögdberg [81] are consistent with the simulated findings.

- Richtmyer-Meshkov Instability - Interface instability created by acceleration through a density change Through a harrowing application of finite difference methods, Richtmyer [104] discovered RMI in 1960. In 1970 Meshkov [85] confirmed the simulations.

Soot is one such area steeped in many theories that are still waiting for measured validation. Soot measurement often relies on assumptions of uniform soot or similar obviously flawed statements. SMPS measurements are common in quantifying the soot in engine exhaust [49, 76] however, in practice, they occur far from the exhaust valves and only after significant pretreatment. After leaving the cylinder, the exhaust is typically diluted and cooled to arrest coagulation and surface reactions and then maintained at temperature in a denudering process to remove volatiles and subincipient soot particles. During these processes, continued coagulation and oxidation occur at uncertain rates, although there has

been some research quelling these concerns [49]. Soot deposition on walls in the measurement probes is also an unvetted concern that may be highly dependent on thermophoresis. Additionally, SMPS samples are volumetric and time averages, giving no resolution that may be useful for soot growth. These problems make SMPS results questionable when trying to validate a soot models for engine simulations.

KL extinction measurements are an attractive alternative because they solve many of the mentioned problems. Using planar light sources and rapid cameras, both time and space soot information can be resolved. Additionally, aside from the radiation of the light source which is likely inconsequential, the measurement process is non-invasive.

There are limitations to KL extinction measurements however. The most obvious is the required optical access in processes that typically work best at high pressures, temperatures, and with oil. Spray A is a standardized test, intended to exhibit real-world diesel combustion phenomenon and effectively designed around KL extinction measurements by maximizing optical access. Although KL extinction provides one of the best ways to passively sample soot, KL extinction measurements have additional, less obvious, problems. To produce volume fraction measurements with KL extinction, assumptions on the uniformity of soot are required. For instance, it is typical to use an empirically determined constant value of $(1 + \alpha_{sa})E(m_o) = 0.26$ [84] due to a lack of alternative soot information.

Unfortunately, soot has complicated absorbency properties making m_o and α_{sa} functions of soot particle morphology [73]. For instance, because of their size, incipient mode particles likely contribute very little to the extinction despite their typically substantial contribution to the total soot population, and extinction due to large particles is likely related to the particles' fractal dimension with more dense particles having a greater impact. In the work of Skeen et al. [111], two light sources with different wavelengths were used to measure the optical thickness of soot. Then the differences between the calculated values were analyzed as an indicator of nonuniform optical soot properties. The variability in optical properties

reduces the accuracy and usefulness of KL extinction measurements for soot, regulating them to qualitative observations [73].

In the following work, the direct soot model will be used in combination with light scattering models to predict the attenuation of soot as a function of space for the Spray A case. Simpler soot models, such as the sectional soot model, would not be able to generate the following analysis because of their lack of particle shape information. These results will then be used to find the error associated with a uniform soot properties assumption. These same assumptions are used in reported measured volume fraction results and a comparison between the simulated and measured results will be performed.

4.2 Theory

Light extinction measurements are used to quantify the concentration of an opaque substance along a path. The transmittance,

$$\frac{I}{I_0} = \exp\left(-K_e L\right), \tag{4.1}$$

where $\frac{I}{I_0}$ is the ratio of collected light intensity with and without soot, gives the optical thickness, $-K_e L$, of the volume that the light passes through.

More generally, if the volume the light traverses is not uniform

$$K_e L = \int_{Z_{-\inf}}^{Z_{\inf}} K_e dz. \tag{4.2}$$

The extinction coefficient, K_e, is given as a sum over the particles in the path

$$K_e = \sum_{i=1}^{M0 \cdot dV} \frac{\sigma_i^2 \pi Q_{ei}}{dV}, \tag{4.3}$$

where σ is the optical attenuation radius, dV is a differential volume, $M0$ is the particle concentration in that volume, and the extinction efficiency is the sum of the scattering, Q_s,

and absorption, Q_a, efficiency,

$$Q_e = Q_s + Q_a \tag{4.4}$$

[135].

Small particle Mie theory gives models for Q_s and Q_a of a single particle assuming the particle is spherical. For particles in the Rayleigh limit, where

$$x_p = \frac{\pi\sigma}{\lambda} \tag{4.5}$$

is less than 1, Q_a can be approximated by

$$Q_a = 4x_p Eo(m_o) \tag{4.6}$$

where

$$Eo(m_o) = \Im\left(\frac{m_o^2 - 1}{m_o^2 + 2}\right). \tag{4.7}$$

Q_s can be approximated by

$$Q_s = \frac{8}{3}x_p^4 Fo(m_o) \tag{4.8}$$

where

$$Fo(m_o) = \left|\frac{m_o^2 - 1}{m_o^2 + 2}\right|^2. \tag{4.9}$$

If the domain is further assumed to be monodisperse then the total expression for K_e collapses to

$$K_e = f_v \frac{6\pi}{\lambda}(1 + \alpha_{sa})Eo(m_o), \tag{4.10}$$

where α_{sa} is the scattering to absorption ratio and f_v is the volume fraction. In extinction measurements reproducing the soot volume fraction field, as in Figure 4.1a, it is typical to use this relation with an empirically determined constant value of $(1 + \alpha_{sa})Eo(m_o) = 0.46$ [84] due to a lack of alternative soot information, despite studies [130] showing soot particles spanning a wide array of not only size but also form, throughout a combustion event. Other

literature [17, 135] assumes a zeroth-order log-normal distribution of soot particle sizes in a polydisperse volume to create a relation requiring soot population moments. Rayleigh-Debye-Gans theory gives the scattering efficiency for a porous sphere as

$$Q_s^{'} = Q_s Y_a. \tag{4.11}$$

The porous sphere has been adopted to soot by Dobbins et al. [28] using a model for Y_a

$$Y_a = k_f \left(\frac{3D_f}{16x_p} \right)^{D_f/2} \tag{4.12}$$

An empirical correction of the extinction efficiency given by Mackowski et al. [83],

$$Q_e^{'} = Q_s + log(n_p) Q_a, \tag{4.13}$$

accounts for the aggregate nature of a soot particle. In this work, assumptions will be made when lacking the requisite information to use an applicable model, such is the case for the refractive index of soot, or when the available information is not exactly the value required, such as the attenuation diameter. The attenuation diameter was given by the soot chemistry collision diameter due to their similar purpose of representing the likelihood of getting in the way of particles or light. Soot particle bound and free electron densities used for refractive index models, such as the Drude-Lorentz dispersion model, are not immediately provided by the soot model used so the literature prevalent constant refractive index of $1.57 + 0.56i$ will be used for soot. Zhang et al. [135] collected data from multiple studies to find a refractive index of $1.57 + 0.56i$ an average soot value.

4.3 Case Setup

The case being simulated is the Spray A test used by Skeen et al. [111] and described in section 3.3

4.4 Results

Using KL extinction methods, volume fraction measurements were taken by Skeen et al. [111] during quasi steady state, after the spray head leaves the viewing window and until the end of injection, beginning at 1.8ms and going until 5.8ms. More details on the measurement methods are given in [111].

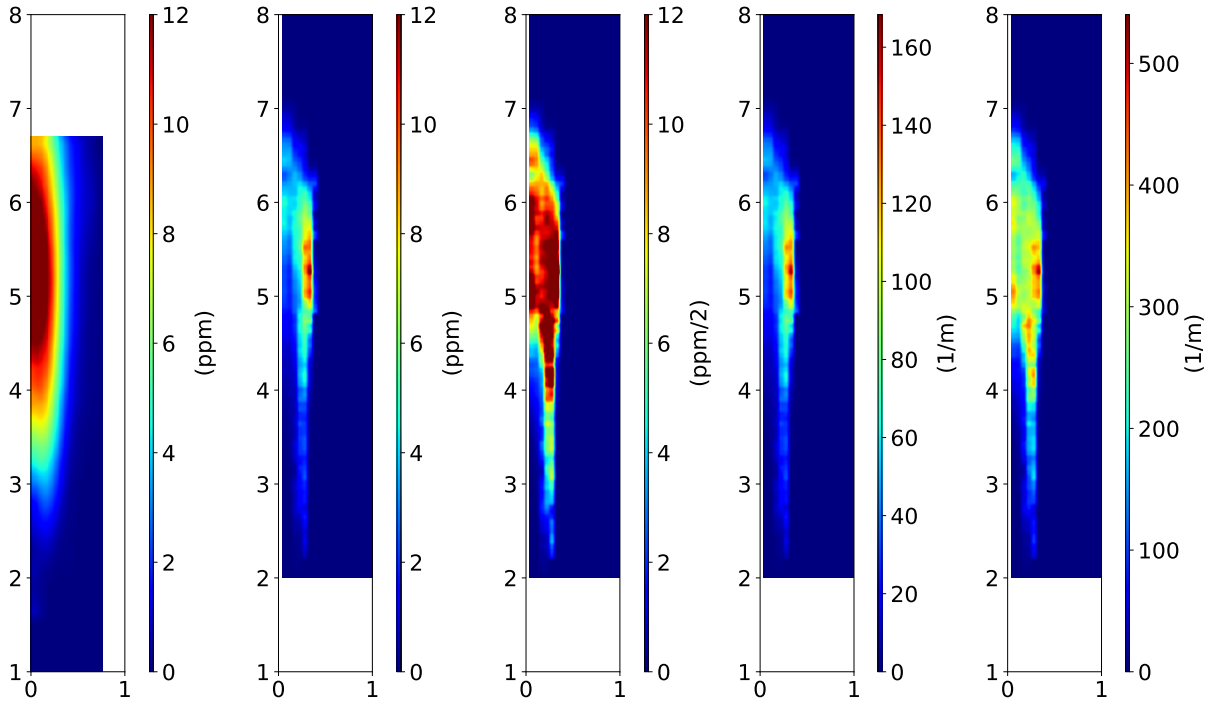

(a) volume fraction based on measurements

(b) simulated volume fraction

(c) expected measurement based volume fraction using the optical properties of soot found in the simulation

(d) average extinction coefficient calculated by assuming all soot has the same optical properties

(e) average extinction coefficient calculated using Equation 4.3 with the extinction efficiency given in Equation 4.13

Figure 4.1: Surface plots of the time averaged indicated value. Surfaces are bisections of the central axial plane.

Figure 4.1 shows surfaces colored by the corresponding scale for the indicated value. The injector tip is out of view in the lower left-hand corner at $(0, 0)$. The surfaces represent the right half of the axisymmetric central plane of the jet with time averaged values over

the pseudo steady state range. Figures 4.1a and 4.1b compare the measurement based and simulated volume fraction. The simulated volume fraction has much steeper gradients than the measurement based results, however, both share some distinctive features. Both have wings preceding the main sooty body where there is a higher volume fraction in the perimeter than in the core. The measurement based wings are much softer and end much sooner than the simulated wings. In general, the simulated sooty volume fraction body seems to be shifted further away from the injector nozzle and most of the sooty region's core near the axis seems to be missing. Magnitude wise the simulated and measurement based volume fraction are in very good agreement, especially for soot results. As stated earlier, the measurement based results assume soot is monodisperse and has constant optical properties. The following is an investigation into the validity of that assumption.

4.5 Analysis

Particle Size Distributions

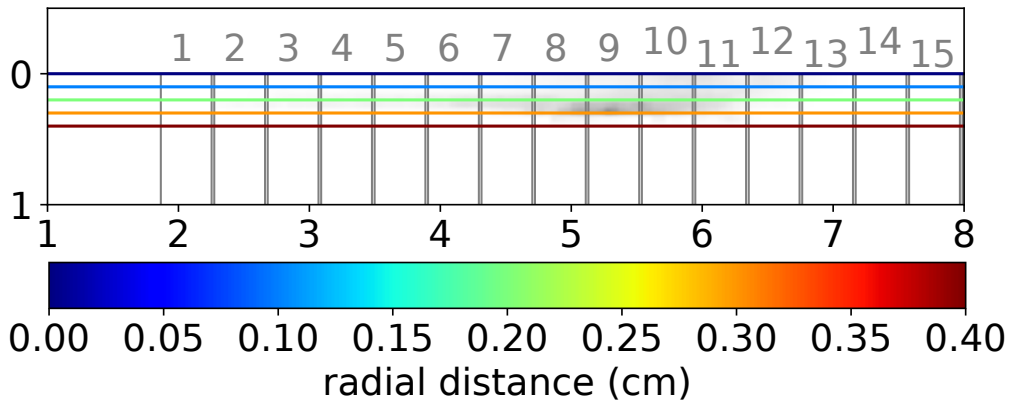

Figure 4.2: Map of locations for PSDs in Figure 4.3. Numbered box corresponds to plot number and colorbar corresponds to radial distance. For example, the orange PSD curve in Figure 4.3.10, was constructed from the soot at an axial distance of approximately 5.75 cm and a radial distance of 0.3 cm. The surface is colored by the volume fraction, similarly to Figure 4.1b, but in greyscale.

Figure 4.3 shows a collection of local PSDs over the entire Spray A domain. Particles are sized according to their electrodynamic diameter. The number of the plot corresponds

to the PSDs axial location and the color of the PSD corresponds to is radial location. The bold black PSD is the cumulative radial PSD for that plot's corresponding axial location. The map to interpret the location of the PSD is shown in Figure 4.2. Figure 4.2 is a surface of Spray A colored by the simulated volume fraction in greyscale. The color legend, however, corresponds to the radial distance from the jet centerline. The PSD colors of Figure 4.3 follow the same radial location legend. The zones corresponding to the plots of Figure 4.3 are also numbered in Figure 4.2.

A significant realization not necissarilly related to the optical properties of soot is that a regions average PSD is a construction of many sets of particles with different histories that often have very different PSDs than the average. Before these results, it seemed possible that every subset of particles in a certain region would quickly adapt to the PSD that that region allowed and would have roughly the same PSD as the larger set's average and every set its vicinity. This is certainly not the case. This observation is not possible with Eulerian based soot models because the local history of the particles is not preserved; a big particle is a big particle. Its also not possible with simpler parcel tracking models without any coupling to the Eulerian field because there is no way to define a spacial average between two different Lagrangian parcels with no volumetric representation.

Soot evolution in the jet as it is transported downstream is easily visible in Figure 4.3. The progression from inception at roughly 2.5cm (Figure 4.3.3) to mature soot, 5cm (Figure 4.3.9), and finally into decay, 6.5cm (Figure 4.3.13), can be identified by moving axially away from the injector.

Moving radially away from the injection axis shows different patterns depending on the axial location. 3cm (Figure 4.3.5) downstream from the nozzle, the largest particles are found in an annular region, bounded internally and externally by smaller particles. At approximately 4cm (4.3.7) the largest particles are represented at the perimeter of the sooty region and smaller near the axis. Finally, at approximately 5.25cm (4.3.10) all radial locations

exhibit some fully mature particles, however, there is still a slight radial gradient from the smallest to largest particles. Going further downstream, PSDs collapse as the sooty region narrows to a point. Beyond 5.25cm, perimeter PSDs exhibit the most diversity in mature and medium sized particles while central PSDs are typically more concentrated at a single largest mode. It is clear that although the section averaged PSDs (Black curves of Figure 4.3) maintain a relatively similar shape over much of the domain, bimodal with a maximum diameter of about $100nm$, the constitution of said PSDs varies greatly. Based on the complex variability of PSDs with respect to location, the relation between particle size and particle type is worth investigation.

Particle Form

Figure 4.4 shows surface plots in a similar format to Figure 4.1, however, Figure 4.4a is colored by the average particle optical attenuation diameter, Figure 4.4b is colored by the average number of primary particles per soot agglomerate, Figure 4.4c is colored by the average particle extinction efficiency, $Q_e^{'}$ from Equation 4.13, and Figure 4.4d is colored by the number of soot particles per volume, $M0$ from Equation 4.3.

Figs. 4.4a and 4.4b are both plots indicating the average soot particle type in a given region. Figure 4.4a shows that in the body of the sooty region, particles at the core have a smaller attenuation diameter than the surrounding particles despite having roughly the same electrostatic diameter as shown in Figure 4.3.10. Figure 4.4b provides some explanation, showing particles nearer to the core having more primary particles on average, effectively lowering their fractal dimension and making the particle less compact. The same relation is visible at the head of the sooty region (i.e., along the axis). As the particles move into the oxidizing region, they trade compactness for primary particles. These figures continue to show that the particle population is not uniform and the prevalent particle types are a strong function of location. Due to this variability and attenuation's reliance on particles'

form, the investigation continues to a model for the optical extinction coefficient based on particle shape.

Particle Optics

Figures 4.4c and 4.4d along with Figure 4.4a show the average contributing terms to Equation 4.3 as a function of location. Figure 4.4d shows that the number of soot particles is maximized much closer to the injector nozzle than areas of considerable volume fraction seen in Figure 4.1. The number of particles is inversely related to the extinction efficiency at approximately 5cm away from the injector nozzle where substantial particle growth occurs by coagulation. The extinction efficiency of Figure 4.4c finds its shape as a combination of the patterns seen in Figures 4.4a and 4.4b. Attenuation diameter's influence is found in Eqs. 4.6 and 4.11 via x_p and the strong core is a function of the less compact soot particles that exhibit increased scattering efficiency seen in Equation 4.12. The extinction efficiency also shares a similar shape to the volume fraction.

Coefficient of Extinction

Equation 4.3 is solved over the whole domain by iterating through all of the stochastic soot particles and solving for each particle's contribution. Figure 4.1e shows the resulting surface plot colored by K_e. For comparison,

$$K_e = f_v \frac{6\pi}{\lambda}(1 + \alpha_{sa})E(m_o), \tag{4.14}$$

where $(1 + \alpha_{sa})E(m_o) = 0.46$, is solved using the simulated volume fraction and plotted in Figure 4.1d Note that the right side is simply a scaled soot volume fraction plot and that it makes the same assumptions that the measurement based data of plot 4.1a make.

Figure 4.1e shows that the opacity of soot is not related proportionally to the volume fraction of soot. Specifically, regions of high opacity are expanded to the core and extend

further to the perimeter of the sooty region. Figure 4.1c shows a surface colored by the simulated optical thickness and then correlated to soot volume fraction using the same constant coefficients of Equation 4.10 used in measurement based values. In essence, this is what the simulation expects the measurement based data to look like. Comparing the measurement based data of Figure 4.1a and the expected data based on simulations of Figure 4.1c, the measurement based data exhibit many of the properties expected. Specifically, the core of the jet exhibits high values. The simulated results still deviate from the measurement based results by having sharper wings and high attenuation surrounding the core where the measurement based results have a much softer gradient that monotonically reaches a maximum attenuation at the core. Comparing the magnitudes of Figures 4.1e and 4.1d shows that the measurements are generally under-predicting the simulation based soot despite the volume fraction plots of Figure 4.1a and 4.1b being approximately correct magnitude wise. Possible sources for the remaining error include soot particle motion deviation from the bulk Eulerian fluid motion, inaccurate soot surface chemistry, and unaccounted variability of soot optical properties, such as refractive index, or inaccurate models for scattering efficiency of a highly diverse soot population.

4.6 Conclusion

A soot simulation using a detailed stochastic soot model was used to simulate a Spray A case. The combustion simulation was validated by comparing to the measured liftoff length and convergence studies were used to verify the phenomenological soot model stability. The experimental soot volume fraction, measured using KL extinction and assuming a monodisperse spherical soot population, and simulated soot volume fraction showed substantial differences. The simulated soot volume fraction gradients were sharper and had its region of maximum soot volume fraction away from the axis. Using models for attenuation, absorption, and scattering, the optical extinction coefficient was found for the simulated soot. This

modeled field was compared to the field of extinction coefficient created using the constant soot optical properties assumed in the measurements. The modeled extinction coefficient revealed a profile that matched the measurement based profile much more closely with much more absorption near the axis. Even allowing the possibility of relatively inaccurate soot simulation, these results indicate that local soot particle shape is an important factor in KL extinction measurements for soot volume fraction.

Indirectly related to the optical properties, region cumulative PSDs were found to be constructions of subsets of particles with different histories and different PSDs.

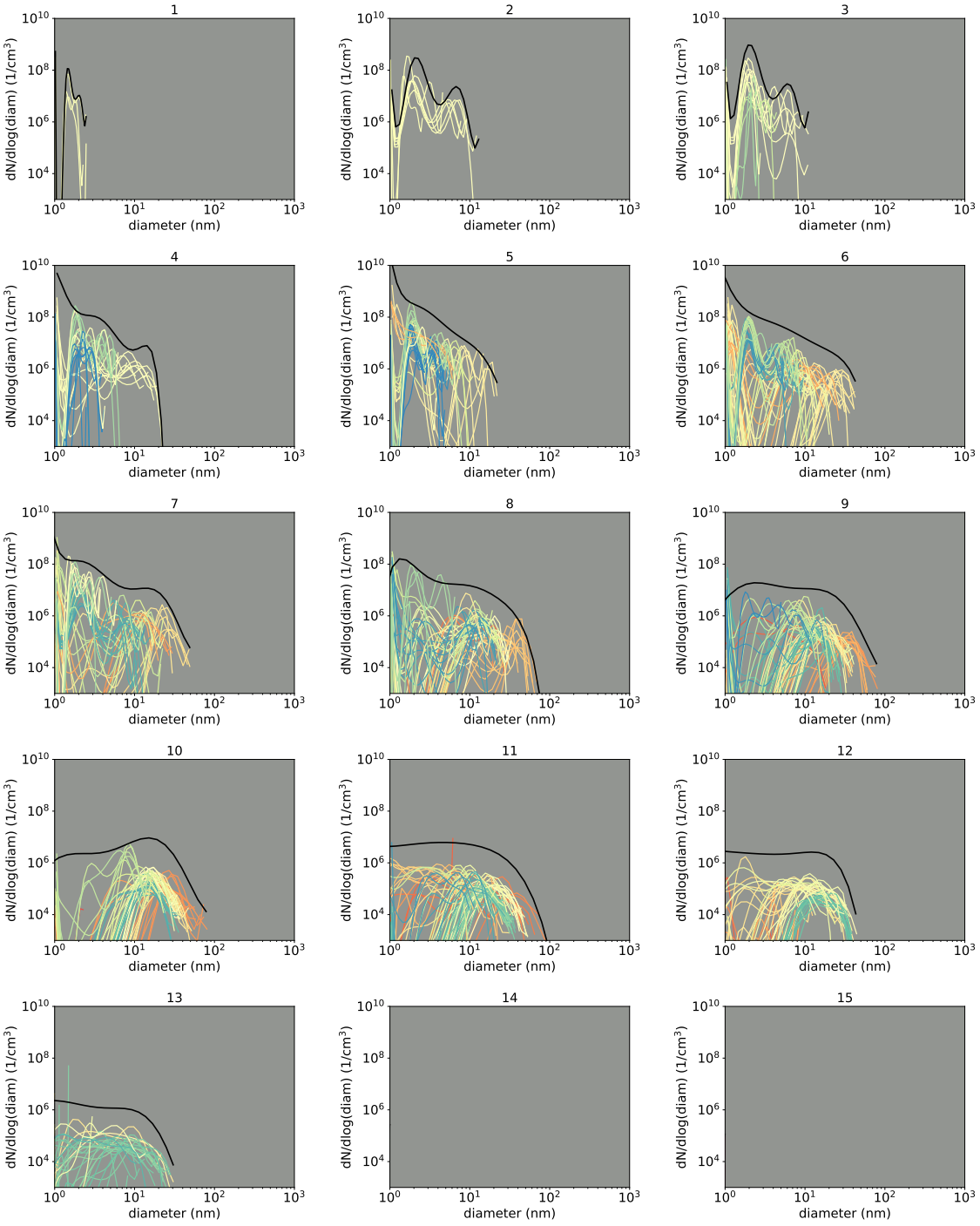

Figure 4.3: PSDs across all soot producing regions of the domain at 5 ms after the start of injection. Each colored curve represents a cell sized region (1cm characteristic length). Each black curve represents the axial section cumulative. Refer to Figure 4.2 for an explanation of location interpretation. Diameter is electrodynamic diameter.

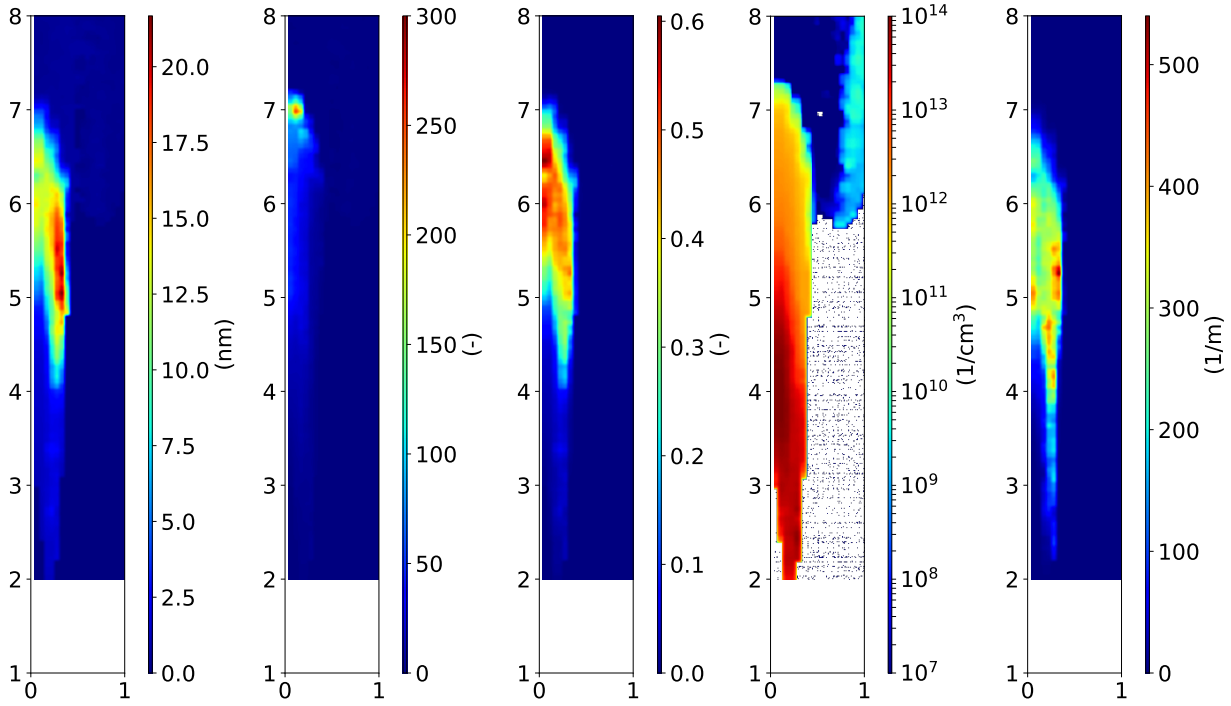

(a) average attenuation radius

(b) average number of primary particles per agglomerate

(c) average extinction efficiency

(d) soot particle concentration

(e) average extinction coefficient calculated using Equation 4.3

Figure 4.4: Surface plots of the time averaged indicated value. Surfaces are bisections of the central axial plane.

5 MODEL APPLICATION: SOOT'S GROWTH VIA HACA

5.1 Motivation

To meet tightening soot regulations, now and in the past, many strategies have been considered. After treatment is a popular and effective option if the correct operating conditions are met but additional components are often relatively expensive. Instead of treating the symptom through after treatment, reducing emissions produced by the combustion cycle is an attractive option. Techniques to reduce engine-out emissions are not obvious and usually a gain in one area is matched by a loss in another. For instance, typically injection timing can be retarded for cooler combustion temperatures and reduced NOx at the cost of increased soot and vice versa. One method aimed at reducing soot without a significant downside is splitting the injection. For example, under heavy load conditions, Tow et al. [122] found injection profiles with 3 injections with a relatively long dwell before the final injection that resulted in a reduction of soot by a factor of two, no NOx penalty, and 1.5 percent BSFC increase. However, Bobba et al. [9] showed soot could also be increased by splitting the injection depending on timing during low temperature combustion cases, but either way the increased mixing was significant in the development of soot. The opportunity of split injections has driven many similar experimental studies, investigating the relationship between injection profile, fuel mass, engine load, etc. and soot. These studies have found split injections affect soot via enhanced mixing, increased temperature, and reduced continuous injection duration [53]. Even with substantial experimental knowledge, because of the number of degrees of freedom, the microscopic nature of soot, and the sensitivity of soot to minor adjustment, a design-level understanding of soot is still out of reach [9]. For such insight, simulation can be used to bridge the gap between theory and experimental results as in the field of turbulence. Han et al. [53] ran simulations with a laminar-and-turbulent characteristic-time combustion model and a modified empirical Hiroyasu model to find that shorter injections

did not maintain areas of high equivalence ratio important to soot production. Many other simulations with empirical models have been used to investigate mostly mixing related phenomenon because it is difficult to draw conclusions about phenomenon such as addition that are not necessarily simulated. Yue et al. [133] studied soot oxidation using constant volume simulations with detailed chemistry and an improved semi-empirical two-step soot model that considered oxidation by O_2 and OH. They determined post injection lead to more soot formation and oxidation and the ultimate benefit of post injections depended on whether there was sufficient time to oxidize the soot developed by the post injection.

Unfortunately, engine soot studies performed so far have been done using relatively simple soot models limiting the potential inferences. For example, Hessel et al. [55] made a relatively exhaustive study with the Hiroyasu soot model in which cylinder averages and isosurfaces of oxidation, formation, temperature, and pertinent species are investigated to find post injections can reduce soot generation by accelerating combustion.

The HACA pathway is commonly credited as the main contributor to soot growth [64, 126]. What follows is a study into the HACA pathway, using the extended hybrid soot model. The additional detail offered by the extended hybrid model, specifically, the ability to calculate soot surface reaction and coagulation rates based on soot particle shape, will provide insight into how crucial the HACA pathway is and what drives it. If the HACA model is responsible for all of the soot growth then coagulation, agglomeration, and other particle collision-based forms of soot growth can be ignored without regret in general soot studies. This is significant in stochastic models such as SWEEP because the data structures built around coagulation are relatively expensive to access. The simulation time can be cut from $\mathcal{O}(N \log(N))$ to $\mathcal{O}(N)$, where N is the number of particles, without assumptions made in the linear process deferment algorithm [94]. It is also an important justification for simpler semi-empirical models that do not consider coagulation such as the multistep and two-step model. If the HACA model is not responsible for soot growth, previous conclusions need

to be reconsidered and additional research into the growth mechanisms of soot and their implementation into soot models is required.

5.2 Acetylene addition investigation

The HACA path was developed by Appel et al. [3] and a more complete description of it can be found in their work, however, a brief description is presented here. The HACA path is a progression of reactions with a soot particle as a reactant or product. Conventional soot growth theory dictates chemical modes of soot growth occur at local surface sites of a soot particle. Reactions involving these sites occur like reactions of large PAH molecules with the gas phase [64]. The HACA model is a progression of such PAH reactions that result in PAH growth (i.e. soot growth). The chemical equations of the HACA model are given in Equations 5.1 through 5.3.

$$A_i + H \longleftrightarrow A_{i-} + H_2 \tag{5.1}$$

$$A_{i-} + C_2H_2 \longleftrightarrow A_{i-}C_2H_2 \tag{5.2}$$

$$A_{i-}C_2H_2 + C_2H_2 \longrightarrow A_{i+1} + H \tag{5.3}$$

where A_i is a soot particle of size i. Equation 5.1 shows hydrogen abstraction works to radicalize aromatic sites on a soot particle. Equation 5.2 is a reversible acetylene addition reaction and. Equation 5.3 stabilizes the larger soot particle with an additional acetylene addition reaction. These equations justify the acronym HACA (hydrogen abstraction C_2H_2 addition).

The previously discussed GM 1.9L simulations with the extended hybrid model used for validation of the combustion and soot model in Section 3.3 are used again here for the investigation because the operating conditions are representative of sooty, low load, cold start conditions. Experimental conditions can be found in Table 3.4.

The following is an investigation of the effects of acetylene addition; it is not an investiga-

tion into more general aspects such as what other processes influence soot or what operating conditions will minimize soot. The first half of the investigation is done through comparison of the SOI9 and SOI23 cases. The conventional case is ignored for clarity and with little loss of information because of its similarity, soot-wise, to the SOI9 case. The second half of the investigation is a deep dive into the pertinent phenomenon of acetylene addition using only the SOI9 case. The SOI9 case is picked over the SOI23 case because of its sensitivity to acetylene addition as shown in the first half of the investigation.

The investigation will start by comparing the effects of acetylene addition on the SOI9 and SOI23 case soot. Simulation, especially with phenomenological models, provides the ability to change physics in a hypothetical world. The effects of acetylene addition on the SOI9 versus SOI23 cases will be investigated by considering both with the validated soot model and the same model with the acetylene addition removed.

Figure 5.1 shows PSDs at the sampled times indicated in Figure 5.2 with and without acetylene addition active. The baseline PSDs at EVO of Figure 5.1 are the same as those compared to measured data in Figure 3.19. The PSD produced with acetylene addition at EVO for the latter case has a similar shape the PSD produced without acetylene addition but with a slight transpose to more and larger particles. The PSD produced with addition for the earlier case is much broader with a less pronounced medium sized particle mode, has significantly more and larger particles, and a different shape in general than the PSD produced without addition. It is clear from these plots that acetylene addition has a much more significant impact on the SOI9 case with respect to the soot at EVO.

Figure 5.2 shows the mass concentration of acetylene over the combustion cycle for the SOI9 and SOI23 cases. Although the SOI9 case has generally higher amounts of acetylene, both cases produce amounts on the same order and local maximums differ by less than a factor of 2. Figure 5.2 also indicates sampling times that will be used in Figure 5.1, Figure 5.3, and Figure 5.7. The first sampled time, 14 deg. ATDC, is at the trailing edge of the

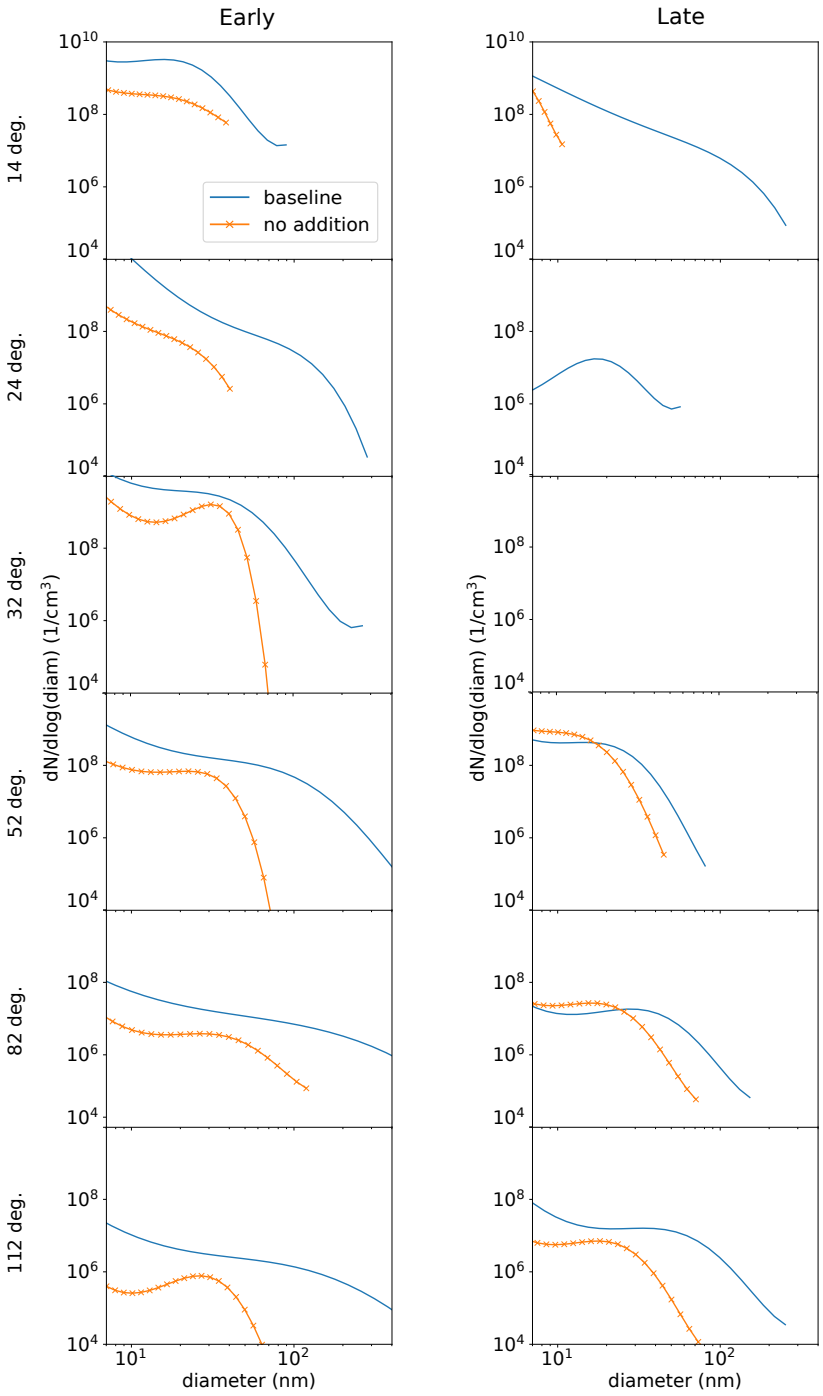

Figure 5.1: PSDs at the indicated crank angle after top dead center for simulations with baseline and no addition in the soot model. The left column is the SOI9 case and the right column is the SOI23 case.

acetylene swell produced by the main, or second, injection for both cases. The next sample, 24 deg. ATDC, is during the dwell of the SOI23 injection case and at the peak of acetylene

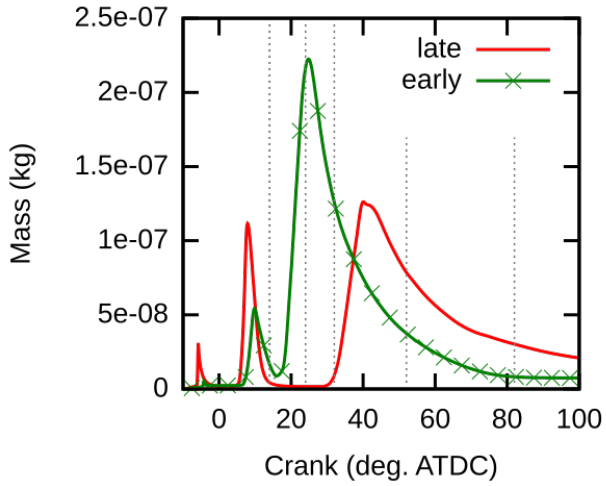

Figure 5.2: Concentration of acetylene during combustion for the SOI23 and SOI9 third injection cases. The doted vertical lines indicate the sampled times that are used in other figures.

produced by the final injection of the earlier case. The next sample, 32 deg. ATDC, is just before the final injection of the SOI23 injection case. The next sample, 52 deg. ATDC, is SOI9 in the trailing edge of both final injection acetylene swells followed by the sample at 82 deg. ATDC. The final sample is at EVO, 112 deg. ATDC, and not shown in Figure 5.2. Considering the timing information of Figure 5.2 provides context to the plots of Figure 5.1. At 14 deg. ATDC the SOI23 case has just experienced higher average concentrations of acetylene and the PSD is highly effected by addition. This is also the only time where the SOI23 case has larger particles than the earlier case. At 24 deg. ATDC the SOI23 case soot is in rapid decline. Without addition the SOI23 case soot is below meaningful concentrations. The SOI9 baseline case continues to grow larger particles however without addition; the PSD looks similar to the PSD at 14 deg. ATDC. At 32 deg. ATDC the SOI23 case soot, with or without considering addition, is below meaningful concentrations. The SOI9 case has swells in medium sized particles and the largest particles are reduced in the baseline case. At 52 deg. ATDC the SOI23 case has just gone through most of the combustion from the SOI23 injection and its PSDs are back. Both the baseline and modified PSDs are strikingly similar. In the SOI9 case, the concentration of all particles below 100nm diminishes

by approximately an order of magnitude while the baseline PSD moves to larger particles. For the remainder of the cycle all profiles experience a similar trend; all concentrations are reduced for particles smaller than 100nm, and baseline PSDs tend to flatten out, generally creating larger particles. During the injector dwell in the SOI23 case, the soot population is destroyed. This is consistent with the minimum injection dwell duration findings of Han et al. [53]. Alternatively, the dwell for the earlier case is much shorter and the soot population is always maintained. The plots representing times after the start of the third injections show that the SOI23 injection soot distribution is much less dependent on acetylene addition. The SOI23 injection PSD shapes are similar but shifted by a small amount. The SOI9 injection PSD without acetylene addition is drastically different with a much less pronounced larger particle mode but with many larger particles. Figure 5.1 shows that the importance of acetylene addition is a function of the engine operating conditions. The investigation will explain why the acetylene addition effects differ.

Figure 5.3 is a variation on the typical PSD plot and requires some explanation. The PSD notation and CDFs are discussed in the appendix, §A.4. If the CDF of a conventional PSD plot is instead the CFD of the total rate of acetylene addition that is occurring to any particles smaller than x, then Figure 5.3 is the plot of log(D(log(x))) vs log(x).

Figure 5.3 shows plots of distribution functions of the rate of acetylene addition events, ordered by the size of particles that the events occur on (abbreviated RDF), at the sampled times of Figure 5.2. Figure 5.3 shows which and how strongly particles are affected by acetylene addition. The RDFs shown in Figure 5.3 are the product of the specific rate as a function of particle size and the number of particles at that size. At 14 deg. ATDC acetylene addition is more prevalent in the SOI9 case over the range of particles that exist. The distribution function has a local maximum that corresponds to the population local maximum shown in Figure 5.1. Alternatively, the SOI23 case has a PSD that monotonically decreases but a RDF with a local maximum nearing its largest particles. At 24 deg. ATDC

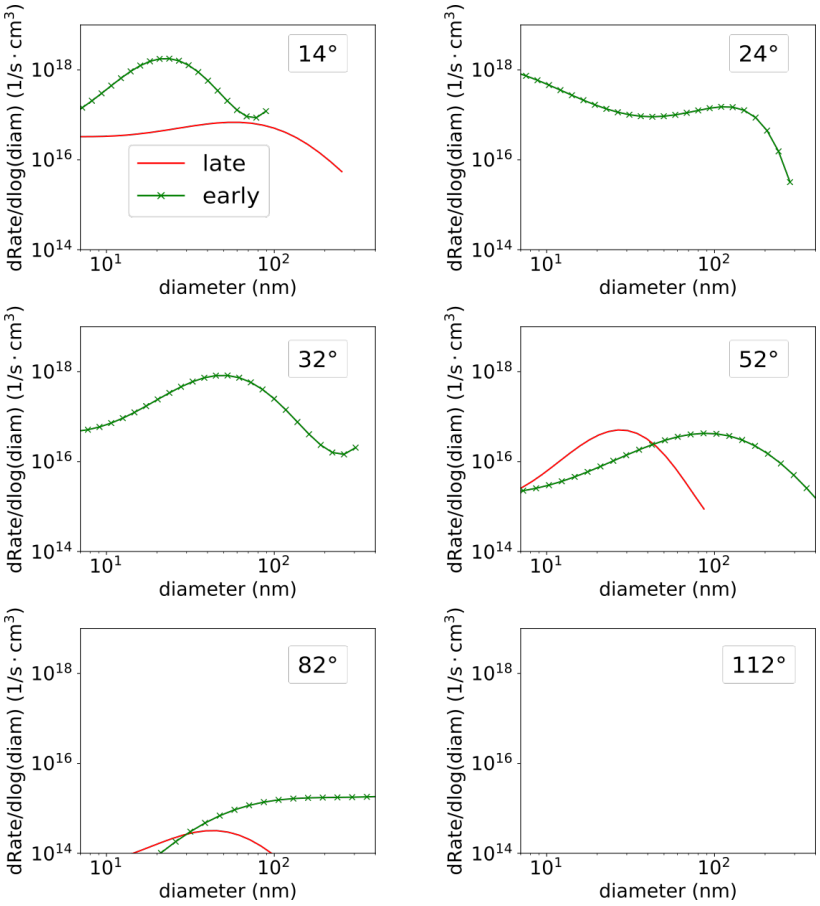

Figure 5.3: Distribution function of rate of C_2H_2 addition events distributed by soot particle size for the indicated crank angle after top dead center.

acetylene addition is not occurring in the SOI23 case. The SOI9 case now sees the behavior that the SOI23 case seen at 14 deg. ATDC, namely the local maximum of the RDF does not correspond to a local maximum of the PSD. At 32 deg. ATDC the SOI23 case is again not affected by addition, but the SOI9 case is. At 52 deg. ATDC both cases are affected by addition at approximately equal rates. The local maximums of RDF correspond to weak modes in their respective PSDs. At 82 deg. ATDC only the larger particles are affected by addition and the SOI9 case is affected more despite having a lower population of affected particles. At 112 deg. ATDC both cases are unaffected by addition.

Notice that the acetylene addition rate magnitudes decline throughout the combustion duration. The plots at 24 and 32 deg. indicate that during the dwell of the SOI23 injection

case that decimates the soot formed from the main injection, there is no soot for the acetylene to react with. Meanwhile, the soot population of the SOI9 injection case is maintained and is heavily acted on by acetylene addition. For the latter case, after the timing of the third injection, the decline of acetylene addition importance is rapid.

It has been shown that the SOI9 case is more sensitive to acetylene addition than the SOI23 case with respect to the PSD at EVO. It has also been shown that this is at least partially due to injection timing and not other factors such as exceptional local equivalence ratios, for instance. The remainder of the investigation will focus on what factors drive acetylene addition seen in the SOI9 case.

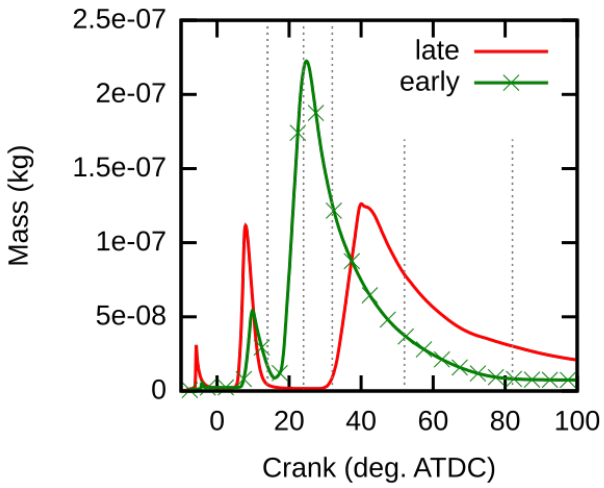

Figure 5.4: Cylinder averaged acetylene addition using the baseline, constant $\alpha = 0.01$, and reduced temperature models.

The detailed stochastic model calculates the acetylene addition rate using the Arrhenius submodel rate Equation 2.5. Figure 5.4 shows that the cylinder averaged acetylene addition rate as produced by the baseline validated model and two model alterations.

Because of the multiplicative nature of Equation 2.5, the term that spans the most decades will be the most influential. Decade is defined here as

$$\text{number of decades} = \log(x_1) - \log(x_2) = \log\frac{x_1}{x_2}. \tag{5.4}$$

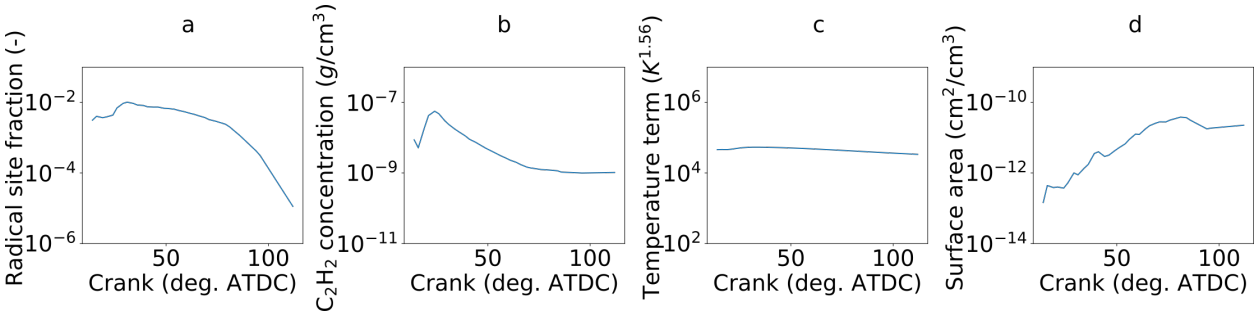

Figure 5.5: Cylinder averaged terms of Equation 2.5. All plot ranges span the same number of decades.

The plots of Figure 5.5 show the cylinder averaged terms of the right-hand side of Equation 2.5. Namely, radical site fraction, acetylene concentration, soot surface area, and soot particle temperature. All plots span the same range highlighting the effect that the term would have on addition. The addition rate for the baseline case in Figure 5.4 is relatively constant until 80° ATDC when it plummets 6 decades. The shape and scale of the addition plot roughly matches the shape of the radical fraction plot, indicating the radical fraction drives changes in addition over time. Acetylene concentration also shows a decline but its shape would indicate that the addition rate should have slowed much earlier than it did. The average surface area, which has a positive trend, does not correlate with the additions negative trend. The temperature term only spans $\mathcal{O}(0.1)$ decades. This disparity in the terms of Equation 2.5 indicates temperature does not directly drive the propensity for acetylene addition.

To confirm that temperature has little direct effect on the soot production, the simulated physics were changed again. This time, the soot simulation was run with temperatures reduced by 10 percent over the entire domain and throughout the entire simulation. Figure 5.4 shows that the addition rate changes by less than an order of magnitude and Figure 5.6 shows the corresponding change in the PSD at EVO for the modified simulation is practically identical to the standard simulation.

The physics are changed again to set $\alpha = 0.01$. Now, Figure 5.4 shows a considerable increase in the addition rate and Figure 5.6 shows a significant increase in the largest particles.

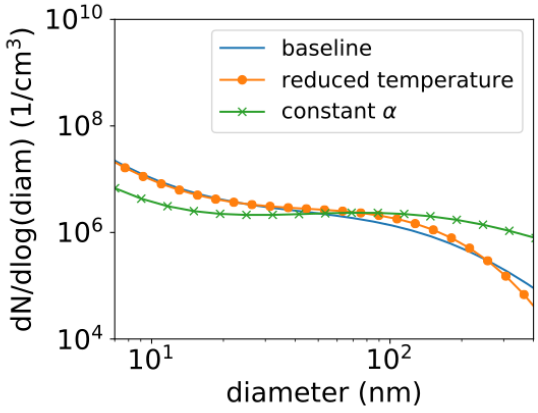

Figure 5.6: PSDs at EVO for SOI9 case with the temperature term in Arrhenius rate equation for acetylene addition reduced by 10 percent.

The addition rate created with a constant radical site fraction varies more before 80° ATDC and also drops in frequency after 80° ATDC but by less than 2 decades, spanning slightly more than 3 decades in total. Although the addition rate experiences some slowdown, it is clear that radical site fraction is the main contribution to the substantial slowdown seen in Figure 5.4.

Global averages help to explain trends over large durations of the combustion cycle however most soot is produced in local abnormal regions of exceptional composure. To investigate the importance of terms in Equation 2.5 at any instant in these small subdomains, the domain must be examined with spatial resolution. To do so, colored surfaces of the domain are created by collapsing the azimuthal dimension of the simulation to a single plane, then interpolating soot parcel values to a uniform grid. This method loses azimuthal dependence information, but it allows more resolution in the radial and z directions.

Figure 5.7 has surfaces for the SOI9 case colored by the rate of acetylene addition and temperature. Lagrangian parcels are queried for their attribues and a surface is made by bilinear interpolation along a uniform mesh. The azimuthal coordinate is collapsed to make the 2D surfaces. Data from parcels was not extrapolated so regions beyond parcels are left blank, as seen in the upper right-hand corner of the head and wall. These areas without

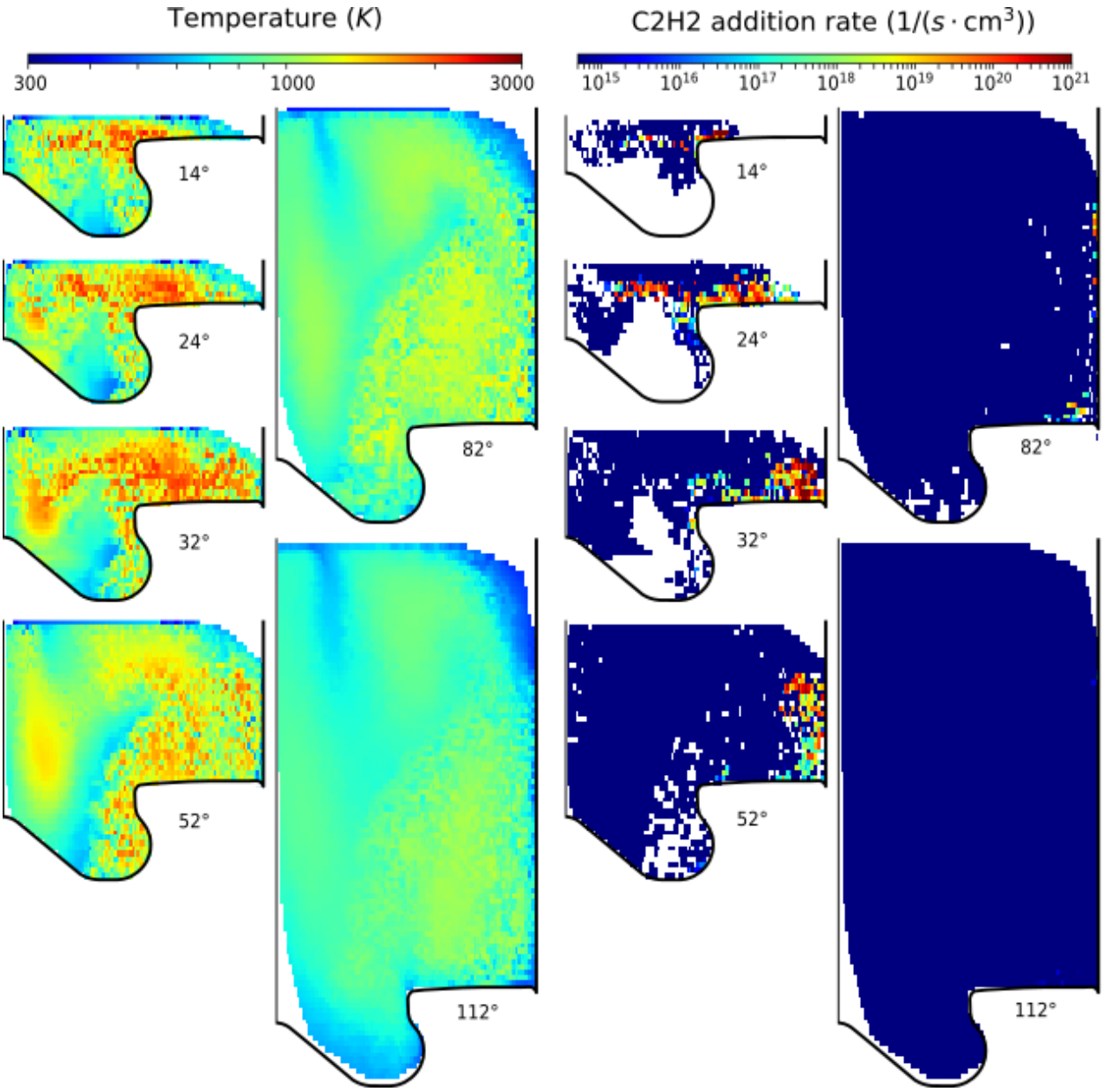

Figure 5.7: Surfaces colored by soot parcel temperature and C_2H_2 addition rate according to the scale at the top of the figure. White areas indicate a lack of data.

parcel representation did not have a high enough pyrene concentration to initialize a parcel, nor was there advection of parcels into them. Interpreting the model, there would not be soot there. Blank spots within the parcel cloud seen in the acetylene plots that are not blank in the temperature plots are areas in which acetylene addition has gone below the lower bound of the scale. A lower bound was installed so that interesting features were more visible and

because acetylene addition below the rate of $\mathcal{O}(1e14)$ is effectively inconsequential for the cases studied. Note that the same lower bound was used in Figure 5.3. At 14 deg. ATDC the injection structure is clearly visible in the temperature and addition rate surfaces. At 24 deg. ATDC the injection flow structure has started to disappear in the temperature surface as general volumetric temperature increase begins but it persists in the addition rate. At 32 deg. ATDC high temperatures are found in near the center of the cylinder; however, areas of high addition continue to only be at the head of the injection flow structure. At 52 deg. ATDC the areas of high temperature and addition share little in common. Significant addition continues to retreat toward the cylinder wall. At 82 deg. ATDC the last bastions of significant addition are found directly next to the cylinder wall meanwhile heat transfer has started to cool gasses directly next to the wall. At EVO no significant addition is observed as predicted by the plot of Figure 5.3. It is obvious from the figures that temperature is at least not the only controlling factor in acetylene addition. There seems to be very little relation between areas of high temperature and areas of high addition. Figure 5.7 shows that being closer to the wall has more impact on acetylene addition than temperature although it is certainly an indirect effect. To find the important terms of Equation 2.5, the relation between the terms and addition must be quantified. A measure of relation is Pearson correlation

$$\text{correlation}_{X,Y} = \frac{\text{cov}(X,Y)}{\text{Std. dev.}(X)\,\text{Std. dev.}(Y)}, \tag{5.5}$$

where cov is the covariance given by

$$\text{cov}(X,Y) = \text{Ex}[(X - \text{mean}(X))(Y - \text{mean}(Y))], \tag{5.6}$$

where Ex is the expectation.

Figure 5.8 shows the correlation between the acetylene addition rate and the indicated value over the cycle. As expected, temperature is only slightly correlated, and the correlation becomes worse with the cycle progression. Interestingly, the radical site fraction is not well

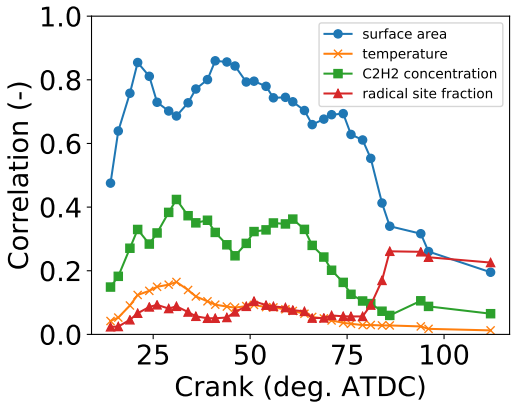

Figure 5.8: Pearson correlation between the indicated and acetylene addition rate surfaces.

correlated until SOI23 in the cycle despite our findings that it was responsible slowing the addition rate. To explain this, it is necessary to view the results with respect to time. Early in the cycle when the average radical site fraction is relatively constant, the correlation is low but as the radical site fraction plummets, the correlation becomes stronger indicating the radical site fraction is responsible for ending addition but not regulating addition when it is occurring. Surface area is highly correlated to addition indicating surface area is the main throttling process of addition. It is worth noting that there is a direct positive feedback loop for surface area and a negative feedback loop for acetylene concentration. Acetylene addition consumes acetylene and grows soot. Although this affects the dynamics of addition, it does not change the effect of the terms in Equation 2.5. In other words, even with feedback, the correlation between the terms and addition is still a measure of addition's dependence on the terms. The findings of the correlation study are consistent with acetylene addition having a stronger effect on the SOI9 case than the SOI23 case. Once initialized, the SOI9 case keeps a soot population with significant surface area throughout the combustion process, allowing acetylene addition to continue impacting soot. The latter case allows all of the soot created by the main injection oxidize away, leaving only the soot from the third injection to survive until EVO. The third injection effects of the SOI23 case occur relatively shortly before the

radical site fraction slows addition to inconsequential values.

5.3 Conclusion

The GM1.9L engine simulations with the extended hybrid model allowed an in depth analysis of the acetylene addition soot production pathway that is not possible using any other commercial soot model. Acetylene addition had a much larger impact on the SOI9 and conventional case than the SOI23 case. The cause was investigated while considering temporal and spatial resolution of the soot processes. The SOI9 case kept a soot population throughout the combustion process, allowing acetylene addition to continue impacting the population. The SOI23 case oxidized all of the soot created in the first and second injection, leaving only the soot from the third injection to survive until EVO. The soot generated by the third injection was only subjected to much slower acetylene addition SOI23 in the cycle. The acetylene addition rates were slowed by reduced radicalization of active surface sites required for surface reactions such as addition. It is clear that while acetylene addition is important in soot production, it is not the only mode of growth. Accurate soot models cannot be simplified by removing or only considering acetylene addition. The heavy reliance of this model, and others, on a derivative of the HACA model to determine the crucial radicalized active surface area lights a path towards more accurate models by refinement of the radicalized active surface fraction submodel.

6 MODEL APPLICATION: SYNGAS'S INFLUENCE ON SOOT

6.1 Motivation

In recent years, a substantial amount of attention has been devoted to dual-fuel combustion strategies [26, 51, 58]. These strategies have shown the potential to achieve high efficiency while keeping engine out emissions low. Dual-fuel strategies can be divided into two categories depending on the timing of the fuel injection event [131]. When the injection timing is early in the cycle, chemical kinetics controls combustion phasing and duration. Without direct control over the combustion process, practical application of early injection timing strategies can be challenging [70]. For injection timings late in the cycle (i.e., near top dead center), the combustion event becomes directly coupled to the fuel injection event and combustion phasing control is no longer a challenge. Due to the ease of operation in this regime, a substantial portion of dual-fuel research has been focused on diesel substitution strategies where near top dead center injection timings are used and diesel is partially replaced by a premixed gaseous fuel. Most dual-fuel strategies have consistently shown increased efficiencies through a shorter, more thermodynamically favorable combustion event, and a reduction of the mixing requirements of the direct injected fuel. However, the use of two fuels presents challenges for many applications; such as the requirement of having two fuel reservoirs and asymmetric consumption of the fuels leading to different filling intervals. An alternative approach that enables true single fuel operation is achieved through fuel reformation [20–22]. The concept involves the use of an on-board reformer to generate syngas. Syngas is a mixture of hydrogen, carbon monoxide and inert species such as water and carbon dioxide. The syngas can be used as a secondary fuel in the engine, enabling the advantages of dual-fuel operation from a single fuel stream.

Previous work by the Chuahy et al. [21] has shown that the addition of syngas can significantly reduce the particulate emissions, when expressed by filter smoke number (FSN).

Kittelson et al. [69] has shown that emitted particles can have different health impacts depending on their size, where smaller particles have a higher rate of deposition in the human lung, thus having a higher impact when respiratory issues are concerned. Additionally, work by Zhang et al. [136] has shown that different combustion strategies may have significantly different PSDs for similar FSN measurements, highlighting the importance of PSD measurements on evaluating possible health impacts of a certain fuel combination and combustion strategy. Finally, with atomic hydrogen being an integral part of the HACA mechanism (section 5.2) it is of interest to study the effects of reformed fuel on the PSD behavior of DPI and RCCI strategies and how the presence of reformed fuel affects the relative rates of inception, coagulation and addition during the soot formation process. Accordingly, engine experiments using a SMPS and CPC to obtain the PSD for each operating mode will be used to evaluate the effects of syngas substitution and composition on the particulate sizes for DPI combustion. These effects will be analyzed using detailed stochastic soot simulations (e.g., [70]), providing a more complete description of the soot population, including PSD results for direct comparison to measured data.

Experimental methods

Experiments and measurement postprocessing was performed by Chuahy [18], simulations were run by the author, and conclusions were a cumulative effort.

Engine specifications

The engine used was a single cylinder version of a Caterpillar C-15, 15-L six-cylinder engine. Table 6.1 shows the engine specifications. The C-15 is typical of a heavy-duty size-class diesel engine with a bore of 137-mm and a stroke of 171-mm yielding a displacement of 2.5 liters per cylinder. A turbocharger was simulated by pressurizing a closely coupled intake surge tank with compressed air. A port-fuel injection system was installed to provide the premixed fuel. Experiments were conducted with a commercial US #2 diesel fuel (supplied by Landmark

Table 6.1: C15 engine conditions

bore (cm)	13.7
stroke (cm)	17.1
speed (rpm)	1300
CR	16.9
Nominal IMEP (bar)	7.0
Rail Pressure (kPa)	105,120,145
swirl ratio	0.7
injector	6 x 205μm
SOI timing (CA deg. ATDC)	-10 (DPI) -55 (RCCI)

Services Cooperative), with a cetane number of 42, H/C ratio of 1.792 and lower heating value of 42.5 MJ/kg. Syngas was represented by a mixture of 50/50 H_2/CO, unless otherwise specified.

Soot measurement methodology

The particulate sampling system is composed of a heated probe, a two-stage dilution system, a SMPS and a CPC. An exhaust sample is extracted from the exhaust stream and sent through the two-stage dilution system. The sample is diluted once at high temperature and subsequently undergoes a room temperature secondary dilution. The exhaust dilution is necessary to achieve the appropriate sample conditions for the SMPS used to measure the particulate size distributions. The flow rates of the primary dilution air, the secondary dilution air and the heated probe temperature are controlled and monitored by the Dekati Fine Particle Sampler 1.3 software. The SMPS system consists of a long differential mobility analyzer (DMA, TSI model 3081) controlled by an electrostatic classifier (ESC, TSI model 3080). The SMPS system has the capability of resolving particle mobility diameters from 7 nm to 300 nm. The primary dilution air was heated to 400C to prevent condensation of volatile particles. Secondary dilution is performed with air at ambient temperature. The dilution ratio is chosen to provide the CPC with an adequate number of particles for the measurement. Too few particles can reduce the repeatability of the measurement while too

many may saturate the analyzer and result in particles being missed. The overall dilution ratio is controlled by selecting solenoid valve combinations inside the control unit. An overall dilution ratio of approximately 60:1 was chosen as a suitable number based on previous works [136]. To determine the dilution ratio, the diluted sample is measured with a Fourier transform infrared (FTIR) spectrometer (Nicolet Model CQ1319-100). For each operating condition, seven PSD scans were performed. Each scan consists of a scan-up of 155 s and scan-down time of 30 s. The results of the seven scans are averaged and corrected for the measured dilution ratio for all reported PSDs.

6.2 Simulation methods

The same chemistry mechanism developed by Ren at al. [101], described in section 3.1, and used in validation was used, again, here.

O-D reaction modeling

0-D, constant volume, homogeneous, simulations were run using the SENKIN detailed chemistry, constant volume code [82]. SENKIN is a homogeneous time evolution solver with detailed chemistry and sensitivity analysis capabilities. The detailed chemistry equations and thermodynamic data are compiled by CHEMKIN [27] and the variable order numerical solution methods of DASAC [13] are used to solve the formed nonlinear differential equations. SENKIN has been fully, 2-way, coupled with SWEEP on the chemistry timestep.

Multi-dimensional computational fluid dynamics modeling

The C15 engine was simulated using the same 3D engine simulation program and parameters described in section 3.3 and used for in the validation step with Spray A. The mesh was changed to a 60° sector mesh made up of 45,000 cells. The mesh size was selected by per-

forming a grid sensitivity study. It was found that this grid size gave an acceptable trade-off between accuracy and computational expense.

6.3 Results

Measured

Constant premixed equivalence ratio

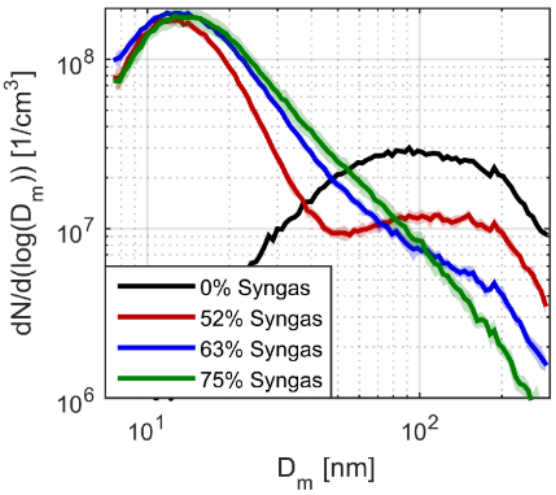

Figure 6.1: PSD curves for constant premixed equivalence ratio experiments

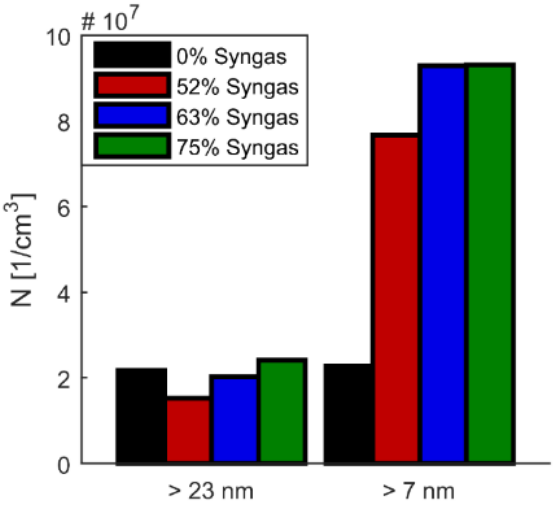

Figure 6.2: Integrated particle number density for constant premixed equivalence ratio experiments

The first set of experiments involved the substitution of diesel fuel for syngas at a constant premixed equivalence ratio. Table 6.1 shows a summary of the operating conditions. The intake pressure was adjusted to prevent over-leaning of the premixed fuel as diesel fuel is replaced by syngas and maintain a constant premixed fuel equivalence ratio. The injection pressure of the direct-injected (DI) diesel fuel was held constant at 600 bar and the start of injection (SOI) timing was fixed at -10 deg. ATDC. Figure 6.1 shows a comparison of the PSDs for the experiments. The addition of syngas has a significant impact in the concentration of all particle sizes. The addition of 52 percent syngas by energy resulted in a factor of two reduction in the concentration of particles larger than 40 nm. Conversely, the

concentration of particles sized 20 nm and lower showed a two order of magnitude increase, which indicates the effects of syngas in the PSD, is beyond that of dilution. In previous work by the authors [21], soot reductions were discussed in the context of the Hiroyasu soot model, which does not explicitly account for particulate morphology effects. It is clear that the reductions in soot seen both in [21] and in the current work are driven by a reduction in the mixing requirements of the DI fuel and DI fuel quantity as demonstrated by the Hiroyasu soot model. However, the effects of syngas on the soot chemistry may be playing a role as evidenced by previous works [25, 50, 119, 120, 129] and the substantial changes in the particulate size distribution. As the syngas energy percentage was further increased, further reduction of accumulation-mode particles observed. For the highest syngas percentage tested, the concentration of 300 nm particles was reduced by over an order of magnitude. In contrast, as the syngas percentage was varied from 52 percent to 75 percent, a substantial increase in the concentration of particles smaller than 100 nm was observed. Figure 6.2 shows the integrated number concentration of particles for two measurement ranges. The first range covered the entire particle size domain of the SMPS (i.e., 7-300 nm), the second range was restricted to particles larger than 23 nm, the cut-off diameter for current European Union particle number emission regulations. The total particle concentration for the diesel baseline is approximately the same for both ranges. The addition of 52 percent syngas resulted in a reduction of the total particle concentration when only considering regulated particles. However, when considering the entire particle spectrum, total particle concentration increased by a factor of four. This is the result of the syngas effects on the PSD. Addition of syngas results in a significant increase in particles sized 20 nm and lower. As syngas was further increased, a monotonic increase in total particle concentration was observed for both particle ranges. It is of note that for the 75 percent syngas case, although the PSD was significantly different than the diesel baseline, for regulated particles, the total particle concentration was approximately the same. Conversely, if particles smaller than 20 nm are considered, the

addition of syngas resulted in a factor of five increase in the total particle concentration. It should be noted that accurate measurement of particles below 20 nm in diameter is difficult and carries a significant amount of uncertainty.

Constant intake pressure

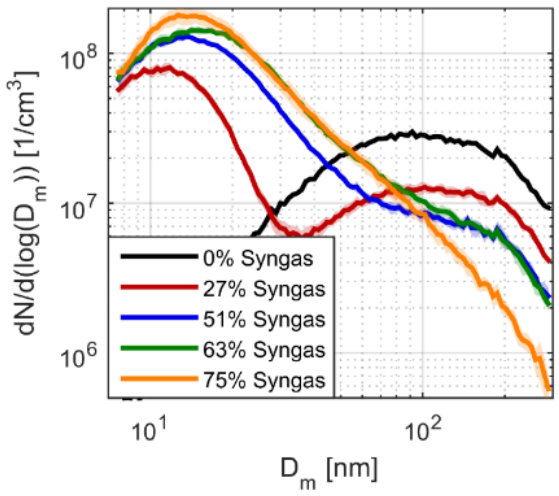

Figure 6.3: PSD curves for constant intake pressure experiments

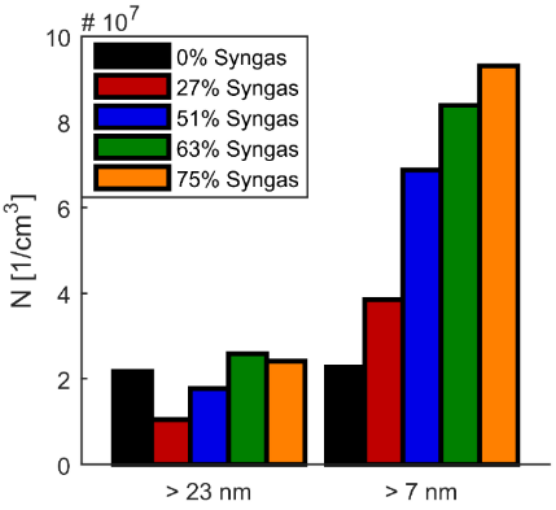

Figure 6.4: Integrated particle number density for constant intake pressure experiments

Additional experiments were performed at constant intake pressure and are shown in Figure 6.3. Similar results are observed for the syngas substitution sweep. At constant intake pressure, over-leaning of the background fuel resulted in poor combustion efficiencies (i.e., the premixed fuel partially burned). Due to the extremely low combustion efficiencies (<80 percent), the cases at constant intake pressure are not typically useful from an engine operation point of view. However, in contrast to the first set of results, where the premixed equivalence ratio was sufficiently high for all syngas percentages, the results of the second set of experiments indicate that the reduction in the quantity of diesel fuel combined with the jet-entrained syngas are mostly responsible for the effects that resulted in the current observed PSDs. Additionally, it is of note that the reductions in intake pressure in the first set of experiments and resulting lower oxygen availability in the spray region were not suf-

ficient to negate the reductions in soot emissions by syngas addition. Although not shown, FSN decreased monotonically as syngas was increased. This reduction correlates well with the reductions in the accumulation-mode particle concentrations for all the cases. It further confirms that FSN alone is not able to capture increases in the concentration of particles smaller than approximately 50 nm.

Syngas composition

A number of studies, [25, 50, 119, 120, 129], have shown that H_2 addition to flames has a soot reduction effect beyond that of dilution. The significant increase in nucleation-mode particle concentrations seen in the DPI experiments indicates that the effects seen in flame experiments are also present in the engine. In order to further investigate the impact of H_2 on the observed PSD curves, the DPI case with 63 percent syngas and 120 kPa intake pressure was used as the baseline and the ratio of H_2/(H_2+CO) was modified while keeping the total syngas energy fraction constant. The H_2/(H_2+CO) ratio was reduced from its original value of 50 percent, to 25 percent and 15 percent.

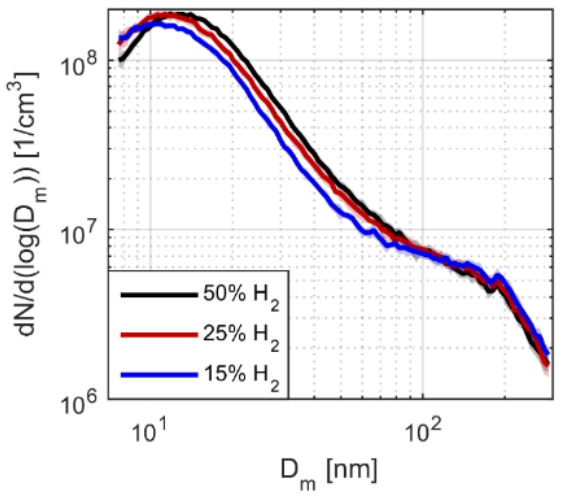

Figure 6.5: PSD curves for constant intake pressure experiments

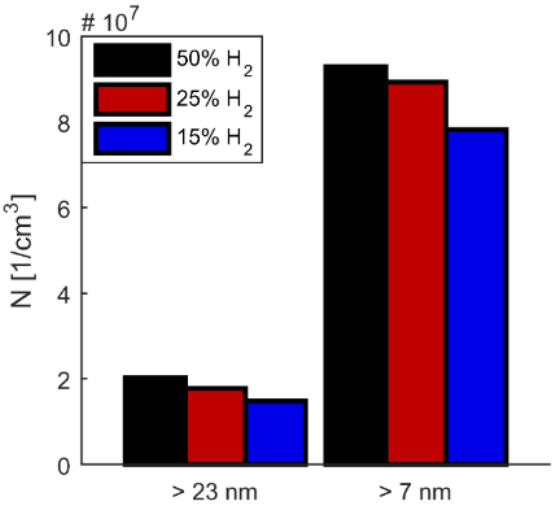

Figure 6.6: Integrated particle number density for constant intake pressure experiments

Figure 6.5 shows the PSD and total particle concentration results for the H_2/(H_2+CO)

ratio sweep experiments. A reduction from 50 percent H_2 by mole to 15 percent H_2 had a minor impact on the PSD curves. As H_2 was reduced, a small reduction in the concentration of particles smaller than 100 nm was seen as a result. Figure 6.6 shows that total particle concentration was slightly reduced for both particle diameter ranges as H_2 concentration was reduced. As H_2 is replaced by CO in the syngas mixture, more air is displaced due to the lower energy density of the syngas mixture. Consequently, oxygen availability in the spray might be playing a role in increasing accumulation-mode particles as H_2 percent was decreased. However, the overall shape of the PSD was not affected. This is thought to be the result of two factors. First, the main effect driving the decrease in accumulation-mode particles is the substitution of diesel fuel for syngas, and therefore changes in the $H_2/(H_2+CO)$ ratio have a minor effect on the shape of the PSD. Second, hydrogen plays a key role in the production of intermediary and small particles seen across all syngas experiments presented and the limits of its influence were not reached. The relative contributions of each phenomenon will be explored in the modeling section.

Fueling strategy

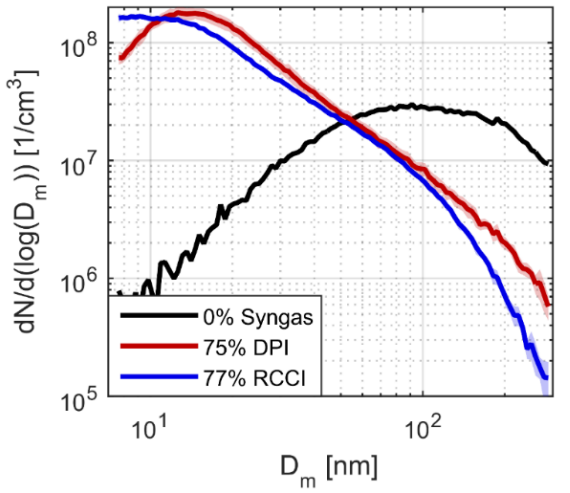

Figure 6.7: PSD curves for diesel baseline, 75 percent syngas DPI case and 77 percent syngas RCCI case

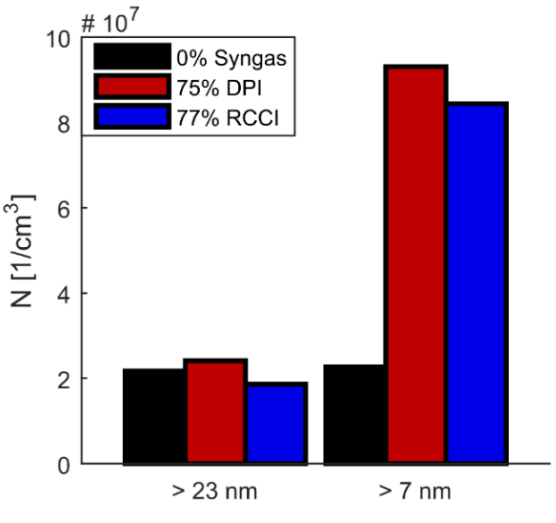

Figure 6.8: Integrated particle number density for diesel baseline, 75 percent syngas DPI case and 77 percent syngas RCCI case

To compare DPI and RCCI operation, the diesel fuel injection timing for a syngas percentage of 75 percent was adjusted to -55 deg. ATDC and the PSD results were compared to the DPI case at the same substitution. Figure 6.7 shows the PSD comparison between the three modes of combustion in the current experiments. The diesel baseline is compared to the 75 percent syngas DPI case and the 77 percent syngas RCCI case. As was already shown, the shape of the PSD is changed significantly once syngas is added to the combustion process. The overall features of the PSD for DPI and RCCI are similar with some distinct differences. For a similar syngas energy percentage, operation under RCCI conditions was able to further reduce accumulation-mode particle concentrations. Further, particle concentrations were consistently lower for RCCI when compared to DPI across the whole diameter range. This is believed to be a result of two factors. First, reduced fuel stratification during RCCI operation, and consequently lower local equivalence ratios, promotes a reduction in particulate formation. Second, the lower local equivalence ratios lead to lower peak flame temperatures, which also slows down surface reaction kinetics necessary for particulate growth. Figure 6.8 shows the total particle concentrations for the three cases. For the regulated particle range, total particle concentrations were similar between the three strategies, with RCCI resulting in the lowest total concentration. RCCIs total particle concentration remained lower than DPIs. As was expected from the reduction in accumulation-mode particles, RCCI resulted in significantly lower FSN than either diesel combustion or DPI combustion. Diesel combustion resulted in an FSN of 1.46, while DPI and RCCI resulted in FSNs of 0.35 and 0.072, respectively.

Simulation and analysis

The results presented in the previous section have shown that the addition of syngas to the combustion process results in significant changes to the PSD shapes and magnitudes. Simulations are used to explain the trends observed in the experiments. Specifically, simulations

of the neat diesel and 52 percent syngas fuel mixture at constant premixed equivalence ratio provide a foundation for comparison and investigation. These two cases were chosen because they show very different soot behavior due to changes in fueling strategy while maintaining a second accumulation mode population as seen in Figure 6.1. This second mode is a useful identifiable feature in making comparisons.

Fully inclusive simulation and validation

To validate the models used, measured experimental data is compared to results of comprehensive 3D simulations. This approach confirms that the models and submodels are predicting the correct behavior when all soot related phenomenon are considered. Once the models have been validated, an analysis of the phenomenon responsible for changes in soot is performed by isolating said phenomenon. The two phenomenon considered are soot chemistry and mixing.

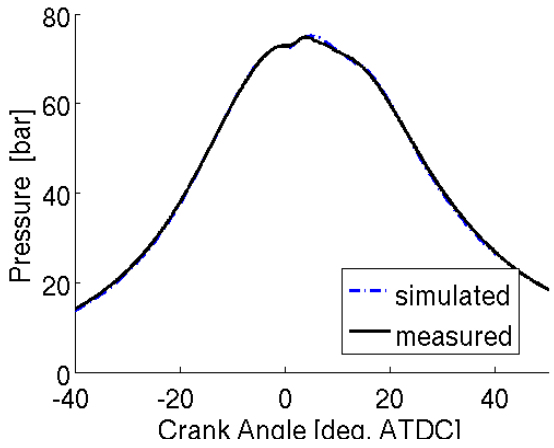

Figure 6.9: Pressure profile for neat diesel

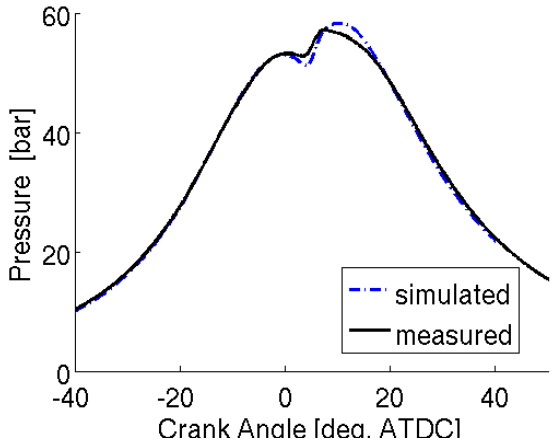

Figure 6.10: Pressure profile for diesel-syngas mix case

The combustion simulation has been generally validated in section 3.3 however validation specific to the current cases will be included here. The combustion simulation of the two investigated cases is validated by comparing pressure profiles to experimental measurements. Figure 6.9 and 6.10 show simulated and experimental pressure profiles that match to within

5 percent. The mixed syngas case deviates more, but the experimental data also has more cycle-to-cycle variability. The agreement found here is similar to other studies (e.g., [60]) and is deemed acceptable for the present study.

Validation of the soot model in section 3 will be supplemented by only the directly applicable and unique measured data covered here. In this work, soot data is catalogued using PSD plots.

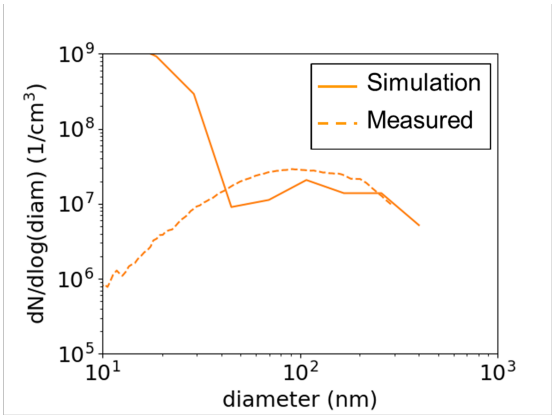

Figure 6.11: Neat diesel PSDs for simulated data at EVO and measured data

Measured data is limited to particles from 7 to 300nm in diameter, but the simulated results are able to capture all sizes. Also, as described earlier, measured data is based on time averaged exhaust readings, meaning PSD results are based on the entire cylinder volume. For comparisons' sake, the simulated results have been limited to 600 nm in diameter and include the entire cylinder volume when comparisons to measured data are made. Figure 6.11 shows a comparison between the simulated and measured particle size distributions for the neat diesel case. The simulated PSDs were generated at exhaust valve opening. The simulation predicts all particles larger than 20nm to within an order of magnitude and the large accumulation mode shape is also captured.

Figure 6.12 shows the simulated particle size distributions for the neat and mixed cases. Trends can be compared to their experimental analogues found in Figure 6.1. Notice the simulations captured the larger accumulation mode and smaller inception sized population

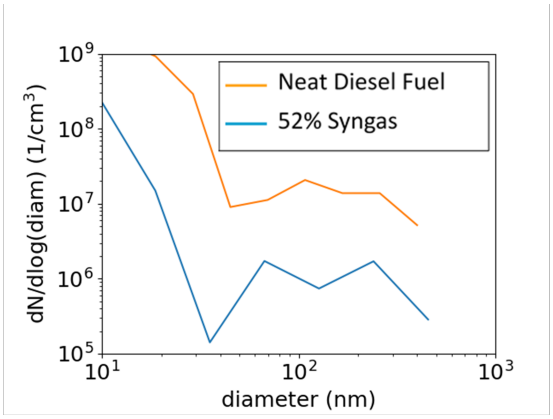

Figure 6.12: Simulated PSDs at EVO for neat diesel and syngas mix cases

for the neat diesel case. For the mixed syngas case, the large inception mode with a smaller and distinct accumulation mode trends are predicted well and to within an order of magnitude throughout the size domain excepting particles around 50nm, where the decrease in population is over predicted.

From the preceding results, it is apparent that the soot production and growth phenomenon are being captured to a reasonable degree, quantitatively as well as qualitatively. The one major exception is with the inception mode population of the neat diesel case. One possible explanation for this difference is that the simulated results are from the time of exhaust valve opening while the measured data is based on a volume that has been transported and prepared for measurement. This gives the small particles time to agglomerate or diffuse to the containment walls. In the following sections, no quantitative conclusions will be drawn based on the inception mode particles. Although there is also a qualitative hump that is present only in the simulated data, it remains relatively small in comparison to the mixed syngas case inception mode. Consequently, for this analysis, the engine and soot models are considered valid.

The following is a dissection of the models and supplementary simulation to gain insight on the influence of syngas on the captured phenomena. The phenomenon impacting soot by adding syngas fit into two categories, soot chemistry or mixing. In the first category, syngas

chemically reacts with soot to modulate its growth. There is a strong case for expecting the components of syngas, specifically hydrogen, to react chemically with the soot surface to inhibit its growth. In the mixing category, changes to soot are due to physical effects of adding syngas. Adding a premixed fuel to a combustion event that would otherwise be based completely on an injection event, naturally has strong ties to fuel stratification. Fuel stratification can influence soot formation by resulting in more or fewer fuel rich regions, whose role in soot formation has been thoroughly investigated.

Soot chemistry simulation

The soot chemistry effects are considered first. Specifically HACA and its effect on particle size. Referencing appendix 5.2, Equation 5.1 shows hydrogen works to deradicalize aromatic sites on a soot particle. Without radical sites, the soot particle cannot go through the addition reactions of Equations 5.2 and 5.3 to become larger. So, additional hydrogen concentration should slow the growth of soot. An expression for the rate of particle growth (i.e., rate from the reactants of Equation 5.1 to the products of Equation 5.3) can be formulated from Equations 5.1-5.3 to make Equation 6.1 if one assumes all chemical reactions are in pseudo-equilibrium [15]

$$\frac{d[A_{i+1}]}{dt} = \frac{K_4 \frac{[H]}{[H_2]}}{(1/(K_5 k_6 [C_2H_2]^2) + 1/(k_5[C_2H_2]) + 1/(k_{-4}[H_2])}, \tag{6.1}$$

where $K_4 = 1$ [3], $K_5 = 1$ [127], $k_6 = 5.27e8$ [127], $k_5 = 1.5e11$ [127], $k_{-4} = 3.713e9$ [3]. Reaction rate constants were calculated at 700 K. This expression shows that there is an exponential relation between hydrogen concentration and soot growth. This can lead to a state of hydrogen "saturation" in which additional hydrogen will have a negative, but negligible effect. If the domain is saturated with hydrogen, adding additional syngas would have negligible soot chemistry effects. The soot chemistry effects are isolated from mixing effects by using homogeneous, adiabatic, constant volume simulations at engine relevant conditions.

Table 6.2: C15 0D simulation parameters

	Neat diesel	Syngas mix
Syngas energy fraction	0	52
Equivalence ratio (-)	4.3	
Initial temperature (K)	700	
Initial pressure (bar)	72	55
Sample time (ms)	3	
Simulation time (ms)	5	

The engine relevant thermodynamic conditions were determined using a nonreacting version of the full 3D simulation already described. Initial temperatures and pressures are cylinder averaged values at 20 degrees ATDC in the nonreacting 3D simulation. The sample time corresponds to 25 crank angle degrees of rotation at the engine speed, which is the time for the cylinder pressure to reach approximately half its maximum value. The soot has also reached a pseudo steady state in the homogeneous simulations by this time as seen in the asymptotic behavior of the curves in Figure 6.13.

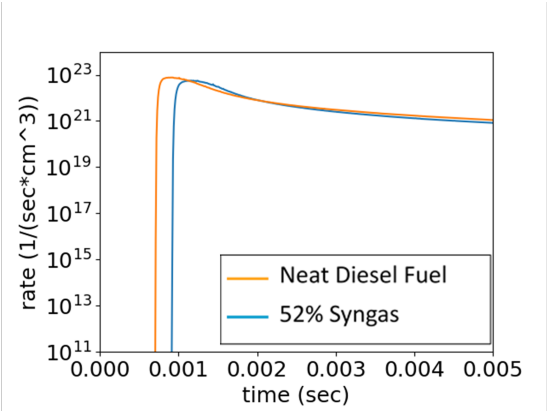

Figure 6.13: Rate of acetylene addition for 0D simulations

The simulation parameters are listed in Table 6.2. Figure 6.14 shows the particle size distributions for the pure and mixed homogeneous simulation cases. The distributions are unimodal at around 200 nm, which is approximately where the accumulation mode of the full 3D simulation PSDs is located. The numbers of particles per size is larger than what

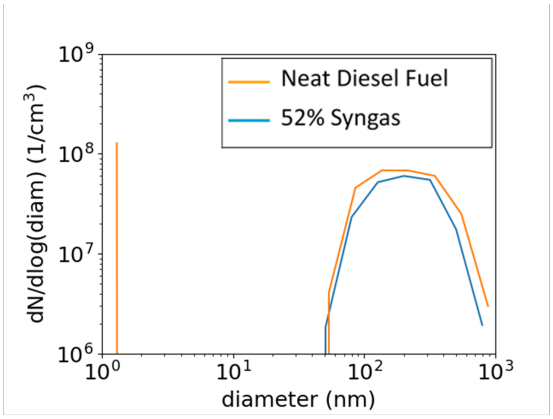

Figure 6.14: 0D simulation PSDs for neat diesel and syngas mix cases

is seen for the full 3D simulation PSDs, but the simulated homogeneous volume is rich, especially compared to the locally rich 3D volume. The differences between the neat and syngas mixed profiles are negligible on the scales pertinent to soot concentrations. This is the first indication that soot chemistry is unaffected by syngas.

To further evaluate the impact of syngas on soot chemistry, the rate of acetylene addition, the prime growth mechanism by the HACA model, is analyzed. Figure 6.13 shows the volumetric rate of acetylene addition for the pure and mixed cases over the duration of the simulation. The neat case is more reactive than the mixed case, so its addition reactions start earlier, but the syngas profile eventually reaches the same shape with a time shift. The similarity between the addition rates supports the findings of 6.14, that additional hydrogen via syngas has negligible effect on acetylene addition. The negligible effect of additional hydrogen can be explained using Equation 6.2 to show the system is saturated with hydrogen.

$$\frac{d}{d[H_2]}\frac{d[A_(i+1)]}{dt} = \frac{-K_4[H]}{(A1\cdot[H_2]+1/k_{-4})^2\cdot A1} \tag{6.2}$$

where $A1 = \frac{1}{K_5 k_6 [C_2H_2]^2} + \frac{1}{k_5[C_2H_2])}$.

If one further assumes that acetylene and radical hydrogen are much weaker functions of hydrogen than surface growth, then an expression for the sensitivity of soot surface growth

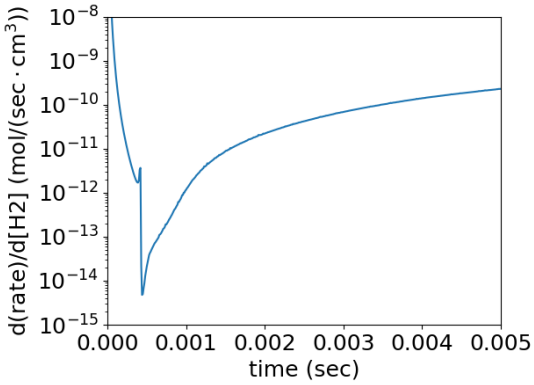

Figure 6.15: Sensitivity of soot surface growth rate with respect to hydrogen concentration

Table 6.3: C15 Pseudo 3D simulation parameters

Time of histogram	20 deg. ATDC
Initial pressure (bar)	60
Number of zones	100
Sample time (ms)	3

to hydrogen concentration can easily be formed and is expressed in Equation 6.2. This expression is solved for the neat diesel case to produce Figure 6.15. In the neat diesel case, there is no initial hydrogen concentration; accordingly, there is a brief initial sensitivity to hydrogen. However, well before the first soot is formed, a hydrogen saturated state is entered. The hydrogen sensitivity for the mixed case is similarly insensitive. Note that if acetylene and radical hydrogen are strong functions of hydrogen, then syngas may have an indirect effect on soot (i.e., an effect on gas phase chemistry that effects soot). However, the typical premise [25, 50, 119, 120, 129] and current investigation focuses on the direct effect of syngas on soot growth.

Stratification via mixing simulation

Based on the previous findings, syngas has limited affect the soot surface chemistry. This leaves effects of premixed syngas addition on mixing. The major aspect of mixing investigated here is fuel stratification. To isolate the effects of stratification from soot chemistry,

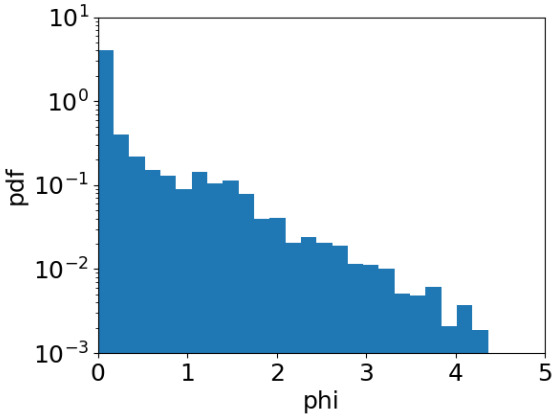

Figure 6.16: Volume weighted histogram, binned by equivalence ratio for the neat diesel case

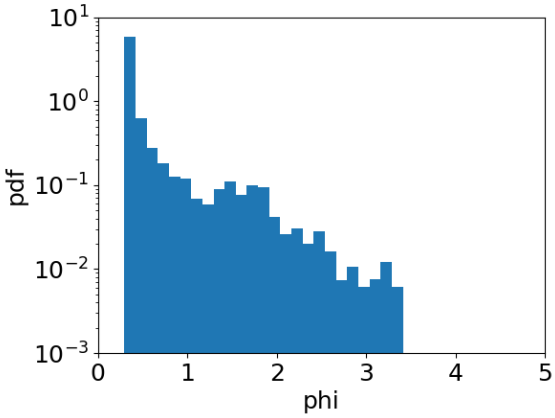

Figure 6.17: Volume weighted histogram, binned by equivalence ratio for the mixed syngas case

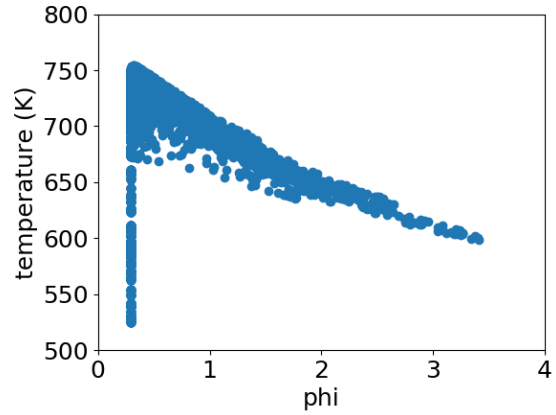

Figure 6.18: Scatter plot of cell temperature values vs equivalence ratio at 20 deg ATDC for non-reacting mixed syngas case

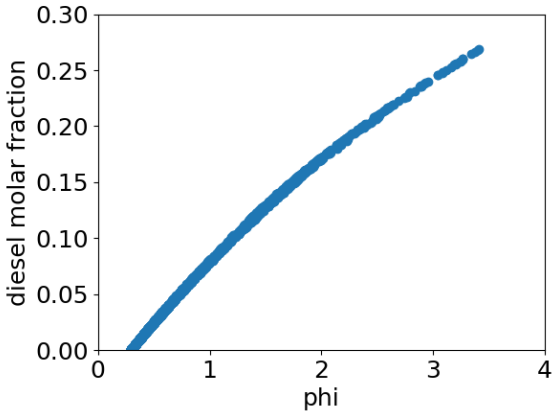

Figure 6.19: Scatter plot of cell diesel molar fraction values vs equivalence ratio at 20 deg ATDC for non-reacting mixed syngas case

fuel stratification is analyzed using pseudo-3D representations of the cylinder domain. For the neat and mixed cases, the nonreacting 3D simulations described earlier are discretized at 20 deg. ATDC into 100 volumes, or zones, of approximately homogeneous temperature and equivalence ratio. Figure 6.16 and 6.17 show normalized equivalence ratio histograms with a vertical scale of volume, indicating the percentage of the cylinder at a particular equivalence ratio and how much volume the zone with that particular equivalence ratio represents. Figure 6.18 and 6.19 show scatter plots of cell values of temperature and diesel mole fraction versus

equivalence ratio for the mixed case. Lines of best fit provide a relation between temperature, diesel fraction, and equivalence ratio. Similar relations are also created for the neat diesel fuel case. These relations give the initial temperature and diesel fraction for a zone with a particular equivalence ratio. An independent constant volume 0D simulation, like those discussed earlier, is performed for each zone. Cylinder cumulative results are summed based on the zones' volume. The constant volume zone representations are indicative of the phenomenon taking place in the actual 3D simulation, but not direct simulations, meaning the representations' results will not be the same as the full 3D simulation results. However, the authors find it a suitable way of separating the mixing effects. Other simulation parameters are listed in Table 6.3.

The constant volume zones model was used so that an additional test to rule out the chemical effects of syngas could be performed. In addition to the two multizone cases (neat diesel fuel and syngas mix) already described, a third case was added. The third case is identical to the syngas case (initial temperature, pressure, represented volume, etc.) except the syngas fuel was replaced with diesel fuel while maintaining the same zone equivalence ratios. In this way, the syngas chemical effects are removed while the mixing-based stratification effects are maintained.

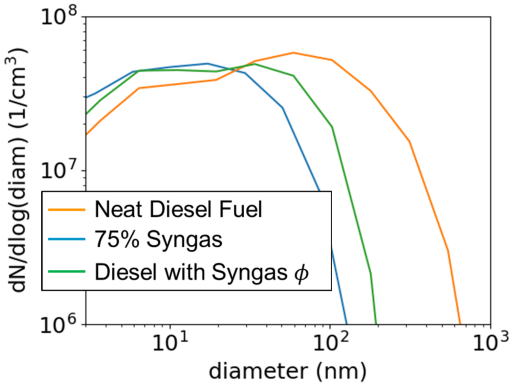

Figure 6.20: Zones simulation PSDs for neat diesel, syngas mix, and mix with diesel substitution cases

Figure 6.20 shows the zone volume weighted, cumulative sum particle size distributions for the pure diesel, mixed syngas and diesel, and with diesel replacing syngas. The diesel case shows more and larger particles than the other cases with the largest particles almost an order of magnitude larger. The syngas case has a slightly larger population of smaller particles because more of the cylinder volume is represented by lower equivalence ratio zones. Both cases lack the inception mode that the full 3D cases have because inception mode particles do not survive until the sampled 3 ms without agglomerating or growing. These inception particles may be present in the full simulation because of local heterogeneous areas of incomplete combustion that exist until closer to exhaust valve opening. The mixed case with diesel substituting syngas is almost identical to the mixed syngas case indicating that the main effect is the reduction in local equivalence ratios enabled by the substitution of diesel by syngas.

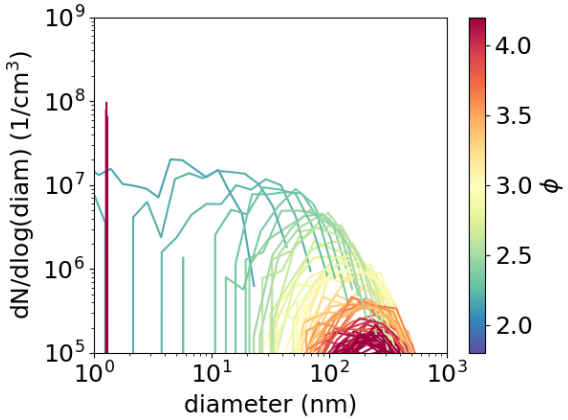

Figure 6.21: Individual zone PSDs from syngas mix case. Color indicates zone equivalence ratio

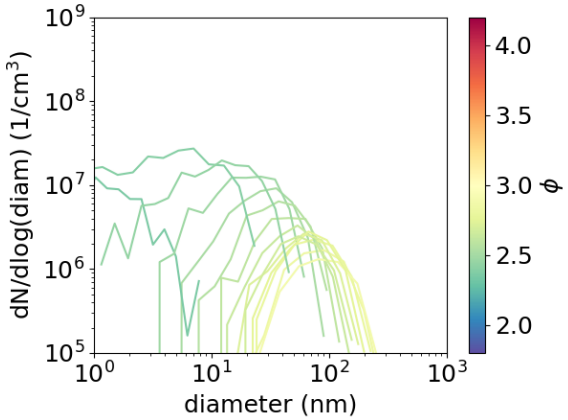

Figure 6.22: Individual zone PSDs from neat diesel case. Color indicates zone equivalence ratio

Figure 6.21 and 6.22 show independent, non-volume scaled particle size distributions for all zones in each respective case. It is clear that zones with higher equivalence ratios produce larger soot particles and that the presence of higher equivalence ratios in the neat diesel case create the larger accumulation mode observed in the particle size distribution.

In summary, the current model results explain the behavior observed in the experimental

results. In the experiments, addition of syngas was responsible for an overall reduction of accumulation-mode particles larger than 100nm and a substantial increase in nucleation-mode particles. The simulations show that the addition of syngas had very little chemical effect, soot surface chemistry or otherwise. However, premixed syngas substitution does lead to less fuel stratification and fewer rich zones, which are responsible for reducing the overall size of the soot particles, while increasing the number of small particles. Substitution of diesel fuel by syngas reduces the mixing requirements of the DI fuel as shown in [21]. Replacement of the DI fuel led to lower local equivalence ratios and, similar to an increase in injection pressure, leads to an increase in the concentration of smaller particles due to increased mixing. Thus, it is concluded that the substitution of diesel by syngas is the dominant parameter in the soot reduction process.

6.4 Conclusions

An experimental and computational study was performed using particle size sampling equipment combined with a 3D CFD and 0D cycle simulation approach. The soot formation characteristics of a reformed fuel engine concept was compared to a baseline diesel fueled engine. Several key conclusions can be drawn from the present analysis:

- Experimental results showed that the addition of syngas at energy percentages as low as 25 percent had a significant impact on the shape of the PSD. In general, syngas addition reduced accumulation-mode particle concentration while increasing nucleation-mode particle concentration.

- The conditions of the premixed fuel did not have an effect on the PSD results. The constant intake pressure cases resulted in the same effects seen for the constant premixed equivalence ratio cases even though the former showed extremely poor combustion efficiency. This indicates that the jet entrained reformed fuel, and reduction in the DI

fuel quantity are mostly responsible for the effects seen in the current experiments.

- For similar syngas energy percentage, RCCI can further reduce accumulation-mode particle concentrations when compared to DPI at similar conditions. This is a result of lower local equivalence ratios and temperatures, both of which suppress particulate formation.

- Model results showed that syngas addition did not affect the soot surface chemistry but did reduce fuel stratification which resulted in the changes to soot particle size distribution observed in the experiments. Additionally, as had been previously documented, the model results showed that areas of high equivalence ratio are responsible for larger soot particles.

7 MODEL APPLICATION: IMPACT OF THERMOPHORESIS

7.1 Motivation

Thermophoresis is the phenomenon of temperature gradient driven motion. In an IC engine, large temperature gradients exist at the walls because the walls are cooled and have a high thermal mass. Logically, one would expect soot, a very temperature sensitive entity, to be susceptible to large changes based on motion that necessarily cools it. Despite this conclusion, there has been relatively little research on the thermophoretic influence on soot generation. There has been work on the two premiss independently. There is certainly a large body of work on the temperature dependence of soot [38], and there has been work on thermophoresis effecting the motion of soot.

Blake et al. [116] performed an order of magnitude analysis on the equations characteristic of thermophoresis, Brownian diffusion, turbulent diffusion, inertial impingement, and electrophoresis effects deposition of soot onto cylinder walls and found thermophoresis was the strongest driver. They then performed experiments on a Cummins NH250 single cylinder test engine with a sapphire window that could be cooled. They found that cooling had a significant effect, 46.9 percent, on the soot deposition rate.

Tokura et al. [121] measured the soot accumulated in oil via blowby and the total amount of soot in the oil and concluded that most soot migrated to lubricating oil by mixing with the oil on the cylinder wall and getting recaptured by the scraping of the piston rings. Kittelson et al. hypothesized that the soot deposition rate onto cylinder surfaces is between 20 and 45 percent of the net soot emitted from their indirect injection diesel engine [67]. This theory was based on the characteristic equations of thermophoresis and particle drag that were evaluated under engine like conditions. The theory was corroborated by experimental measures of transmittance through a window subject to thermophoresis. Additional evidence comes from Kittelson et al. [68] in experiments where the exhaust is measured with an electrostatic probe

that captures the electrostatic field of soot just after the exhaust valve with crank angle resolution. They found the concentration of soot expelled during the exhaust blowdown is significantly higher than during rest of the exhaust cycle. For soot reentrained from the cylinder walls, the shear forces would be the greatest during the blowdown period [67].

Most simulation studies are concerned with the motion of soot within a coflow or counterflow flame where the temperature gradient and resultant thermophoresis studied is across the flame front. Lignell et al. [39] performed a DNS simulation with a four step method of moments soot model to investigate the diffusion mode of soot, mainly thermophoretic, with respect to the flame speed, and how soot can escape the flame front at certain mixture fractions.

Duvvuri et al. [31] ran diesel engine simulations using the sectional soot model with an additional submodel for soot deposition on the cylinder wall. They solved for the thermophoretic velocity of soot based on Equation 7.1 for every boundary cell and for every soot particle size section of the sectional model. In this way, the deposition rate was a function of the cell conditions and the particle size. Cell values were taken at the cell centers. It is unclear if the soot mass deposited on the wall was removed from the gas phase. Empirical matches to experimental data showed the simulated soot mass collected on the wall was correlated to the soot mass found in the lubricating oil over a range of operating conditions.

The present study will investigate the effects of thermophoresis using the direct soot model in an effort to identify its influence on the soot developed in an engine. First a Spray A case with measured TEM results from a probe mounted in the spray axis will be simulated to identify changes in the generated soot and flowpatern of soot around an unavoidable source of thermophoretic force. Then GM 1.9L engine cases will be simulated and the results will be compared to simulations without the thermophoresis model. This simulation will have particle trajectory histories and particle shape data in a soot study with thermophoretic effects. To the author's knowledge, this is unlike any previous attempts in the literature.

7.2 Theory

Again, thermophoresis is the phenomenon of temperature gradient driven motion for particles larger than the surrounding gas molecules. The phenomenon is ultimately an effect of entropy. Cooler (slower) gas phase molecules transfer less momentum to the larger particles than hot gas molecules. In a surrounding of gas under a temperature gradient, the large particles will be transported away from gas imparting more momentum. With this as a blueprint, based on molecular hydrodynamic theory, Brock [11] formulated the thermophoretic force equation in the continuum regime:

$$F_T = \frac{12\pi\mu\nu a C_s(\frac{\kappa_g}{\kappa_p} + C_t\frac{\lambda}{a})\frac{(\nabla T)_x}{T_0}}{(1+3C_m\frac{\lambda}{a})(1+2\frac{\kappa_g}{\kappa_p}+2C_t\frac{\lambda}{a})}, \tag{7.1}$$

where μ is the viscosity of the gas ,ν is the kinematic viscosity of the gas ,C_s, C_t, C_m are dimensionless factors of O(1) based on kinetic theory (commonly $3/4, 2.18, 1.14$ respectively - related to the previously seen Cunningham correction factor) ,κ_g, κ_p are the thermal conductivities of the gas and particles ,a is the radius of the particle ,T is the temperature of the gas ,T_0 is the average local temperature, and λ is the mean free path of the gas.

Transition regime slip factors were added to extend its accuracy to Kn on the order of $1e-10$. Talbot et al. [117] found that Equation 7.1 was theoretically valid, citing the works of, Brock [11] and Epstein [33] in the continuum and the slip, and Waldmann [125] in the collisionless limits, in the limiting cases of λ/a, ignoring an error of C_s/C_m in the free molecular limit. Theoretical analysis by Gorelov et al. [46] that was based on a numerical solution to the Boltzmann equation predicted a reduction in thermophoretic force for λ/a around unity. Talbot et al. experimentally validated equation for conductive particles within an error of 20 percent over a range of Kn with the correct selection of the slip coefficients.

Based on Equation 7.1, thermophoretic force can be easily ignored when there is not a large temperature gradient or when the Knudsen number is large ($F_T \propto \frac{1}{Kn}$ for $Kn > \frac{\kappa_g}{\kappa_p}$). For particles in a flow, this force is at odds with the viscous drag force, modeled by the

Stokes-Cunningham Equation 3.2. As seen in Section 3.4, the drag force is substantial for soot, but it is not obvious how thermophoresis is comparable in driving soot. Note that both models are dependent on the particle size which further complicates the matter. A ratio of forces produces a dimensionless number, $F_T/F_{viscous}$, indicative of the major driver of particle motion.

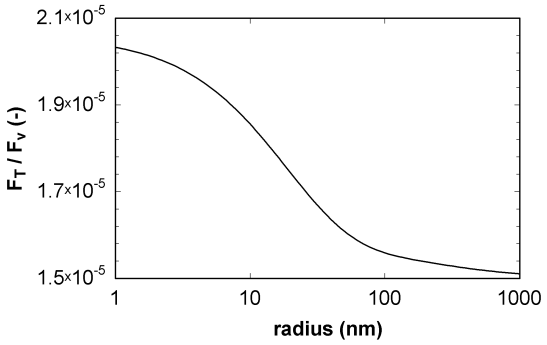

Figure 7.1: Particle forces ratio versus particle size

Figure 7.1 shows a plot of this ratio versus particle size. For engine relevant conditions, the ratio was solved for particles from 1 nm to 1000 nm. A temperature gradient of 60 K/mm approximating the gradient outside of the laminar sublayer [132] and a gas velocity velocity equal to the average piston speed were used as parameters. Particles were assumed to be spheres for simplicity even though that assumption is certainly wrong, with soot having a fractal dimension closer to two than three. The relationship between the two forces should be relatively stable with respect to the shape of the particles for this cursory investigation. spanning incipient mode to accumulation mode particles. It is clear that the thermophoretic force is inferior to the drag force, however, it is also clear that the magnitude of the force ratio is relatively constant across all particle sizes.

7.3 Implementation

The thermophoresis effects on soot parcels was incorporated by way of a submodel. The submodel is run and its effects applied in the parcel motion substep of the operator splitting algorithm of Figure 2.3. The net effect is the parcel getting accelerated towards the wall by the force calculated using Equation 7.1 and the Euler approximation of Newtons momentum law. Figure 7.2 shows a flowchart of the parcel motion substep with the submodel applied.

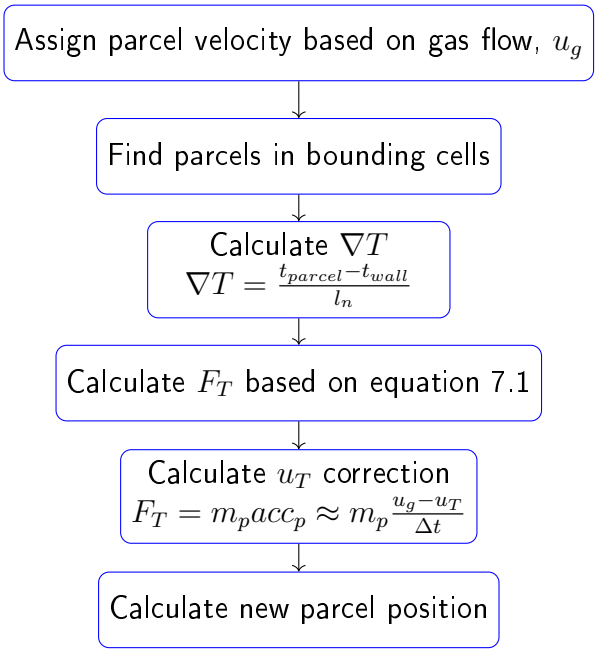

Figure 7.2: Simplified flow chart of thermophoresis implementation

As mentioned in Section 2, the soot parcels are assumed to follow the flow perfectly without the consideration of thermophoresis, so the default velocity of the parcel is based on the interpolated cell velocity. Because applying the effects of thermophoresis to all parcels for all surfaces would not only be computationally expensive, it would also be difficult, the next step is to identify which parcels meet the threshold of considering thermophoretic effects. This is handled differently for the Spray A simulation and the GM 1.9L simulation and will be discussed further in their sections. The temperature gradient is calculated as the temperature of the parcel, less the temperature of the wall, over the normal distance between the two.

This is certainly flawed due to the thermal boundary layer and the law of the wall model temperature calculation would be a much better fit, however, the results as is should still be indicative of the importance of thermophoresis, if not perfectly accurate. F_T can now be calculated using Equation 7.1. The parcels average collision diameter is used for the same reason it is used in the optical calculations of Section 4.2, the equation is based on the collision frequency with the particle. Once the force is known, the parcels new location can be determined by calculating the acceleration from the force, average mass of the parcel, and the flow timestep of the simulation. Figure 7.1 shows that although choosing the average particle diameter is flawed, and different sized particles within the parcels' representation would be affected differently, they would not be affected differently by more than a factor of five.

7.4 Simulations

Again, the objective of this work is to find the significance of thermophoresis in TEM measurement techniques that rely on thermophoresis for particle deposition. Then, once the effects of thermophoresis are proven to be nonnegligible, the study will be extended to a diesel engine running at low load. This study is cursory and because of a relatively simple thermophoresis model, the results are not expected to be quantitatively correct, but are expected to provide qualitative guidence.

Additionally, the drivers of thermophoresis will be limited to simulation boundaries. Thermophoresis affects all soot within a temperature gradient, however, because thermophoresis's relative weakness to viscous drag and soot oxidations' sensitivity lower temperatures, only the thermophoresis driven by low wall temperatures will be considered as it is especially interesting.

Spray A

Just like in the optical properties investigation, §4, Spray A is a convenient case format for research, for both experiments and simulation, because of its static domain and relatively easy access. i.e. the confounding variables are minimized. Kondo et al. [71] ran Spray A experiments in which particles were collected via thermophoretic forces, making it a good specimen for simulation.

The case parameters will be introduced by comparison to the experimental Spray A work of Skeen et al. [111] outlined in Section 3.3, instead of reiterating all of the same case parameters. The major deviation is a TEM grid directly inline and 70 mm downstream of

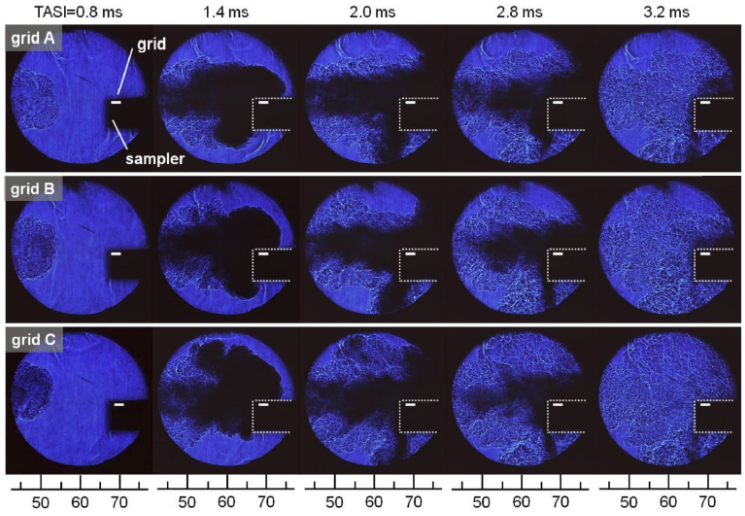

Figure 7.3: Laser shadowgraph of experimental spray. TEM grid placement is indicated by the white rectangle. The grid holder is the dashed rectangle. [71]

the jet that collected soot particles on its surface under the influence of thermophoresis. Figure 7.3 shows the placement of the grid during injection. The probe holding the TEM grid extends toward the injector tip, just off axis and such that the TEM grid is parallel with the jet so that direct impingement is not a mode of deposition. Diesel is injected at 1500 bar for 2.5 ms into 15 percent oxygen, 1000K ambient conditions resulting in a pseudo-steady state duration from 1.5 to 2.5 ms after the start of injection. The conditions are summarized in Table 7.1.

Table 7.1: Spray A with diesel fuel experimental conditions

Case	without thermophoresis	4 cm	7 cm
Grid location downstream	none	4 cm	7 cm
$T_{ambient}$	1000 K		
$\rho_{ambient}$	9.5 kg/m^3		
$O_2, ambient$	21.00 mol/mol %		
$N_2, ambient$	75.00 mol/mol %		
Fuel	Diesel		
Inj. Duration	2.5 ms		
Nozzle	140 μm		
Injection Pressure	800 bar		
Pseudo-steady	1.5-2.5 ms		

Table 7.2: Spray A with diesel fuel simulation parameters

Simulation package	KIVA3v Rev 2 + ERC submodels
Soot model	Direct
Number of parcels	$O(1000)$
Number of particles	512
Turbulent model	RANS (RNG k-ϵ)
Reaction Mech.	Multi component w/ PAH [101]
Fuel surrogate	$nC_{16}H_{34}$, C_7H_8 (90/10, %molar)
Mesh	Pseudo 2D
Base mesh (mm)	1.0

Excepting the diesel surrogate used to simulate the injected diesel fuel and the thermophoresis model, the simulation parameters of the present case are identical to those of Section 4.3 and 3.3 and outlined in table 3.3. The diesel surrogate is the same used in the GM 1.9L simulations outlined and validated in Section 3.3.

The effects of thermophoresis on soot from an axially mounted TEM grid was modeled by treating an axial point as origin of thermophoretic force for particles in a 1 cm radius. The temperature of that point remained constant at the initial domain temperature of 1000 K. This was based on a constant surface temperature assumption of the TEM grid that was based on a thermal time constant of the TEM grid much larger than the duration of the Spray A combustion and a Biot number much smaller than one. The distance from this point

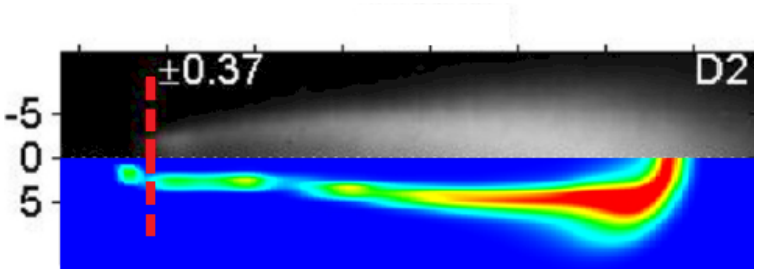

Figure 7.4: Spray A with diesel fuel steady state lift off length comparison

was used as the distance to the TEM grid. 3D effects of the grid or the grid holding probe, that laid along jet axis, were ignored.

OH chemiluminescence images were not published in the work of Kondo et al. [71], however, similar Spray A conditions with a diesel fuel were published by Kook et al. [73]. That data is temporarily used for further validation of the combustion simulation.

Figure 7.4 shows a comparison between the measured OH chemiluminescence and simulated OH mole fraction under pseudo steady conditions, just like Figure 3.5. In the figure, the injector is out of view on the left. The lower half is the simulated OH concentration across the centerplane at 2.5ms and the upper half is the ensemble averaged measured OH chemiluminescence. Both images are to scale and span the same domain. Again, this figure is used to validate the spray simulation accuracy since it involves mixing and combustion. The overall jet structure is captured by the simulation well; however, the lift-off length is over predicted by approximately 3 mm. This agreement is similar to other studies (e.g., [113]) and is deemed acceptable.

GM 1.9L

The previously discussed GM 1.9L cases used for validation of the combustion and soot model in Section 3.3 are used again here for the investigation because the operating conditions are representative of sooty, low load, cold start conditions. This time, however, the KIVA simulation with the direct soot model will be used so that soot values are available during

the simulation for thermophoresis calculations.

For the GM 1.9L simulations, parcels within a boundary cell are subject to the effects of thermophoresis. It is assumed particles further than a cell away from the boundary are unaffected by thermophoresis because of the very low force of thermophoresis relative to drag and the 6 mm characteristic length of the mesh.

7.5 Results

Spray A

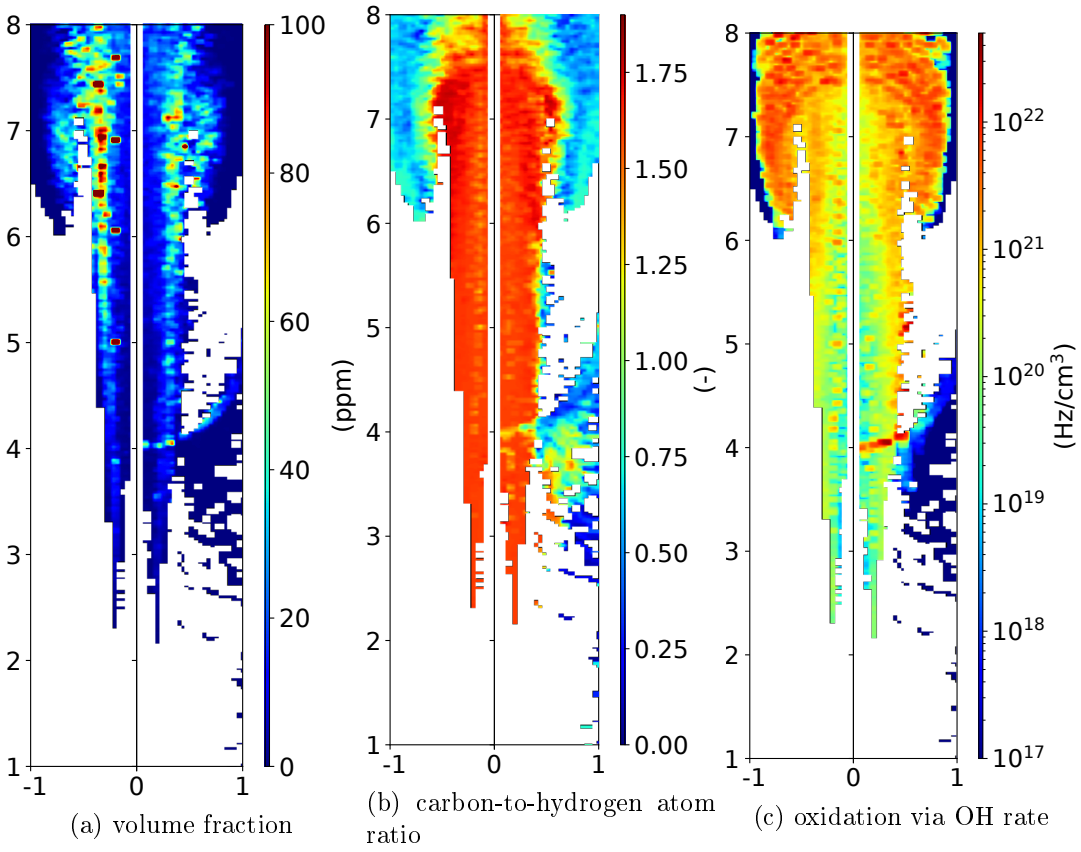

(a) volume fraction

(b) carbon-to-hydrogen atom ratio

(c) oxidation via OH rate

Figure 7.5: Surface plots of the time averaged indicated value. For every variable, the 4 cm case is on the right and the without thermophoresis case is on the left and has been mirrored across the centerline. Surfaces are bisections of the central axial plane and regions without soot are left white.

Figure 7.5 show surfaces colored by the corresponding scale for the indicated value in the same format as Figure 4.1. For every variable, the without thermophoresis case on the

left and the 4 cm case on the right. The 4 cm case is displayed rather than the 7 cm case because the effects of the thermophoretic region are easily identified in the 4 cm case while the effects are hidden by transient jet plume effects in the 7 cm case. Figure 7.5a has surfaces colored by volume fraction. The volume fractions are generally similar in form to the volume fraction of Spray A using dodecane fuel, seen in Figure 4.1, except that the concentrations are approximately five times higher and the region of high soot mass is much further downstream. Likewise, the same is true for the carbon-to-hydrogen ratio and oxidation vi OH. As such, discussion of the generalities of the figures will be relegated to the earlier section, §4.4, and only thermophoretic effects will be analyzed here.

The most glaring difference is the structure protruding from the TEM grid. The cup formed with the base at the TEM grid is a line of equilibrium where the thermophoretic force balances the viscous drag force. The equilibrium is stable on the upstream side of the cup. If a parcel passes through the cup, the parceled will continue downstream. Particles are added to the cup within the stream at all times, however, only parcels that are part of the jet plume as the plume passes the equilibrium line and get left behind are able to become part of the cup outside of jet. Outside of the jet, the gas velocity is low, allowing parcels to idle even though the thermophoretic force is also low. As the parcels get nearer to the centerline, the thermophoretic force gets stronger and the stable line gets shallower. There is a fan of ultra low mass soot parcels in a nonsensical location underneath the cup and outside of the jet. This effect is a function of a numerical error caused by first order accurate operator splitting Euler time step numerical scheme used to couple the thermophoresis model. These parcels were once at equilibrium but then underwent rapid oxidation. The newly very light and small parcels are propelled backwards by a relatively stronger thermophoretic force that overpowers the viscous drag and propels them backwards. Aside from the cup, the 4 cm case also shows lower maximum volume fractions of soot by aproximately half.

Figure 7.5b compares the soot particle carbon-to-hydrogen atom ratio. As discussed in

Section 4.4, the carbon-to-hydrogen ratio is an indicator of the number of surface reactions that have occurred to a particle and consequently, is an indicator of the history of the parcel since surface reactions are typical in soot that has matured and grown in surface area. Again, the cup is clearly visible as a streak of much lower carbon-to-hydrogen ratio. Only the head has regions of carbon-to-hydrogen ratio that match the cup. The cup is evident at all radial positions within the jet, however, the carbon-to-hydrogen ratio seems to increase as the radial distance decreases. The lower carbon-to-hydrogen ratio in the equilibrium line shows that thermophoresis is effecting the local soot type.

Figure 7.5c compares the soot particle oxidation by OH rate. This figure shows that oxidation along the cup is increased but only significantly within the jet. Outside of the jet, where things are cooler (Figure 7.6), oxidation of older particles from the passing head of the jet is much slower. This figure also shows the thickening effect that thermophoresis has the most clearly. The sooty region of the jet becomes wider in the 4 cm case such that the edges of the region enter the oxidation regime as seen by the increased oxidation rate and the lower carbon-to-hydrogen ratio.

Figure 7.6 shows surfaces in the same format as Figure 7.5, however, these are colored by Eulerian cell values of temperature. Note that the high temperature region reaches much further upstream and the lower temperature core is thicker in the 4 cm case. The highest temperature conic is delayed in the 4 cm case until almost the exact location of the TEM mesh. This highlights the coupledness of the soot model with the rest of the simulation since adding the thermophretic forces only affected the parcel motion and had no direct impact on the gas phase.

Figure 7.7 follows a similar format to Figure 4.3 except only two axial locations are displayed corresponding to the two TEM grid locations. Figure 7.7a shows PSDs approximately 4 cm downstream and Figure 7.7b shows PSDs approximately 7 cm downstream from the injector tip. The top plot of every column corresponds to the 4 cm case, the middle plot

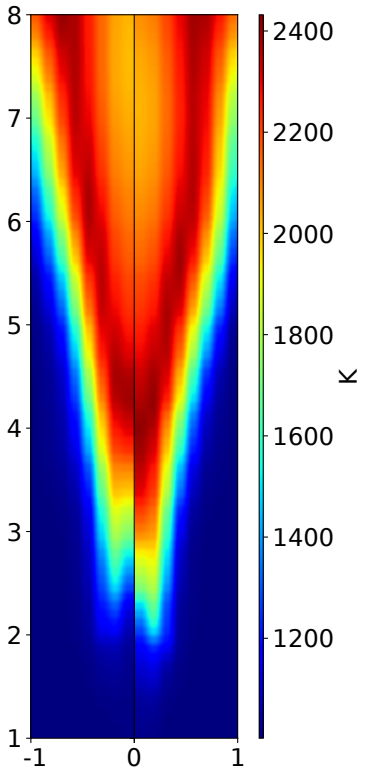

Figure 7.6: Surface plots colored by temperature. The 4 cm case is on the left and the without thermophoresis case is on the right. Surfaces are bisections of the central axial plane of Eulerian cell values.

corresponds to the 7 cm case, and the bottom plot corresponds to the without thermophoresis case. The PSDs are colored according to their radial location according to the scale in Figure 7.7 and the black curve is the axial cumulative. Only a sample of the parcels are plotted individually so that individual PSDs are still identifiable. Enough curves to see all of the interesting patterns are present. The PSDs are similar in concept to those throughout the document, such as Figure 3.2, however, here the measured results are reported in terms of radius of gyration and cumulative particle mass since they will be compared to measured results of automated TEM image processing and not SMPS instruments. Reporting in terms of particle mass also allows the results to be on linear scales since the smaller particles weigh less. The bimodal shape disappears as the much more prevalent incipient species population almost vanishes when measured by weight.

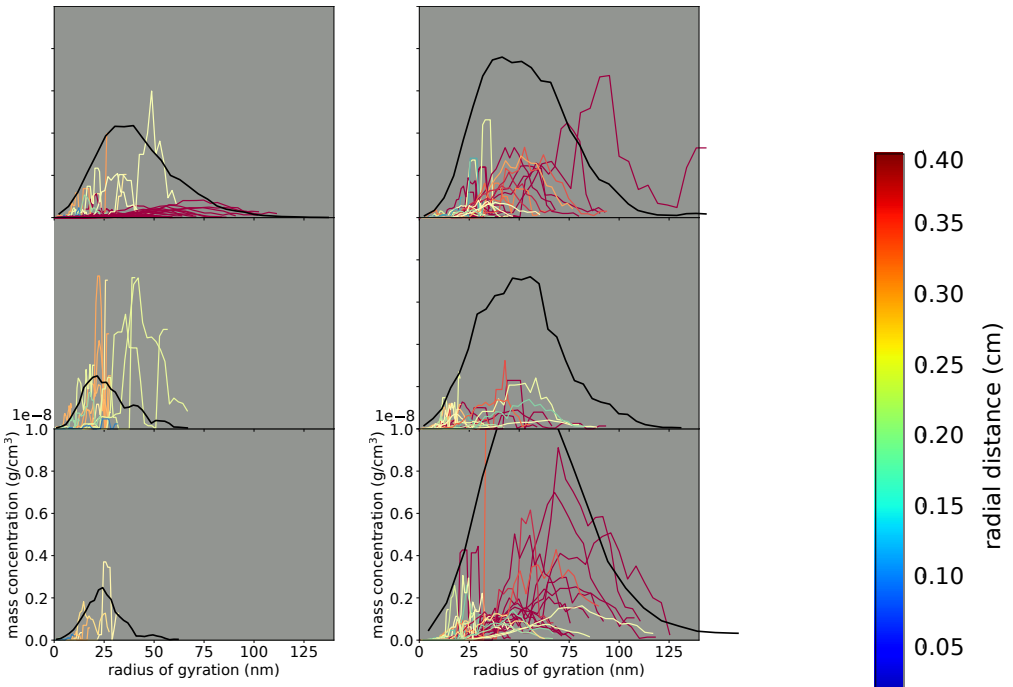

(a) 4 cm downstream (b) 7 cm downstream

Figure 7.7: Time averages of PSDs at the indicated axial location. All plots are on the same scale. For each row, the top plot is the 4 cm case, the middle plot is the 7 cm and the bottom is the without thermophoresis case. Each colored curve represents an individual parcel, colored by its radial distance according to the scale on the right. Each black curve represents the axial section cumulative.

Figure 7.7a shows the PSDs at the location that the 4 cm case has its TEM probe. Since this is 3 cm upstream of the 7 cm case probe, despite a few radical individual PSDs of the 7 cm case that get washed out in the average, the 7 cm and without thermophoresis cases are both relatively similar. The 4 cm case, however, has approximately twice the peak soot mass and parcels that are approximately twice as large. All of the largest soot particles in the 4 cm case come from regions far from the central axis. This pattern corresponds well to the regions of high volume fraction seen in Figure 7.5a, indicating thermophoresis is drawing the large particles.

Figure 7.7b shows the PSDs at the location that the 7 cm case has its TEM probe. At 7 cm downstream, all of the PSDs are much larger than at 4 cm. The 4 cm and 7 cm case are

now more similar than the without thermophoresis case, at almost half the peak soot mass. In the 7 cm case there are larger particles much nearer to the central than in either of the other two cases.

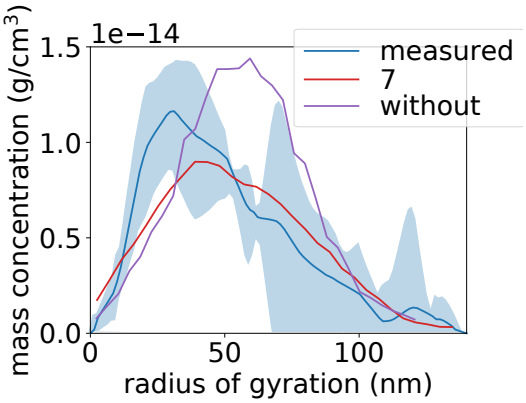

Figure 7.8: Simulated without thermophoresis and 7 cm case and measured radius of gyration versus cumulative mass PSDs. The error band is the 95 percent confidence interval. Simulated PSDs are the axial average at 7 cm downstream from the injector nozzle.

Figure 7.8 shows the measured and simulated radius of gyration PSDs. The error band of the measured data is the 95 percent confidence interval based on the variance of three reported PSDs. The simulated data is the axial average 7 cm downstream from the tip of the injector, where the TEM grid was during measurement deposition. The simulated data has been scaled to match the magnitude of the measured data because although there is a thermophoresis model, there is no deposition model so there is no way to quantify how the PSD of the soot in the volume near the TEM probe would be deposited onto the surface area of the TEM grid. Both simulated results match the measured data within approximately 15 percent across particle size range after scaling for best fit. Of the two simulated cases, the 7 cm case has a slightly better fit by having a smaller radius of gyration at the peak mass.

The Spray A simulations have shown that thermophoresis has a significant effect on the motion of soot which consequently even effects the fluid flow. The altered paths of soot result in variations to the PSDs to varying degrees depending on where it is sampled. At the location the measured results were taken, the thermophoretic force had an indeterminate

effect because of a missing deposition model. The cumulative soot at the axial distance of sampling was relatively similar between the two cases, however, the 7 cm case did have larger particles closer to the TEM grid than the without thermophoresis case did.

GM 1.9L

Based on the positive results seen with the Spray A case, the study continues to the GM 1.9L case in which the domain varies and the motion of soot is much less predictable. For brevity, the investigation concentrates on the conventional injection case unless otherwise specified.

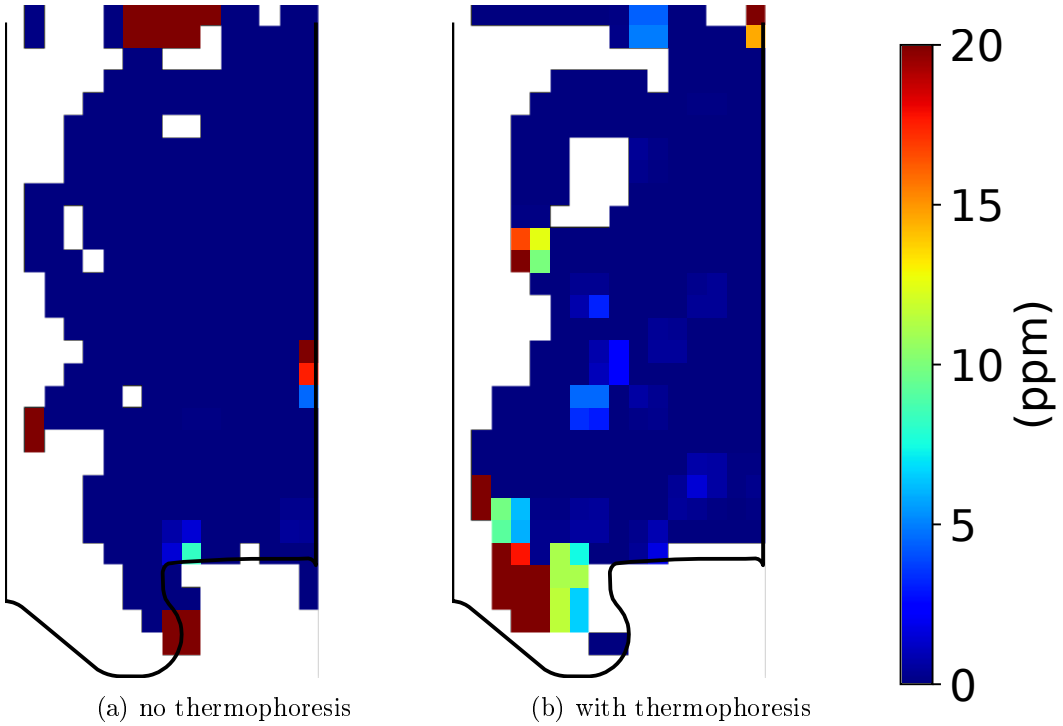

(a) no thermophoresis (b) with thermophoresis

Figure 7.9: Surfaces based on the conventional case and colored by volume fraction according to the scale. One surface considers thermophoresis and the other does not. White areas indicate a region without soot.

Figure 7.9 is similar in execution to Figure 5.7. Surfaces are generated by interpolation on a uniform mesh that is on the r-z plane. The extended hybrid model's easy scalability compared to the direct model, discussed in Section 2.5, leads to an order of magnitude

disparity between the number of parcels. Figure 7.9 is much more coarse than Figure 5.7 because of the parcel disparity. Pixels outside of the drawn cylinder boundary are from parcels within pixels that do not sit completely in the boundary. Figure 7.9 shows surfaces for the simulated case with and without thermophoresis effects considered, colored by the volume fraction. Again, areas without soot are left blank. In the cylinder without thermophoresis, the regions of highest soot concentration are much more concentrated than with thermophoresis. The regions of highest concentration are not colocal with the thermophoresis case either. Without thermophoresis, the center of the head and the bowl undercut are regions of notable soot. With thermophoresis, the perimeter of the head and near the center of the piston bowl are the high soot regions.

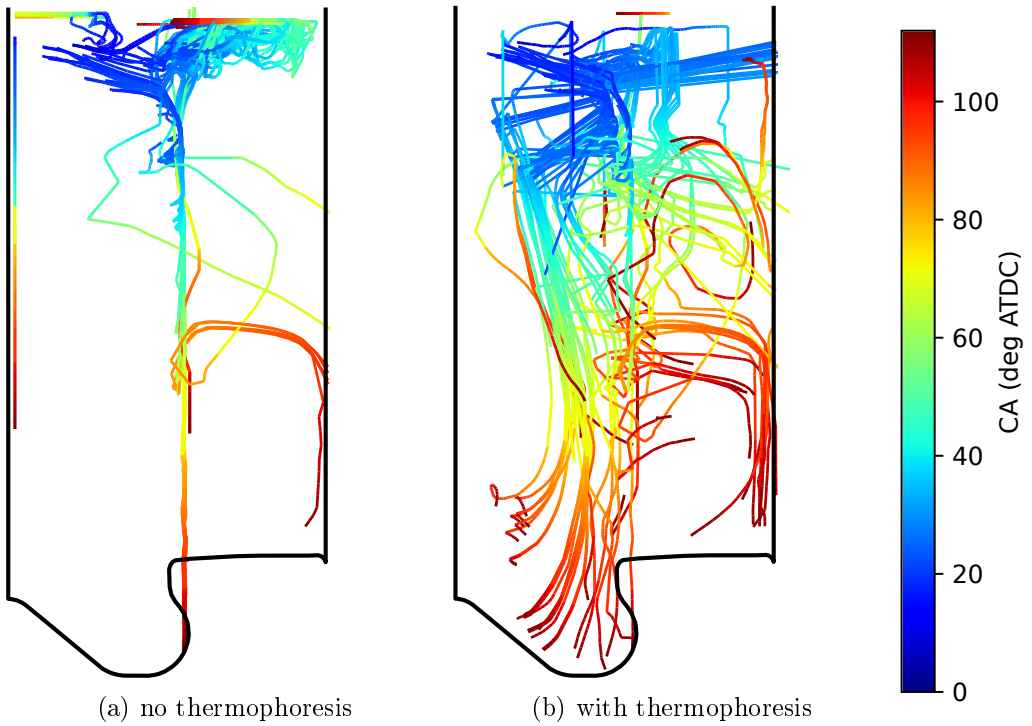

(a) no thermophoresis (b) with thermophoresis

Figure 7.10: Parcel paths of the 100 parcels with the largest soot mass contribution to the domain at the time of EVO for the indicated conventional simulation with or without soot. Paths are colored according to the crank angle ATDC. Paths that hit a cylinder wall and stop moving will terminate in whatever color corresponds to the time that movement stopped.

Figure 7.10 shows the paths of the 100 largest, by mass, parcels at then end of the simulation, over the duration of the simulation. The color of the path corresponds to the

crank angle when the parcel is at that location, according to the scale. Figure 7.10b shows the paths for the simulation with thermophoretic effects considered. Figure 7.10a shows the paths for the simulation without thermophoretic effects considered. If a parcel stays in the same location, like a parcel hitting a wall, the path will hold is last color. A few parcels in Figure 7.10a are trapped on the concave bowl surface early in the expansion cycle and their path produces a perfectly straight line downwards. The starting locations and time of all of the parcels in either figure is very similar, in the axis of the injection path near 10 to 20 deg ATDC. The figures disagree highly on where the heaviest parcels end up and how they get there, however. With thermophoresis, most of the parcels distribute widely along surfaces. The paths fan out and sweep a large portion of the cylinder volume. Parcels that wind up in the top quarter of the cylinder stop moving after about 35 deg. ATDC. Without thermophoresis, the 100 largest parcels are much more uniform. The proportion of largest parcels that wind up on the head is disproportionately high, indicating surfaces are still responsible for generating soot even if there is not thermophoretic motivation to be on the boundary. Parcels that stay in the top quarter of the cylinder continue to move until at least 45 deg. ATDC which is later than with thermophoresis.

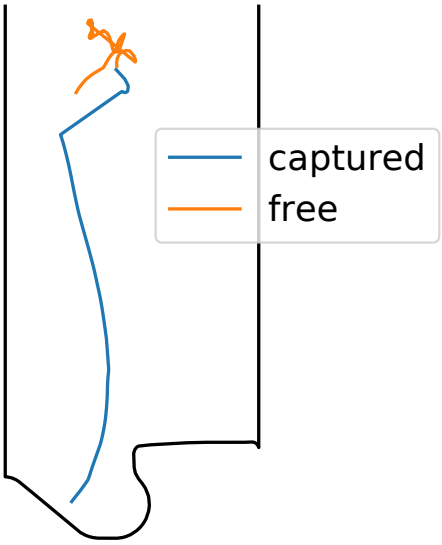

Figure 7.11: Paths of the parcel with the largest soot mass contribution to the domain at the time of EVO and a parcel that initializes in a very similar location but does not make it to a wall

Figure 7.11 shows the paths of two selected parcels, the largest and one of the smallest at EVO, from the simulation considering thermophoretic effects. The largest will be referred to as the captured parcel and the smaller parcel will be called the free parcel based on their movement histories. Both parcels have a starting location within 2 mm of each other, although the captured parcel is generated earlier. The captured parcel quickly makes it to the piston bowl where it rides down for the majority of the expansion stroke. The free parcel wanders until EVO when it is still within the cylinder and far from any walls.

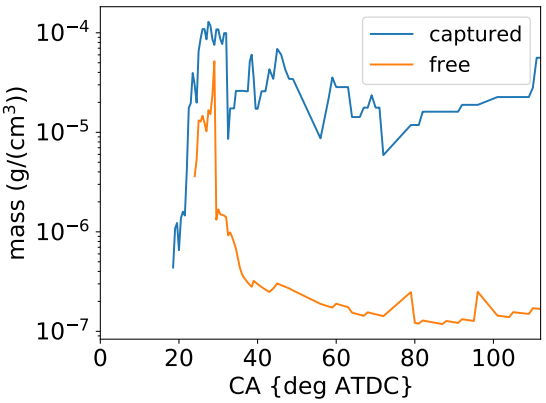

Figure 7.12: Parcel mass vs crank angle for the two followed parcels of Figure 7.11

Figure 7.12 shows the mass over time of the tracked parcels of Figure 7.11. The captured parcel quickly reaches a relatively steady state mass that is maintained within an order of magnitude for the duration of the cycle. The free parcel quickly reaches a similar mass on a similar trajectory but it is abruptly consumed to its own roughly steady state value that is approximately three decades lower than the captured parcel. Even though the parcels finish with very different masses, both parcels start from a similar prospect.

Figure 7.13 shows the PSDs of the two tracked parcels from Figure 7.11. The PSDs are colored according to their sample time using the same scale of Figure 7.13. The captured parcel PSDs follow the expected pattern of an initially large incipient population that is consumed at the cost of moving the mode to a larger but less dense mean. The free parcel

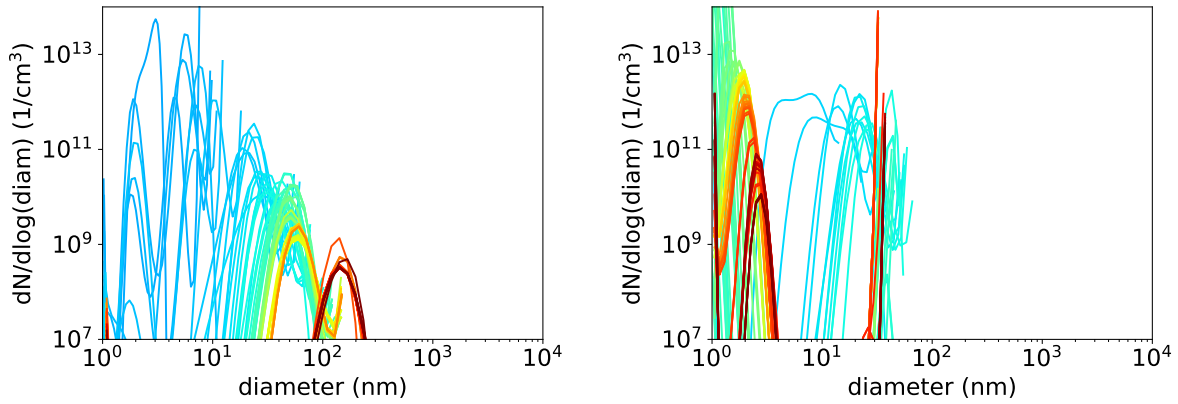

(a) The captured parcel

(b) The free parcel

Figure 7.13: PSDs of the indicated parcel, colored according to the crank angle

has a later start but at its earliest times it has an even larger midsized particle population. All of these particles are abruptly lost and replaced with a very large population of very small incipient sized particles that decay until EVO. The patterns seen in PSDs corroborate the mass histories of Figure 7.12.

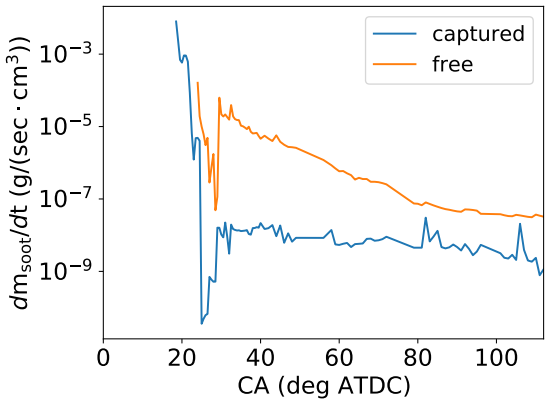

Figure 7.14: Inception rate vs crank angle for the two followed parcels of Figure 7.11. The rate is reported in terms of mass by scaling the inception rate by the mass added from an inception event.

Figure 7.14 shows the inception rate over time of the tracked parcels of Figure 7.11. The rates of Figures 7.14 and 7.15 are reported in terms of mass of soot by scaling the rate by the effect of the event. This allows easier comparison between the phenomenon. The

rate is reported in terms of mass by scaling the inception rate by the mass added from an inception event. The free parcel's inception rate is larger than the captured inception rate at all times. Aside from an initial dip and return, it also monotonically slows until EVO, mirroring the decline of its PSD of Figure 7.13b The captured parcel's rate starts high but quickly plummets before bouncing back to a steady rate until EVO. This plot exposes the nonnecessity of inception for a large soot population.

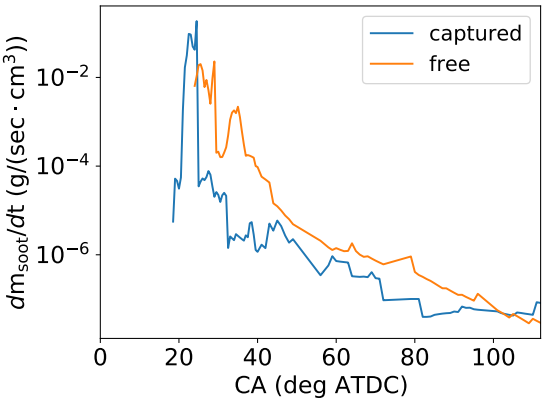

Figure 7.15: Oxidation rate vs crank angle for the two followed parcels of Figure 7.11. The rate is reported in terms of mass by scaling the oxidation rate by the mass added from an oxidation event.

Figure 7.15 shows the oxidation rate over time of the tracked parcels of Figure 7.11. The oxidation rates of both parcels is similar, roughly to within an order of magnitude, over the entire duration of the cycle, as long as they both exist. Oxidation quickly jumps for the captured case, right after it's generation, but otherwise the rate monotonically descends until EVO, following the temperature profile. Although similar, the free parcel's oxidation is alway slightly higher while the parcel consists of incipient particles with less surface area for surface reactions to occur on.

Figure 7.16 shows comparisons of simulated and measured PSDs for the three cases. Each simulation was performed with and without considering thermophoresis. All of the simulations in which thermophoresis is not considered produce far less soot, in number and in size, than the measured results. In Figure 7.16b the soot population is completely out of scope

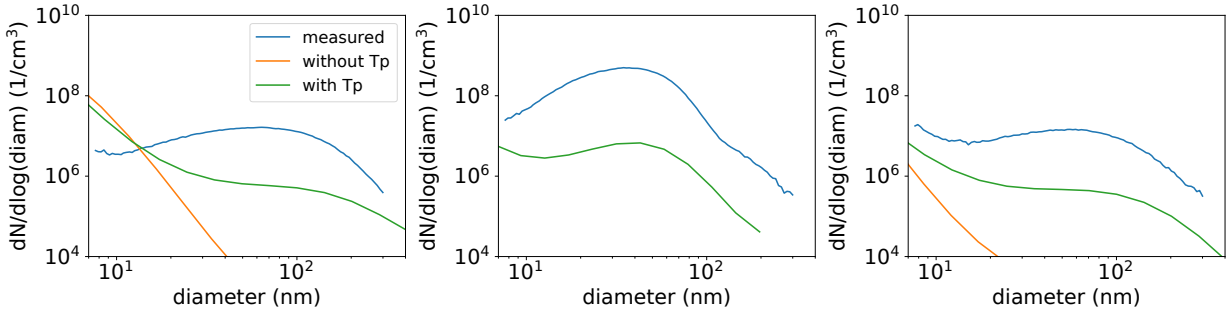

(a) 3rd SOI 9 (b) 3rd SOI 23 (c) conventional

Figure 7.16: Measured and simulated PSDs at EVO from the GM 1.9L cases. Simulations are run with and without the effects of thermophoresis considered.

without thermophoresis considered. The agreement between simulations with thermophoresis considered and measured data is very similar to the extended hybrid simulation results seen earlier. In qualitative terms, the match of the simulations with thermophoretic forces considered and measured data is easily identifiable. The simulated PSDs for the SOI9 and conventional cases with thermophoresis of Figures 7.16a and 7.16c are both similar and show the subtle accumulation mode with a tail toward a large incipient population. Their similarity matches the measured results' similarity. For the SOI23 case with thermophoresis shown in Figure 7.16b, the separation of the incipient and accumulation modes is much more distinct. The measured results also show a much more prominent accumulation mode, but lack any indication of an incipient population. Quantitatively, all of the measured results are underpredicted by approximately an order of magnitude across all cases. The smallest deviation occurs for the smallest particles, where the simulated results increase drastically.

7.6 Conclusion

A relatively simple thermophoresis model was applied to simulations with a highly detailed soot model, allowing the coupling between soot and thermophoresis to be directly observed. A Spray A case with a TEM probe was simulated to find the effect of thermophoresis was present, however, it had questionable effects the measurements because of the location of the

TEM probe. Thermophoresis acting directly on the particles did have an indirect effect on the flowfield which is only possible with the full coupling of the model.

A light duty diesel engine was then simulated for three different injection schemes with the direct soot and thermophoresis model. Thermophoresis had a large effect on the engine PSD results by controlling the path of the largest parcels. Without thermophoresis, soot parcels were not likely to stay near the cooler cylinder walls and oxidation consumed the accumulation mode particles. With thermophoresis, the domain cumulative PSDs for the three cases retained their accumulation mode populations. Matches to measured PSDs were qualitatively good fits, with matching identifiable characteristics for all three cases. All of the simulations underpredicted the quantity of particles but the quantitative results were mostly within an order of magnitude.

8 CONCLUSIONS AND FUTURE WORK

8.1 Conclusions

In this document a highly detailed stochastic soot model limited to 0D simulations is coupled to 3D domains through the use of a LPEF method. Concepts and previous work from simpler models for soot, Lagrangian parcel tracking models for particulate, and partitions for sets are all used in developing the model. Validation for the model followed the "bottom up" methodology, requiring the combustion simulation, SWEEP simulation, coupling assumptions, and discrete mesh errors to be validated in turn. The combustion validations were done in accordance to literature norms. For a spray simulation, the liftoff length was compared and agreement to within 3mm was found. For a low load diesel engine with multiple injection strategies, the pressure and heat release rates were compared to find they were within 5 percent over the duration of the cycle. The SWEEP simulation is restricted to 0D cases or burner stabilized flames where the simulated domain follows the gas flow so the moving reference frame is 0D. Here the simulated particle size distributions and total soot mass are compared with measured results. Assumptions intrinsic to the model and required for simple use of the model are validated through dimensionless numbers, numerical studies, and convergence studies.

Many subinstances of SWEEP simulations are well ordered for multithreaded processing, however, the eventual coupling of the Lagrangian parcels to the Eulerian fluid creates a weakest link problem where the weakest link is unknown before the start of the simulation. A dynamic load distribution algorithm is implemented via MPI. An extended hybrid variation of the model is created to further avoid slowdown from the soot simulations by allowing the highly detailed, more expensive soot simulation to be run in a postproscessing step. The extended hybrid model requires a surrogate soot model that is capable of impacting the rest of the combustion simulation in the same way that the detailed soot model would to be

valid, however, validation steps saw success with a multistep model. An added benefit to the postprocessing nature of the extended hybrid model is its easy use with proprietary software packages.

Then the model is used in multiple case studies, showcasing capabilities not had by other models. Conclusions of applications of the new soot model include:

- The optical properties of soot generated in a Spray A simulation are calculated to find measured results are likely overpredicting the mass of soot along the central axis via KL extinction measurements.

  The experimental soot volume fraction, measured using KL extinction and assuming a monodisperse spherical soot population, and simulated soot volume fraction showed substantial differences. Using models for attenuation, absorption, and scattering, the optical extinction coefficient was found for the simulated soot. This modeled field was compared to the field of extinction coefficient created using the constant soot optical properties assumed in the measurements. The modeled extinction coefficient revealed a profile that matched the measurement based profile much more closely with much more absorption near the axis. Even allowing the possibility of relatively inaccurate soot simulation, these results indicate that local soot particle shape is an important factor in KL extinction measurements for soot volume fraction.

  Indirectly related to the optical properties, region cumulative PSDs were found to be constructions of subsets of particles with different histories and different PSDs. Without preserving independent particle histories and coupling to the Eulerian domain, this realization would not have been possible.

- An experimental and computational study on the effects of syngas with soot was performed using particle size sampling equipment combined with a 3D CFD and 0D cycle simulation approach. Experimental results showed that the addition of syngas at en-

ergy percentages as low as 25 percent had a significant impact on the shape of the PSD. In general, syngas addition reduced accumulation-mode particle concentration while increasing nucleation-mode particle concentration. The constant intake pressure cases resulted in the same effects seen for the constant premixed equivalence ratio cases even though the former showed extremely poor combustion efficiency. This indicates that the jet entrained reformed fuel, and reduction in the DI fuel quantity are mostly responsible for the effects seen in the current experiments. For similar syngas energy percentage, RCCI can further reduce accumulation-mode particle concentrations when compared to DPI at similar conditions. This is a result of lower local equivalence ratios and temperatures, both of which suppress particulate formation. Model results showed that syngas addition did not affect the soot surface chemistry but did reduce fuel stratification, which resulted in the changes to soot particle size distribution observed in the experiments.

- Investigations into the HACA mechanism for soot growth and the effect of syngas on soot in 3D domains were performed with much more detail than has been available before.

  The GM 1.9L engine simulations with the extended hybrid model allowed an in depth analysis of the acetylene addition soot production pathway that is not possible using any other commercial soot model. Acetylene addition had a much larger impact on the SOI9 and conventional case than the SOI23 case. The cause was investigated while considering temporal and spatial resolution of the soot processes. The SOI9 case kept a soot population throughout the combustion process, allowing acetylene addition to continue impacting the population. The SOI23 case oxidized all the soot created in the first and second injection, leaving only the soot from the third injection to survive until EVO. The soot generated by the third injection was only subjected to much slower acetylene addition SOI23 in the cycle. The acetylene addition rates were slowed

by reduced radicalization of active surface sites required for surface reactions such as addition. It is clear that while acetylene addition is important in soot production, it is not the only mode of growth. Accurate soot models cannot be simplified by removing or only considering acetylene addition. The heavy reliance of this model, and others, on a derivative of the HACA model to determine the crucial radicalized active surface area lights a path towards more accurate models by refinement of the radicalized active surface fraction submodel.

- A thermophoresis submodel that calculates force based on the soot particles' shape is installed to find it has a high influence on the path of the heaviest soot particles.

  A relatively simple thermophoresis model was added to simulations with the direct soot model, allowing the coupling between soot and thermophoresis to be directly observed. A Spray A case with a TEM probe was simulated to find the effect of thermophoresis was present. Thermophoresis acting directly on the particles did have an indirect effect on the flowfield.

  The GM 1.9L engine was then simulated with the direct soot and thermophoresis model. Thermophoresis had a large effect on the engine. Without thermophoresis, soot parcels weren't likely to stay near the cooler cylinder walls and oxidation consumed the accumulation mode particles. With thermophoresis, matches to measured PSDs were qualitatively good fits, which matching identifiable characteristics for all three cases. All the simulations underpredicted the quantity of particles, but the quantitative results were mostly within an order of magnitude.

8.2 Future work

The new soot model is already more detailed and possibly more accurate than other commercially available options and its almost purely physics-based composition make its use in

simulating and analyzing interesting soot scenarios a prime option. However, like all models, it is far from perfect and its future should be filled with refinement as well as use.

Index of refraction

In the optical properties section, (§4), a constant value for the index of refraction was used. In reality, the index of refraction is a complicated and ill understood value, possibly because of its implementation in equations that are oversimplifications [54], but the general theory relates it to the free electron densities. Soot particle free electron densities not provided by the current implementation of the soot model. If the soot model's framework was updated to include free electron model, an index of refraction model could be used, such as the Drude-Lorentz dispersion model. Free electron densities are a function of the molecule or soot particle construction [114]. Selecting a model for the free electrons of a soot particle may require allowing oxygen atoms in a soot particle and a tally of molecular structures.

Parcel temperature models

Section 7 showed that the effects of thermophoresis are nonnegligable but the thermophoresis model was built on assumptions that are flawed. Namely, that soot parcels are at interpolated cell temperatures. For quantitative results, the parcel temperature needs to account for the thermal boundary layer near walls that are driving steep temperature gradients. Additionally, a conjugate heat transfer model for walls should be applied.

Radiation

Adding a radiation model to soot should be done. Initial radiation models can be added for qualitative results in the same way the thermophoresis model was added. Soot particles have a very low thermal time constant as shown in section 3.4. This means soot transfers heat from one region of the cylinder to another, or to a boundary. Modeling this effect could have large implications considering the temperature sensitivity of many combustion processes, including

soot production. The major complications with a radiation model in an Eulerian framework are the number of calculations required and the path dependancy of the radiation. Assuming every cell transmits some amount of radiation to every other cell, a calculation needs to be performed for every unique pair of cells in the domain. This series is given by $\binom{n}{2}$, or $\frac{n^2}{2}$ where n is the number of cells. When calculating the radiation transmission between a pair of cells that are not adjacent, some of the radiation will be attenuated by the cells along the path. Complicating the issue, is the path length of the radiation through the cell is also necessary to account for cells that may be traversed obliquely. Carefully selecting the order of cell pair calculations, or "ray tracing", becomes important here so that the amount of radiation left is known. If the combustion simulation is only first order accurate in general, getting better results will be very expensive. Implementing a radiation model using Lagrangian soot parcels which are discrete and possibly fewer than the number of cells potentially alleviates both of these problems. Additionally, the optical properties have already been implmented in section 4, although the model may need to modified to account for spectrum dependent emission.

Active site fraction

The submodel for the active site fraction (α_{as}) used in acetylene addition contains the only empirical term in the entire soot model. The current active site surface fraction submodel (Eq. 8.1) is an empirical fit created by Appel et al. [3].

$$\alpha_{as} = \tanh(\frac{a}{\log(\mu)} + b) \tag{8.1}$$

where μ is the first size moment and a and b are empirical parameters.

So that results can be interpreted based on only the underlying physical phenomenon, a phenomenological active site surface model should be installed. Celnik et al. [15] have already implemented this in 0D. In their model, the active surface sites are reactants or products for surface reactions and the active sites on a particle must be tracked just like the age of the

particle. Future work should adapt this or a similar model to the current implementation.

9 BIBLIOGRAPHY

[1] Neerav Abani and Rolf D Reitz. A model to predict spray-tip penetration for time-varying injection profiles. In *ILASS Americas, 20th Annual Conference on Liquid Atomization and Spray Systems*, 2007.

[2] Anthony A Amsden and Margaret Findley. Kiva-3v: A block-structured kiva program for engines with vertical or canted valves. Technical report, Lawrence Livermore National Lab.(LLNL), Livermore, CA (United States), 1997.

[3] Jörg Appel, Henning Bockhorn, and Michael Frenklach. Kinetic modeling of soot formation with detailed chemistry and physics: laminar premixed flames of {C2} hydrocarbons. *Combustion and Flame*, 121(1–2):122 – 136, 2000.

[4] Susanna WM AuYeung. Finding probability distributions from moments. *Master's Thesis, Imperial College, London*, 2003.

[5] M Balthasar and M Kraft. A stochastic approach to calculate the particle size distribution function of soot particles in laminar premixed flames. *Combustion and Flame*, 133(3):289 – 298, 2003.

[6] Alfred Barnard Basset. *A treatise on hydrodynamics: with numerous examples*, volume 2. Deighton, Bell and Company, 1888.

[7] Jennifer C. Beale and Rolf D. Reitz. Modeling spray atomization with the kelvin-helmholtz/rayleigh-taylor hybrid model. *Atomization and Sprays*, 9(6):623–650, 1999.

[8] Mark S Bentley. aggregate.

[9] Mohan Bobba, Mark Musculus, and Wiley Neel. Effect of post injections on in-cylinder and exhaust soot for low-temperature combustion in a heavy-duty diesel engine. *SAE International Journal of Engines*, 3(1):496–516, 2010.

[10] H. Bockhorn. *Soot Formation in Combustion: Mechanisms and Models*. Springer Series in Chemical Physics. Springer Berlin Heidelberg, 2013.

[11] James R Brock. On the theory of thermal forces acting on aerosol particles. *Journal of Colloid Science*, 17(8):768 – 780, 1962.

[12] GC Bushell, YD Yan, D Woodfield, JUDY Raper, and ROSE Amal. On techniques for the measurement of the mass fractal dimension of aggregates. *Advances in Colloid and Interface Science*, 95(1):1–50, 2002.

[13] Makis Caracotsios and Warren E Stewart. Sensitivity analysis of initial value problems with mixed odes and algebraic equations. *Computers & Chemical Engineering*, 9(4):359–365, 1985.

[14] Matthew Celnik, Robert Patterson, Markus Kraft, and Wolfgang Wagner. Coupling a stochastic soot population balance to gas-phase chemistry using operator splitting. *Combustion and Flame*, 148(3):158 – 176, 2007.

[15] Matthew Celnik, Abhijeet Raj, Richard West, Robert Patterson, and Markus Kraft. Aromatic site description of soot particles. *Combustion and Flame*, 155(1):161 – 180, 2008.

[16] P Chan and B Dahneke. Free-molecule drag on straight chains of uniform spheres. *Journal of applied physics*, 52(5):3106–3110, 1981.

[17] Hsueh-chia Chang and T. T. Charalampopoulos. Determination of the wavelength dependence of refractive indices of flame soot. *Proceedings of the Royal Society of London. Series A: Mathematical and Physical Sciences*, 430(1880):577–591, 1990.

[18] FDF Chuahy. *A pathway to higher efficiency IC engines through thermochemical recovery and fuel reforming*. PhD thesis, PhD Thesis, Department of Mechanical Engineering, University of Wisconsin ..., 2018.

[19] Flavio D. F. Chuahy. *A Pathway to Higher Efficiency Internal Combustion Engines through Thermochemical Recovery and Fuel Reforming*. PhD thesis, University of Wisconsin, Madison, 2018. Copyright - Database copyright ProQuest LLC; ProQuest does not claim copyright in the individual underlying works; Last updated - 2019-10-18.

[20] Flavio Dal Forno Chuahy, Jamen Olk, and Sage Kokjohn. Reformed fuel substitution for transient peak soot reduction. Technical report, SAE Technical Paper, 2018.

[21] Flavio DF Chuahy and Sage L Kokjohn. High efficiency dual-fuel combustion through thermochemical recovery and diesel reforming. *Applied energy*, 195:503–522, 2017.

[22] Flavio DF Chuahy and Sage L Kokjohn. Single fuel rcci combustion using reformed fuel. 2017.

[23] Clayton T Crowe, M Pt Sharma, and David E Stock. The particle-source-in cell (psi-cell) model for gas-droplet flows. *Journal of fluids engineering*, 99(2):325–332, 1977.

[24] K.J. Daun and S.C. Huberman. Influence of particle curvature on transition regime heat conduction from aerosolized nanoparticles. *International Journal of Heat and Mass Transfer*, 55(25):7668 – 7676, 2012.

[25] P Dearden and R Long. Soot formation in ethylene and propane diffusion flames. *Journal of Applied Chemistry*, 18(8):243–251, 1968.

[26] John E Dec, Yi Yang, and Nicolas Dronniou. Boosted hcci-controlling pressure-rise rates for performance improvements using partial fuel stratification with conventional gasoline. *SAE International Journal of Engines*, 4(1):1169–1189, 2011.

[27] Reaction Design. Chemkin theory manual. *San Diego, CA*, 2007.

[28] Richard A. Dobbins and Constantine M. Megaridis. Absorption and scattering of light by polydisperse aggregates. *Appl. Opt.*, 30(33):4747–4754, Nov 1991.

[29] DOE. Role of modeling and simulation in scientific discovery, Jan 2013.

[30] Pratik Donde, Venkat Raman, Michael E. Mueller, and Heinz Pitsch. Les/pdf based modeling of soot–turbulence interactions in turbulent flames. *Proceedings of the Combustion Institute*, 34(1):1183 – 1192, 2013.

[31] Pavan Prakash Duvvuri, Rajesh Kumar Shrivastava, Sujith Sukumaran, and Sheshadri Sreedhara. Numerical modeling of thermophoretic deposition on cylinder liner of a diesel engine using a sectional soot model. *Journal of Aerosol Science*, 139:105464, 2020.

[32] Andreas Eibeck and Wolfgang Wagner. Stochastic interacting particle systems and nonlinear kinetic equations. *Annals of Applied Probability*, pages 845–889, 2003.

[33] Paul S Epstein. Zur theorie des radiometers. *Zeitschrift für Physik*, 54(7-8):537–563, 1929.

[34] Martin Fierz, Ralf Kaegi, and Heinz Burtscher. Theoretical and experimental evaluation of a portable electrostatic tem sampler. *Aerosol Science and Technology*, 41(5):520–528, 2007.

[35] ANSYS Fluent. Ansys fluent theory guide. *ANSYS Inc., USA*, 15317:724–746, 2011.

[36] Michael Frenklach. Computer modeling of infinite reaction sequences: A chemical lumping. *Chemical Engineering Science*, 40(10):1843 – 1849, 1985.

[37] Michael Frenklach. Reaction mechanism of soot formation in flames. *Physical chemistry chemical Physics*, 4(11):2028–2037, 2002. great summary and explination of HACA method and particle growth in general.

[38] Michael Frenklach and Hai Wang. Detailed mechanism and modeling of soot particle formation. In *Soot formation in combustion*, pages 165–192. Springer, 1994.

[39] Sheldon Kay Friedlander. Smoke, dust and haze: Fundamentals of aerosol behavior. *New York, Wiley-Interscience, 1977. 333 p.*, 1977.

[40] NA Fuks. On the theory of the evaporation of small droplets. *SOVIET PHYSICS-TECHNICAL PHYSICS*, 3(1):140–143, 1958.

[41] Wendell H Furry. On the elementary explanation of diffusion phenomena in gases. *American Journal of Physics*, 16(2):63–78, 1948.

[42] A Fusco, AL Knox-Kelecy, and DE Foster. Application of a phenomenological soot model to diesel engine combustion. In *Proceedings of the International Symposium COMODIA*, volume 94, 1994.

[43] Fred Gelbard, Yoram Tambour, and John H Seinfeld. Sectional representations for simulating aerosol dynamics. *Journal of Colloid and Interface Science*, 76(2):541–556, 1980.

[44] Rhys Goldstein and Azam Khan. Simulation-based architectural design. In *Guide to Simulation-Based Disciplines*, pages 167–182. Springer, 2017.

[45] Michael Goodson and Markus Kraft. An efficient stochastic algorithm for simulating nano-particle dynamics. *Journal of Computational Physics*, 183(1):210 – 232, 2002.

[46] SL Gorelov. Thermophoresis and photophoresis in a rarefied gas. *Fluid Dynamics*, 11(5):800–804, 1976.

[47] AD Gosman and D Clerides. Diesel spray modelling: a review. *Proceedings of ILASS-Europe, Florence, Italy*, 1997.

[48] Christopher J Greenshields. Openfoam user guide version 4.0. *OpenFOAM Foundation Ltd., London*, 2016.

[49] C. Van Gulijk, J.C.M. Marijnissen, M. Makkee, J.A. Moulijn, and A. Schmidt-Ott. Measuring diesel soot with a scanning mobility particle sizer and an electrical low-pressure impactor: performance assessment with a model for fractal-like agglomerates. *Journal of Aerosol Science*, 35(5):633 – 655, 2004.

[50] Hongsheng Guo, Fengshan Liu, Gregory J Smallwood, and Ömer L Gülder. Numerical study on the influence of hydrogen addition on soot formation in a laminar ethylene–air diffusion flame. *Combustion and Flame*, 145(1-2):324–338, 2006.

[51] Dong Han, Andrew M Ickes, Stanislav V Bohac, Zhen Huang, and Dennis N Assanis. Premixed low-temperature combustion of blends of diesel and gasoline in a high speed compression ignition engine. *Proceedings of the combustion institute*, 33(2):3039–3046, 2011.

[52] Zhiyu Han and Rolf D Reitz. Turbulence modeling of internal combustion engines using rng κ-ε models. *Combustion science and technology*, 106(4-6):267–295, 1995.

[53] Zhiyu Han, Ali Uludogan, Gregory J Hampson, and Rolf D Reitz. Mechanism of soot and nox emission reduction using multiple-injection in a diesel engine. *SAE transactions*, pages 837–852, 1996.

[54] Tara Henriksen, Terry Ring, Derrick Call, Eric Eddings, and A Sarofim. Determination of soot refractive index as a function of height in an inverse diffusion flame. In *5th US Combustio Meeting, University of California at San Diego*, pages 1795–1803, 2007.

[55] Randy Hessel, Rolf Reitz, Mark Musculus, Jacqueline O'Connor, and Daniel Flowers. A cfd study of post injection influences on soot formation and oxidation under diesel-like operating conditions. *SAE International Journal of Engines*, 7(2):694–713, 2014.

[56] J. Heyder, J. Gebhart, G. Rudolf, C.F. Schiller, and W. Stahlhofen. Deposition of particles in the human respiratory tract in the size range 0.005-15 um. *Journal of Aerosol Science*, 17(5):811 – 825, 1986.

[57] Derek J Hudson. Lectures on elementary statistics and probability. Technical report, Cern, 1963.

[58] Wontae Hwang, John Dec, and Magnus Sjöberg. Spectroscopic and chemical-kinetic analysis of the phases of hcci autoignition and combustion for single-and two-stage ignition fuels. *Combustion and Flame*, 154(3):387–409, 2008.

[59] Viswanath R. Katta, Linda G. Blevins, and William M. Roquemore. Dynamics of an inverse diffusion flame and its role in polycyclic-aromatic-hydrocarbon and soot formation. *Combustion and Flame*, 142(1):33 – 51, 2005.

[60] Chaitanya Kavuri, Jordan Paz, and Sage L Kokjohn. A comparison of reactivity controlled compression ignition (rcci) and gasoline compression ignition (gci) strategies at high load, low speed conditions. *Energy conversion and management*, 127:324–341, 2016.

[61] Chaitanya Kavuri, Mike Tiry, Jordan Paz, and Sage L Kokjohn. Experimental and computational investigation of soot production from a premixed compression ignition engine using a load extension injection. *International Journal of Engine Research*, page 1468087416650073, 2016.

[62] Andrei Kazakov and Michael Frenklach. Dynamic modeling of soot particle coagulation and aggregation: Implementation with the method of moments and application to high-pressure laminar premixed flames. *Combustion and Flame*, 114(3):484 – 501, 1998.

[63] Andrei Kazakov, Hai Wang, and Michael Frenklach. Detailed modeling of soot formation in laminar premixed ethylene flames at a pressure of 10 bar. *Combustion and Flame*, 100(1):111 – 120, 1995.

[64] Ian M Kennedy. Models of soot formation and oxidation. *Progress in Energy and Combustion Science*, 23(2):95 – 132, 1997.

[65] Ian M. Kennedy, Clement Yam, Darrell C. Rapp, and Robert J. Santoro. Modeling and measurements of soot and species in a laminar diffusion flame. *Combustion and Flame*, 107(4):368 – 382, 1996.

[66] Thomas Kiørboe. Formation and fate of marine snow: small-scale processes with large-scale implications. *Scientia marina*, 65(S2):57–71, 2001.

[67] David B. Kittelson, Jeffrey L. Ambs, and Hassan Hadjkacem. Particulate emissions from diesel engines:influence of in-cylinder surface. In *International Congress and Exposition*. SAE International, feb 1990.

[68] David B. Kittelson and Nick Collings. Origin of the response of electrostatic particle probes. In *SAE International Congress and Exposition*. SAE International, feb 1987.

[69] David B Kittelson, Winthrop F Watts, and Jason P Johnson. Nanoparticle emissions on minnesota highways. *Atmospheric Environment*, 38(1):9–19, 2004.

[70] David Klos and Sage L Kokjohn. Investigation of the sources of combustion instability in low-temperature combustion engines using response surface models. *International Journal of Engine Research*, 16(3):419–440, 2015.

[71] Katsufumi Kondo, Tetsuya Aizawa, Sanghoon Kook, and Lyle Pickett. Uncertainty in sampling and tem analysis of soot particles in diesel spray flame. 04 2013.

[72] VM Kontorovich. The evolution of galaxies in the mirror of the coagulation equation. *Low Temperature Physics*, 43(1):34–46, 2017.

[73] Sanghoon Kook and Lyle M. Pickett. Soot volume fraction and morphology of conventional, fischer-tropsch, coal-derived, and surrogate fuel at diesel conditions. 5:647–664, 01 2012.

[74] Takashi Kozasa, Jürgen Blum, and Tadashi Mukai. Optical properties of dust aggregates: I. wavelength dependence. *Astronomy and Astrophysics*, 263(1-2):423–432, 1992.

[75] Keith J Laidler. Rene marcelin (1885-1914), a short-lived genius of chemical kinetics. *Journal of Chemical Education*, 62(11):1012, 1985.

[76] Anshuman Amit Lall, Weizhi Rong, Lutz Mädler, and Sheldon K Friedlander. Nanoparticle aggregate volume determination by electrical mobility analysis: Test of idealized aggregate theory using aerosol particle mass analyzer measurements. *Journal of aerosol science*, 39(5):403–417, 2008.

[77] LONG Liang, Rolf D Reitz, Claudia O Iyer, and Jianwen Yi. Modeling knock in spark-ignition engines using a g-equation combustion model incorporating detailed chemical kinetics. Technical report, SAE Technical Paper, 2007.

[78] David O Lignell, Jacqueline H Chen, Philip J Smith, Tianfeng Lu, and Chung K Law. The effect of flame structure on soot formation and transport in turbulent nonpremixed flames using direct numerical simulation. *Combustion and Flame*, 151(1-2):2–28, 2007.

[79] F. Liu, K.J. Daun, D.R. Snelling, and G.J. Smallwood. Heat conduction from a spherical nano-particle: status of modeling heat conduction in laser-induced incandescence. *Applied Physics B*, 83(3):355–382, Jun 2006.

[80] Yongchun Liu, Chang Liu, Jinzhu Ma, Qingxin Ma, and Hong He. Structural and hygroscopic changes of soot during heterogeneous reaction with o3. *Phys. Chem. Chem. Phys.*, 12:10896–10903, 2010.

[81] Ola Lögdberg. Vortex generators and turbulent boundary layer separation control. 2006.

[82] Andrew Edward Lutz, Robert J Kee, and James Angus Miller. Senkin: A fortran program for predicting homogeneous gas phase chemical kinetics with sensitivity analysis. Technical report, Sandia National Labs., Livermore, CA (USA), 1988.

[83] Daniel W. Mackowski. Electrostatics analysis of radiative absorption by sphere clusters in the Rayleigh limit: application to soot particles. *Appl. Opt.*, 34(18):3535, June 1995.

[84] Julien Manin, Lyle M Pickett, and Scott A Skeen. Two-color diffused back-illumination imaging as a diagnostic for time-resolved soot measurements in reacting sprays. *SAE International Journal of Engines*, 6(4):1908–1921, 2013.

[85] YEYE MESHKOV. Inability of a shock wave accelerated interface between two gases(instability of shock wave accelerated interface between two gases). 1970.

[86] J. A. Molina-Bolívar, F. Galisteo-González, and R. Hidalgo-Álvarez. Fractal aggregates induced by antigen antibody interaction. *Langmuir*, 17(8):2514–2520, 2001.

[87] Neal Morgan, Markus Kraft, Michael Balthasar, David Wong, Michael Frenklach, and Pablo Mitchell. Numerical simulations of soot aggregation in premixed laminar flames. *Proceedings of the Combustion Institute*, 31(1):693–700, 2007. awesome 3D soot particle models.

[88] Sebastian Mosbach, Matthew S. Celnik, Abhijeet Raj, Markus Kraft, Hongzhi R. Zhang, Shuichi Kubo, and Kyoung-Oh Kim. Towards a detailed soot model for internal combustion engines. *Combustion and Flame*, 156(6):1156 – 1165, 2009.

[89] Y. NA and P. MOIN. Direct numerical simulation of a separated turbulent boundary layer. *Journal of Fluid Mechanics*, 374:379–405, 1998.

[90] Satoshi Okuzumi, Hidekazu Tanaka, and Masa-aki Sakagami. Numerical modeling of the coagulation and porosity evolution of dust aggregates. *The Astrophysical Journal*, 707(2):1247, 2009.

[91] Jiun Cai Ong, Kar Mun Pang, Jens Honore Walther, Jee-Hou Ho, and Hoon Kiat Ng. Evaluation of a lagrangian soot tracking method for the prediction of primary soot particle size under engine-like conditions. *Journal of Aerosol Science*, 115:70–95, 2018.

[92] Kihong Park, Feng Cao, David B Kittelson, and Peter H McMurry. Relationship between particle mass and mobility for diesel exhaust particles. *Environmental Science & Technology*, 37(3):577–583, 2003.

[93] N.A. Patankar and D.D. Joseph. Modeling and numerical simulation of particulate flows by the eulerian lagrangian approach. *International Journal of Multiphase Flow*, 27(10):1659 – 1684, 2001.

[94] R. I. A. Patterson, J. Singh, M. Balthasar, M. Kraft, and J. R. Norris. The linear process deferment algorithm: A new technique for solving population balance equations. *SIAM Journal on Scientific Computing*, 28(1):303–320, 2006.

[95] Robert IA Patterson, Jasdeep Singh, Michael Balthasar, Markus Kraft, and Wolfgang Wagner. Extending stochastic soot simulation to higher pressures. *Combustion and Flame*, 145(3):638–642, 2006. developes harmonic mean coagulation kernel formulation.

[96] Federico Perini, Emanuele Galligani, and Rolf D. Reitz. An analytical jacobian approach to sparse reaction kinetics for computationally efficient combustion modeling with large reaction mechanisms. *Energy & Fuels*, 26(8):4804–4822, 2012.

[97] Lyle M. Pickett and John P. Abraham. Computed and measured fuel vapor distribution in a diesel spray. *Atomization and Sprays*, 20(3):241–250, 2010.

[98] Simon F Portegies Zwart. Submission of a proposal for a commission.

[99] Y Ra and RD Reitz. The application of a multicomponent droplet vaporization model to gasoline direct injection engines. *International Journal of Engine Research*, 4(3):193–218, 2003.

[100] Daniel J Rader. Momentum slip correction factor for small particles in nine common gases. *Journal of aerosol science*, 21(2):161–168, 1990.

[101] Shuojin Ren, Sage L Kokjohn, Zhi Wang, Haoye Liu, Buyu Wang, and Jianxin Wang. A multi-component wide distillation fuel (covering gasoline, jet fuel and diesel fuel) mechanism for combustion and pah prediction. *Fuel*, 208:447–468, 2017.

[102] Kenneth L. Revzan, Nancy J. Brown, and Michael Frenklach. *Manual for the Use of Soot Subroutines in Chemical Kinetics Applications*, 1999.

[103] KJ Richards, PK Senecal, and ECONVERGE Pomraning. Converge 2.1. 0 theory manual, convergent science. *Inc., Middleton, WI*, 2013.

[104] Robert D. Richtmyer. Taylor instability in shock acceleration of compressible fluids. *Communications on Pure and Applied Mathematics*, 13(2):297–319, 1960.

[105] Steven N Rogak and Richard C Flagan. Stokes drag on self-similar clusters of spheres. *Journal of Colloid and Interface Science*, 134(1):206–218, 1990.

[106] Javier Rojo, editor. *Recovery of Distributions via Moments*, volume Volume 57 of *Lecture Notes–Monograph Series*, pages 252–265. Institute of Mathematical Statistics, Beachwood, Ohio, USA, 2009.

[107] Taylor Ross. Emissions during catalyst heating operation. *University of Wisconsin-Madison (May 2020)*, 2020.

[108] Subrata P Roy, Paul G Arias, Vivien R Lecoustre, Daniel C Haworth, Hong G Im, and Arnaud Trouvé. Development of high fidelity soot aerosol dynamics models using method of moments with interpolative closure. *Aerosol Science and Technology*, 48(4):379–391, 2014.

[109] RJ Samson, George W Mulholland, and JW Gentry. Structural analysis of soot agglomerates. *Langmuir*, 3(2):272–281, 1987.

[110] A Schmidt-Ott, U Baltensperger, H.W GÃggeler, and D.T Jost. Scaling behaviour of physical parameters describing agglomerates. *Journal of Aerosol Science*, 21(6):711 – 717, 1990.

[111] Scott A Skeen, Julien Manin, Kristine Dalen, and Lyle M Pickett. Extinction-based imaging of soot processes over a range of diesel operating conditions. In *8th US National combustion meeting*, 2013.

[112] M von Smoluchowski. Drei vortrage uber diffusion, brownsche bewegung und koagulation von kolloidteilchen. *ZPhy*, 17:557–585, 1916.

[113] Sibendu Som, Douglas E Longman, Zhaoyu Luo, Max Plomer, Tianfeng Lu, Peter K Senecal, and Eric Pomraning. Simulating flame lift-off characteristics of diesel and biodiesel fuels using detailed chemical-kinetic mechanisms and large eddy simulation turbulence model. *Journal of Energy Resources Technology*, 134(3):032204, 2012.

[114] BJ Stagg and TT Charalampopoulos. Refractive indices of pyrolytic graphite, amorphous carbon, and flame soot in the temperature range 25 to 600 c. *Combustion and flame*, 94(4):381–396, 1993.

[115] Tyler Strickland and Sage Kokjohn. Simulation of a diesel fuel jet with a 3d stochastic soot model. In *2018 Spring Technical Meeting, Central States Section of The Combustion Institute*, 2018.

[116] Blake R. Suhre and David E. Foster. In-cylinder soot deposition rates due to thermophoresis in a direct injection diesel engine. *SAE Transactions*, 101:1648–1661, 1992.

[117] L. Talbot, R. Cheng, R. Schefer, and D. R. Willis. Thermophoresis of particles in a heated boundary layer. *Journal of Fluid Mechanics*, 101:737–758, 1980.

[118] Condor Team. Condor version 7.4. 2 manual. *University of Wisconsin-Madison (May 2010)*, 2011.

[119] PA Tesner. Formation of dispersed carbon by thermal decomposition of hydrocarbons. In *Symposium (International) on Combustion*, volume 7, pages 546–553. Elsevier, 1958.

[120] PA Tesner, HJ Robinovitch, and IS Rafalkes. The formation of dispersed carbon in hydrocarbon diffusion flames. In *Symposium (International) on Combustion*, volume 8, pages 801–806. Elsevier, 1961.

[121] Naomi Tokura, Katsunori Terasaka, and Seishi Yasuhara. Process through which soot intermixes into lubricating oil of a diesel engine with exhaust gas recirculation. In *SAE International Congress and Exposition*. SAE International, feb 1982.

[122] TC Tow, DA Pierpont, and Rolf D Reitz. Reducing particulate and no x emissions by using multiple injections in a heavy duty di diesel engine. *SAE transactions*, pages 1403–1417, 1994.

[123] Max Trautz. Das gesetz der reaktionsgeschwindigkeit und der gleichgewichte in gasen. bestätigung der additivität von cv-3/2r. neue bestimmung der integrationskonstanten und der moleküldurchmesser. *Zeitschrift für anorganische und allgemeine Chemie*, 96(1):1–28, 1916.

[124] Armin Veshkini, Seth B. Dworkin, and Murray J. Thomson. A soot particle surface reactivity model applied to a wide range of laminar ethylene/air flames. *Combustion and Flame*, 161(12):3191 – 3200, 2014.

[125] L Waldmann and KH Schmitt. Thermophoresis and diffusiophoresis of aerosols. In *Aerosol science*, volume 148. Academic Press New York, 1966.

[126] Wan Mohd Faizal Wan Mahmood, Antonino LaRocca, Paul J. Shayler, Fabrizio Bonatesta, and Ian Pegg. Predicted paths of soot particles in the cylinders of a direct injection diesel engine. In *SAE 2012 World Congress and Exhibition*. SAE International, apr 2012.

[127] Hai Wang and Michael Frenklach. A detailed kinetic modeling study of aromatics formation in laminar premixed acetylene and ethylene flames. *Combustion and flame*, 110(1-2):173–221, 1997.

[128] Hu Wang, Mingfa Yao, Zongyu Yue, Ming Jia, and Rolf D. Reitz. A reduced toluene reference fuel chemical kinetic mechanism for combustion and polycyclic-aromatic hydrocarbon predictions. *Combustion and Flame*, 162(6):2390 – 2404, 2015.

[129] Mingrui Wei, Jinping Liu, Guanlun Guo, and Song Li. The effects of hydrogen addition on soot particle size distribution functions in laminar premixed flame. *International Journal of Hydrogen Energy*, 41(14):6162–6169, 2016.

[130] Jill M. Williams and Louis A. Gritzo. in situ sampling and transmission electron microscope analysis of soot in the flame zone of large pool fires. *Symposium (International) on Combustion*, 27(2):2707 – 2714, 1998.

[131] Martin Wissink and Rolf Reitz. Exploring the role of reactivity gradients in direct dual fuel stratification. *SAE International Journal of Engines*, 9(2):1036–1048, 2016.

[132] De xin Liu and Hong qing Feng. In-cylinder temperature field measurement with laser shearing interferometry for spark ignition engines. *Optics and Lasers in Engineering*, 44(12):1258 – 1269, 2006.

[133] Zongyu Yue, Randy Hessel, and Rolf D Reitz. Cfd study of soot reduction mechanisms of post-injection in spray combustion. Technical report, SAE Technical Paper, 2015.

[134] Cuiqi Zhang, Longfei Chen, Shuiting Ding, Huanhuan Xu, Guangze Li, Jean-Louis Consalvi, and Fengshan Liu. Effects of soot inception and condensation pah species and fuel preheating on soot formation modeling in laminar coflow ch4/air diffusion flames doped with n-heptane/toluene mixtures. *Fuel*, 253:1371–1377, 2019.

[135] Q. Zhang and P.A. Rubini. Modelling of light extinction by soot particles. *Fire Safety Journal*, 46(3):96 – 103, 2011.

[136] Yizhou Zhang. *Comparisons of particulate size distributions from multiple combustion strategies*. The University of Wisconsin-Madison, 2017.

[137] Bin Zhao, Zhiwei Yang, Zhigang Li, Murray V. Johnston, and Hai Wang. Particle size distribution function of incipient soot in laminar premixed ethylene flames: effect of flame temperature. *Proceedings of the Combustion Institute*, 30(1):1441 – 1448, 2005.

[138] Bin Zhao, Zhiwei Yang, Jinjin Wang, Murray V. Johnston, and Hai Wang. Analysis of soot nanoparticles in a laminar premixed ethylene flame by scanning mobility particle sizer. *Aerosol Science and Technology*, 37(8):611–620, 2003.

[139] Shu Zheng, Yu Yang, Ran Sui, and Qiang Lu. Effects of c2h2 and c2h4 radiation on soot formation in ethylene/air diffusion flames. *Applied Thermal Engineering*, 183:116194, 2021.

[140] Muhammad Ahmar Zuber, Wan Mohd Faizal Wan Mahmood, Zambri Harun, Zulkhairi Zainol Abidin, Antonino La Rocca, Paul Shayler, and Fabrizio Bonatesta. Modeling

of in-cylinder soot particle size evolution and distribution in a direct injection diesel engine. In *SAE 2015 World Congress and Exhibition*. SAE International, apr 2015.

A APPENDIX

A.1 Central tendencies

Harmonic mean

The harmonic mean, given by equation A.1, gives the average rate of simultaneous random process.

$$H = \frac{n}{\frac{1}{x_1} + \frac{1}{x_2} + \cdots + \frac{1}{x_n}} = \frac{n}{\sum_{i=1}^{n} \frac{1}{x_i}} \tag{A.1}$$

For instance, if soot inception occurs at a rate of once per zeptosecond ($1e21$ times per second), and oxidation occurs at a rate of three times per zeptosecond, then the average rate is $\frac{4}{3}$ times per zeptosecond.

Geometric mean

The geometric mean, given by equation A.2.

$$G = \sqrt[n]{x_1 x_2 \cdots x_n} = \left(\prod_{i=1}^{n} x_i \right)^{\frac{1}{n}} \tag{A.2}$$

The geometric mean is useful in finding the central tendency in values that span orders of magnitude. For instance, if on particle distribution has 1e14 particles and another has 1e4, then the geometric mean of the two populations is 1e9 particles. This may be more useful than the arithmetic mean of 5.0000000005e13 particles.

A.2 Markovian processes

A markovian process is a sequence of events where the probability of moving into a new state is defined by the current state.

Jump rate

The jump rate is the frequency at which one state moves to another. If the events are random and distributed according to the Poisson distribution, the jump rate will follow the exponential distribution.

A.3 Statistical distributions

Poisson distribution

The discrete random variable X follows the Poisson distribution if

$$f(k;\lambda) = \Pr(X = k) = \frac{\lambda^k e^{-\lambda}}{k!} \tag{A.3}$$

where k is the number of occurrences and λ is the expected number of occurrences. The

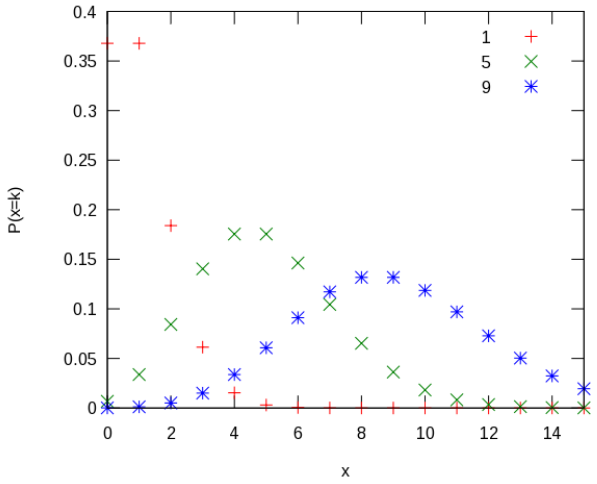

Figure A.1: Probability of $x = k$, where k is an integer, for x that follows a Poisson distribution with the indicated λ

Poisson distribution gives the probabilbity distribution of the number of occurences of an event, k, if k is randomly distributed and the expected number of occurences is λ. If k and λ are per time, then they become rates. For instance, if soot inception occurs at a rate of once per zeptosecond ($1e21$ times per second), then there is roughly a 6.1 percent chance of

3 inception events occurring in a zeptosecond. The probability distribution for such an event can be found in figure A.1

An important aspect of Poisson processes is that they can be combined to form a cumulative Poisson process. For example, if oxidation is a Poisson process occurring at λ_{ox}, and inception is an independent Poisson process occurring at λ_{in}, then the combined oxidation and inception process is also a Poisson process occurring at $\lambda_{in} + \lambda_{in}$

Exponential distribution

The discrete random variable X follows the exponential distribution if

$$f(x;\lambda) = \begin{cases} \lambda e^{-\lambda x} & x \geq 0, \\ 0 & x < 0. \end{cases} \tag{A.4}$$

where λ is the occurrence rate. The exponential distribution gives the probable time distri-

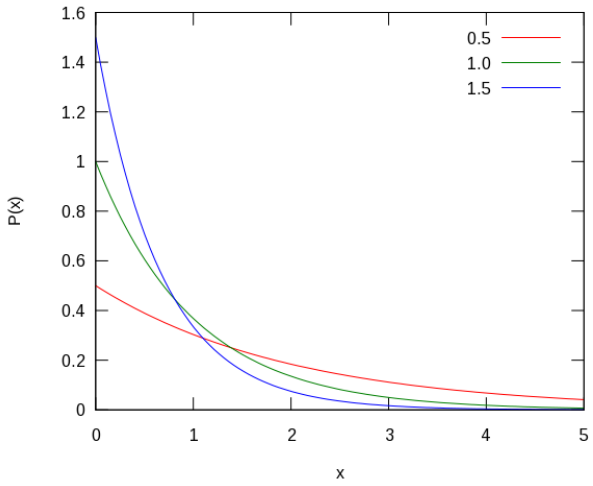

Figure A.2: Probability of x for x that follows an exponential distribution with the indicated λ

bution until an event occurs, if that event occurs randomly and with a rate λ. For instance, if soot inception occurs randomly with an expected rate of once per zeptosecond ($1e21$ times per second), then there is roughly an 8.6 percent chance of the first inception event, since

the start of timing, occurring between 2 and 3 zeptoseconds. The probability distribution for such an event can be found in figure A.2

A.4 PSD notation

Figure 3.19 has plots of distribution functions of the number of soot particles, distributed by the size of particles. This format is a standard in soot literature due to its applicability to quantities of interest in soot, namely, how many and what size. Generating such a figure is not obvious, however, and the axis titles can be difficult to interpret. Understanding these figures requires an understanding of cumulative distribution functions. The cumulative distribution function is defined as

$$CDF(x) = \int_{-\infty}^{x} f(x)dx \tag{A.5}$$

where X is the particle size. The CDF of the function f is the cumulative for all particles smaller than x. To make one of the plots of figure 3.19, f is the electrodynamic diameter of particle x and a change of variables is made to give the correct axis, $log(f(log(x)))$ vs $log(x)$. Note that the axis units labels correspond to the integrand and variable of integration for the CDF. The axis are put on a logarithmic scale due to soot's propensity to span many orders of magnitude and our resulting limited interest in the magnitude.

A.5 Conservation equations

Variables (c) in Eulerian space are described by convection-diffusion equations

$$\frac{\partial c}{\partial t} = \nabla \cdot (D\nabla c) - \nabla \cdot (\vec{v}c) + R \tag{A.6}$$

where $\nabla \cdot (D\nabla c)$ is the diffusion term, $\nabla \cdot (\vec{v}c)$ is the convection term, and R is the source / sink term.

Mass

if c is a density, ρ, then equation A.6 is the mass conservation equation.

Species

if c is a species fraction, Y, then equation A.6 is the species conservation equation.

Energy

if c is temperature, T and there is no phase change, then equation A.6 is the energy conservation equation.

Momentum

if c is momentum, ρu, then equation A.6 is the momentum conservation equation.

A.6 Lagrangian to Eulerian transform

Transforms from the Lagrangian to Eulerian space are made using the material derivative:

$$\frac{D()}{Dt} = \frac{\partial()}{\partial t} + \boldsymbol{v} \cdot \frac{\partial()}{\partial \boldsymbol{x}} \tag{A.7}$$

A.7 Knudsen number

The Knudsen number is a dimensionless number indicating the degree of continuum of the problem.

$$Kn = \frac{\alpha}{a} \tag{A.8}$$

α is the mean free path, or the average distance traveled by a particle between impact events. a is the particles characteristic diameter. $Kn >> 1$ molecular flow: field isn't continuous Kn 1 Knudsen flow: field isn't very continuous $Kn << 1$ continuous flow: field continuous

A.8 Lall model

The lall model is an equation of perfect spheres and aggregates with equal migration velocities and electrical charges. Assuming equally charged particles, an equality between the hydrodynamic drag force of a sphere and an aggregate. The hydrodynamic drag on a sphere [39].

$$F_{drag} = \frac{3\pi\mu d_m}{C(d_m)} c_e \tag{A.9}$$

d_m is the mobility diameter c_e is the migration velocity μ is the gas viscosity C is the Cunningham slip correction factor

$$C = 1 + Kn(A_1 + A_2 e^{-A_3/Kn}) \tag{A.10}$$

A_1, A_2, A_3 are experimental parameters A_1 1.207 A_2 0.440 A_3 0.78 [100] There is a no slip condition assumed at the surface of a sphere in the Stokes's law derived drag force. As particles approach molecular flow, the no slip condition begins to falter. The Cunningham slip correction factor accounts for non-continuum effects. In this problem, Kn is the relation between the mean free path of the gas, and the diameter of the primary particles. α of equation A.8 is defined as

$$\alpha = \frac{\mu}{\phi\rho c} \tag{A.11}$$

where ϕ is a kinetic-theory dependent, dimensionless parameter (0.491 [100]), μ is the viscosity, ρ is the density, and c is the mean velocity of the gas molecules

$$c = \frac{8RT}{\pi M} \tag{A.12}$$

where M is the gas molecular weight

The approximate hydrodynamic drag on an aggregate such that

1. Aggregate velocity is much slower than the mean molecular velocity
2. Aggregates composed of like primary particles
3. Primary particles are well within molecular flow ($Kn = \lambda/a >> 1$)
4. There are many primary particles
5. Aggregates have limited branching

[16]

$$F_{drag} = c^* N \mu a c_e / K_n \tag{A.13}$$

c^* is a dimensionless drag force (6.62 [76]) N is the number of primary particles a is the primary particle diameter c_e is the migration velocity μ is the gas viscosity Kn is the Knudsen number; a dimensionless number indicating the degree of continuum of the problem.

The result is

$$\frac{d_m}{C(d_m)} = \frac{c^* N a^2}{3\pi\lambda} \tag{A.14}$$

d_m is the mobility diameter C is the Cunningham slip correction factor c^* is a dimensionless drag force (6.62 [76]) N is the number of primary particles λ is the mean free path of the gas a is the primary particle diameter

Looking back at the assumptions on the aggregate drag, item 5 is particularly troubling since fractal dimensions near two have extensive branching. From a phenomenological view, a non-negligible effect on drag due to these branches could be expected.

$$F_{\text{modified } drag} = c^* N^{D_{f^*}} \mu a c_e / K_n \tag{A.15}$$

D_{f^*} is a sort of fractal dimension parallel

Applying an exponent to the number of particles of the aggregate drag force, equation A.13, finds consistent with the fractal nature of the aggregates.

A.9 Park model/Park's observation

Park et al. [92] utilized part of the work of Schmidt et al. [110] to identify the electric mobility diameter as the characteristic fractal length and then popularize the corresponding structure prefactor and mass fractal dimension as experimental data. This method requires at least:

1. fractal dimension is greater than 2 [110]
2. Aggregates composed of like primary particles

The fractal relation of equation 2.12 relies on the relationship between the radius of gyration and the mobility diameter.

$$N = C_A (\frac{2R_g}{a})^{D_f} \tag{A.16}$$

$$m = C'_A d_m^{D_f} \tag{A.17}$$

D_f is the mass fractal dimension a is the primary particle diameter N is the number of primary particles C_A is the structure prefactor constant which is dependent on the fractal length type used m is the mass d_m is mobility diameter

A.10 Rogak and Flagan model

$$\Xi = \frac{R_c}{R_g} = \sqrt{\frac{D_f + 2}{D_f}} \tag{A.18}$$

R_c is the collision radius R_g is the radius of gyration D_f is the fractal dimension [105]

A.11 Moments

$$\mu_n = \int_{-\infty}^{\infty} (x - c)^n \, f(x) \, dx \tag{A.19}$$

If f is a probability density function such that $\int_{-\infty}^{\infty} f(x)dx = 1$ then we get

- MO $\Rightarrow$ integral
- M1 set c $= 0 \Rightarrow$ mean
- M2 set c $=$ mean $\Rightarrow$ variance
- M3 set c $=$ mean and normalize by variance $\Rightarrow$ skewness (how not centered the distribution is)
- M4 set c $=$ mean and normalize by variance $\Rightarrow$ kurtosis (how big are the tails)
- M5 set c $=$ mean and normalize by variance $\Rightarrow$ hyperskewness
- M6 set c $=$ mean and normalize by variance $\Rightarrow$ hyperflatness

If f is not a probability density function then these have to be modified. The mean for instance is

$$\text{mean} = \frac{\int_{-\infty}^{\infty} x \, f(x) \, dx}{\int_{-\infty}^{\infty} f(x)dx} = \frac{M1}{M0} \tag{A.20}$$

The specified units in [102] and fallible code reading indicate that M_i for $i > 0$ are not normalized but adhere to the strict definitions. For use as a soot model in KIVA

$$\text{soot mass} = \sum_{i=1}^{N}(\sum_{j=1}^{L_i}\rho_j Vol_i) \tag{A.21}$$

Where N is the number of cells, L_i is the number of parcels in cell i, and

$$\rho_j = \text{average diameter} \cdot \frac{\text{number of particles}}{\text{volume}} \cdot \text{unit conversion} \tag{A.22}$$

$$= \frac{M1}{M0} \qquad M0 \qquad \frac{12}{Avogadro's} \tag{A.23}$$

The zeroth moment in the program is the number of soot particles however, all other moments and calculations are performed on a number of carbon atoms basis. The functioning program variable is μ and it is a fractional moment of $\frac{1}{6}$ intervals. So μ_6 is the first moment. This makes the first moment the average number of carbon atoms per particle. The second is the variance in number of carbon atoms per particle. Note that converting from units of carbon atoms per volume to mass per volume requires a factor of $\frac{12}{\text{Avogadro's number}}^n$ where n is the moment degree.

B EXTENDED HYBRID MODEL INSTRUCTIONS

B.1 Model application

Simulations are heavily relied on in fields where the physics involved are well understood and relatively easily modeled, such as in architecture [44], or experimentation is not possible, such as in astrophysics [98]. Engine simulation has been on the cusp of vital for many years due to the competing forces of expensive, but usually technically possible experimentation, and exceptionally difficult simulation. These applied simulations are much more familiar in industry. To this end, a freestanding set of scripts and programs requiring only a Converge, Ensight, and a Python instance callable in a bash environment will be packaged for free distribution.

B.2 Converge

The extended hybrid model is completely downstream of the engine simulation so any simulation software can be used. In this walkthrough Converge is used. The engine simulation parameter files should be placed in the `casefiles` directory. Ensight Gold files must be created from the engine simulation resutls. The Converge suite produces Ensight Gold files using its `post_convert` program. This can be run in the `casefiles/output` directory

```
$ post_convert
```

and following the prompts. For this walkthrough, the responses are as follows:

```
Enter a case name:
$ test
```

```
Enter a file type to export:
$ 2
```

where 2 corresponds to the Ensight option

```
Boundary surface output?
$ 0
```

where 0 corresponds to no

```
Please indicate the file(s) you would like to include:
$ all
```

```
Please indicate which variables you would like to include:
$ all
```

The extended hybrid model uses fields of

1. Temperature
2. Pressure
3. Mass
4. CO
5. O_2
6. OH
7. C_2H_2
8. H
9. H_2
10. H_{20}
11. A_4 (pyrene)

where species fields are in mass fraction

```
Parcel Variable Selection Menu
```

No parcel variables are selected by returning nothing. This produces the necessary files for the extended hybrid model.

B.3 Ensight

The `runEnsight.sh` script automates the parcel generation process and conforms the SWEEP simulation parameters to the engine parameters. This includes scavenging the rpm and the simulation starting crank angle from the case files. If a different engine simulation software is used, the script must be modified accordingly. Soot parcels are generated at the simulation output times issued by the `post_ca.in` file and at random locations within an isovolume defined by a threshold inception species concentration. The threshold inception species concentration is defined in `ensightEnvironmentTemplate.ctx`. Parcels can be added by increasing the number of parcels generated per time step or increasing the number of time steps.

To run this script Ensight and python must be available. For a system using environment modules, commands similar to

```
$ module load python
$ module load numpy
$ module load Ensight
```

must be issued. Running the script is done by

```
$ sh runEnsight.sh
```

Depending on the computer and case, this can take significant amounts of time ($\mathcal{O}(12)$ hours) due to the parcel trace generation.

If Ensight is not available on the system, the Ensight batch command can be removed from the script. The Ensight command files (ensightEnvironment.ctx and ensightBatch.enc) will still be produced. These files can be run using a nonintegrated Ensight instance with the command

```
$ ensight -X -batch -cwd "./ensightparcels" -p ./ensightbatchfiles/
   ↪ ensightBatch.enc
```

B.4 SWEEP

The `runSWEEP.sh` script sets up and submits individual SWEEP simulations for each parcel to many computers. To run this script Condor and AWK must be available. AWK is standard on most linux systems. Condor is a job managment system aimed at high throughput. This stage is possible without Condor by replacing the `processSWEEPruns.sh` script with an equivalent job scheduler. Running the script is done by

```
$ sh runSWEEP.sh
```

B.5 Postprocessing

The `makePlots.sh` scirpt collects and processes individual SWEEP simulation data to create a particle size distribution at the final time listed in the `times.dat` file. To run this script Python with the matplotlib library must be available.

```
$ sh makePlots.sh
```

Plotting PSDs at different times, subject to certain particle filters, or any other variation can be done relatively easily by altering the `spdfplot.py` code.